Image Potential States and Dielectric Response at Metal Surfaces

Maziar Nekovee

Image Potential States and Dielectric Response at Metal Surfaces

Maziar Nekovee

Image Potential States and Dielectric Response at Metal Surfaces

ISBN 90-9008500-9

Image Potential States and Dielectric Response at Metal Surfaces

een wetenschappelijke proeve op het gebied van
de Natuurwetenschappen

Proefschrift
ter verkrijging van de graad van doctor aan
de Katholieke Universiteit Nijmegen,
volgens besluit van het College van Decanen
in het openbaar te verdedigen op
dinsdag 12 september 1995
des namiddags te 1.30 uur precies

door

Maziar Nekovee
geboren op 14 juli 1965
te Teheran, Iran

druk: CopyPrint 2000, Enschede
1995

Promotor: Prof. Dr. J.E. Inglesfield

تقدیم به

مادر و پدر عزیز

Aan mijn ouders

Contents

Chapter 1

General Introduction

The familiar band-structure picture that serves so well for understanding most of the bulk properties of solids applies in principle only to an infinitely extended crystal with perfect lattice-translational symmetry or, in practice, to portions of a crystal which are far from any boundary. At the surface, at which even the lattice constant may differ from its bulk value, the band structure will be distorted and novel electronic properties such as localised states, surface reconstruction and enhanced magnetism make their appearance.

The importance of surfaces and interfaces in electronic device technology and material science has led to an increasing interest in these properties. Electronic structure calculations are crucial for a detailed understanding of electronic properties of surfaces and they play an essential role in forming a coherent view of other surface phenomena such as crystal growth, melting etc. The goal of surface electronic structure calculations is to characterise electronic properties of surfaces and interfaces by solving the Schrödinger equation for electrons in these systems.

At a semi-infinite system translational symmetry is broken at least in the direction perpendicular to the surface. This means that the Bloch condition no longer holds in this direction and the resulting (single-electron) Schrödinger equation has to be integrated over an *infinite* region. For this reason surface electronic structure calculations are more difficult than the bulk calculations and the specific numerical challenge in calculating electronic properties at surfaces and interfaces is to find a way to reduce the Schrödinger equation over an infinite region to an equation over a compact domain.

The most popular technique for treating this problem is to model the semi-infinite system by a (repeated) slab of finite thickness with vacuum on each side. The advantage of this method is that ordinary band structure schemes can be used to treat the surface problem. These calculations can describe properties such as total energy and charge density rather well provided that the slabs are chosen thick enough [1-3]. However, they do not exploit the relative simplicity of the perfect crystal to which they are related and they are also hindered by the fact that the individual electronic states are affected over a much larger range than are properties such as the total energy, electron density and the effective potential. Detailed interpretation of surface spectroscopies such as photoemission and inverse photoemission, which probe individual electronic states at the surface [4, 5], requires more advanced methods which take into account correctly the semi-infinite substrate.

In part I of this thesis we contribute to the developments of such calculational schemes based on the the embedding approach [6]. Embedding is a variational scheme for taking care of boundary conditions on wavefunctions within a region of interest. We show how incorporating this method into electronic structure calculations leads to an accurate and at the same time economical way of treating electronic properties of surfaces, interfaces and confined quantum systems.

In part II, we apply these calculational methods to study an important class of unoccupied states at metal surfaces: the image-induced surface states. These states originate from the long-range image potential which electrons experience outside the surface and their physics has attracted considerable interest in recent years [7]. We calculate the binding energy, dispersion relation and magnetic splitting of these states for a number of surfaces, compare them with experiments and show how these properties give information on the nature and the shape of the effective surface barrier and near-surface magnetism.

The first two parts of this work deal with the time-independent problem. Many surface sensitive experiments are however based on measuring the response of surfaces to time-varying electromagnetic fields. A detailed understanding of such experiments requires a microscopic calculation of the time-dependent dielectric response of the surface. A major problem in calculating this quantity arises from the non-local nature of the response which in a surface geometry leads to integral equations extending over an infinite domain. In part III we tackle this problem within the jellium model of the surface (a model in which the nuclei are replaced by a uniform charge background abruptly truncated at the surface) and develop a scheme for reducing these integral equations to a finite domain around the surface which can be solved numerically. Based on this scheme, we perform accurate time-dependent density functional calculations of the linear response of several simple-metal surfaces within the whole frequency range below the bulk plasma frequency.

The remaining part of this chapter gives an outline of basic concepts and methods underlying surface electronic structure calculations and in particular this work.

Units

Atomic units are used throughout, with e (the charge of an electron), m (mass of an electron) and $\hbar$ all set equal to unity. The unit of energy is the Hartree, 27.2116 eV, and the unit of distance the Bohr radius, 0.5292 Å. The average electron density is expressed in terms of r_s, the radius of the sphere containing one electron.

1.1 Mean-field treatment of the many-electron system

The first stage in understanding the behaviour of electrons in solids and at surfaces is to separate their motion from that of the atomic nuclei. This is possible because the electrons (at $\mathbf{r}_i$) are much lighter, and consequently they satisfy the Schrödinger equation in which the nuclei (at $\mathbf{r}_I$) are at rest:

$$\left\{-\frac{1}{2}\sum_i \nabla_i^2 + \frac{1}{2}\sum_{i\neq j}\frac{1}{|\mathbf{r}_i-\mathbf{r}_j|} - \sum_{i,I}\frac{Z_I}{|\mathbf{r}_i-\mathbf{r}_I|}\right\}\Psi(\{\mathbf{r}_i\}) = \mathcal{E}_0\Psi(\{\mathbf{r}_i\}). \tag{1.1}$$

The sums run over all the electrons i and the nuclei I, Z_I is the atomic number of the I'th nucleus, and Ψ is the many-electron wavefunction. The motion of the nuclei is then governed by equations of motion (usually taken to be classical) in which the ground-state electronic energy $\mathcal{E}_0$, which is a function of nuclear coordinates $\mathbf{r}_I$, behaves like a potential energy. $-\nabla_I\mathcal{E}_0$ plus the Coulomb force from the other nuclei is then the force on the I'th nucleus, and by minimising $\mathcal{E}_0$ plus the nucleus-nucleus electrostatic energy with respect to the $\mathbf{r}_I$'s the equilibrium geometry can be found. This separation of nuclear and electronic motion is the adiabatic or Born-Oppenheimer approximation [8].

Even after fixing the nuclei in their equilibrium positions, solving the full Schrödinger equation for a macroscopic crystal is intractable because of the extremely large number of electrons ($N \sim 10^{23}$) interacting with each other through the long-range Coulomb potential. In almost all electronic structure calculations for real solids, including this work, one circumvents the complexity of this problem by using a mean field approximation for the electron-electron interaction based on the density functional theory (DFT) in the local density approximation (LDA).

Density functional theory

Density functional theory is based on a theorem by Hohenberg and Kohn [9] which states that the ground-state many-body wavefunction, and hence all ground state properties and in particular the ground-state energy $\mathcal{E}_0$, are unique functionals of the ground-state electron density:

$$\mathcal{E}_0 = E[n_0(\mathbf{r})]. \tag{1.2}$$

As a consequence, the energy functional of the system is stationary with respect to variations in the electron density having a minimum at the true ground state density. Starting from this variational principle it can be shown [10] that the ground state density distribution $n_0(\mathbf{r})$ of the interacting electronic system is reproduced by the charge density of non-interacting electrons moving in the nuclear potential $v_{nuc}(\mathbf{r})$ plus an effective one-electron potential. This consist of the Hartree potential $v_h(\mathbf{r})$, the electrostatic potential due to to the charge density of all the electrons in the system, plus the exchange-correlation potential $v_{xc}(\mathbf{r})$, which accounts for the dynamically correlated motion of electrons. The resulting one-electron Schrödinger equation (the Kohn-Sham equation) is

$$[-\frac{1}{2}\nabla^2 + v_{nuc}(\mathbf{r}) + v_h(\mathbf{r}) + v_{xc}(\mathbf{r})]\psi_i(\mathbf{r}) = \epsilon_i\psi_i(\mathbf{r}) \tag{1.3}$$

from which the ground-state density and the ground state energy of the system of N interacting electrons can be calculated:

$$n_0(\mathbf{r}) = 2\sum_i |\psi_i(\mathbf{r})|^2 \tag{1.4}$$

and

$$\mathcal{E}_0 = 2\sum_i \epsilon_i - \frac{1}{2}\int d\mathbf{r} v_h(\mathbf{r})n_0(\mathbf{r}) - \int d\mathbf{r} v_{xc}(\mathbf{r})n_0(\mathbf{r}) + E_{xc}[n_0(\mathbf{r})]. \tag{1.5}$$

where ψ_i are the N/2 lowest-lying solutions of (1.3) (we ignore magnetic effects at this stage so that each solution is doubly degenerate and is occupied by a spin-up and a spin-down electron). In (1.5), the exchange-correlation energy functional E_{xc} is the difference in energy between the interacting system and the effective one-electron system defined by (1.3). It includes contributions from the electron-electron interactions beyond Hartree and *also* from the difference in the kinetic energy of the one-electron system and the actual interacting system. The exchange correlation potential is defined as the functional derivative of E_{xc} with respect to electron density:

$$v_{xc} = \frac{\delta E_{xc}}{\delta n_0(\mathbf{r})}. \tag{1.6}$$

The important message of density functional theory is that the exact ground state density can be calculated from an effective single-particle potential. However, the exact functional form of E_{xc}, and hence the exchange-correlation part of this effective potential, is not known and without having schemes to find reasonable approximation for this potential the theory is not of much practical impact.

Local density approximation

In solid state electronic structure calculations one usually proceeds by introducing the local density approximation of the exchange-correlation potential. The starting point is to assume that the external potential, and consequently the density, is slowly varying. Each point of the inhomogeneous electron system is then treated as if it were homogeneous with a density corresponding to the local value at that point. This procedure yields the following approximation for the exchange-correlation functional

$$E_{xc} \approx \int d\mathbf{r} n_0(\mathbf{r})\epsilon_{xc}(n_0(\mathbf{r})) \tag{1.7}$$

in which ϵ_{xc} is the exchange-correlation energy per electron of the homogeneous interacting electron gas. The corresponding LDA exchange-correlation potential is then given by

$$v_{xc}(\mathbf{r}) = \frac{d}{dn} n\epsilon_{xc}(n)\Big|_{n=n_0}. \tag{1.8}$$

The exchange-correlation energy of a homogeneous electron gas is known analytically in certain limits – at high electron densities where many-body perturbation theory (within the random phase approximation) can be used, and at low densities where the electrons crystallise into a Wigner lattice. Numerically, it is known from accurate quantum Monte Carlo calculations [11] for the total energy of the homogeneous electron gas of various density, which may be thought of as effectively calculating the many-electron wavefunction.

The assumption of slowly varying densities, which underlies the derivation of the LDA, is certainly not valid at the surface where the electron density drops from its bulk value to essentially zero outside the surface over a very short distance (∼ the Fermi wavelength λ_F). Nevertheless, experience shows [12, 13] that surface calculations based on the LDA capture most of the essential physics of the surface electronic structure problem. It is well-known, however, that LDA fails in reproducing correctly the asymptotic form of the potential felt by an electron outside the solid; the local density approximation gives an exponentially decaying potential outside the surface instead of the classical $-1/4z$ image potential. This is found to introduce only small errors in properties such as charge density and workfunction since these quantities are determined by occupied states of the semi-infinite metal which do not extend far into the vacuum, and hence are not sensitive to the asymptotic form of the effective potential. This is, however, not the case for the more energetic *unoccupied* states studied in part II of this thesis.

Local spin density approximation

To study magnetic systems density functional theory can be extended to include spin [14, 15]. The essential point is that instead of just considering the electron density, one now must involve the spin-densities as well. The generalised Hohenberg-Kohn theorem states then that the ground-state energy is a unique functional of charge and spin-densities and attains its minimum for the true ground state densities.

In the non-relativistic case, imposing a local spin-density approximation (LSD) [14] on the exchange-correlation functional results then in a set of coupled single-particle equations for the two spin directions:

$$[-\frac{1}{2}\nabla^2 + v_{nuc}(\mathbf{r}) + v_h(\mathbf{r}) + v_{xc}^{\uparrow\downarrow}(\mathbf{r})]\psi_i^{\uparrow\downarrow}(\mathbf{r}) = \epsilon_i\psi_i^{\uparrow\downarrow}(\mathbf{r}) \qquad (1.9)$$

from which the densities are calculated by a sum over the states below the Fermi energy (the energy of the highest occupied state of the system)

$$n_0^{\uparrow\downarrow}(\mathbf{r}) = \sum_i |\psi_i^{\uparrow\downarrow}(\mathbf{r})|^2. \qquad (1.10)$$

The spin-density $m_0(\mathbf{r})$ which gives the relative spin ordering of the system is simply the difference between the spin-up and spin-down densities

$$m_0(\mathbf{r}) = n_0^{\uparrow}(\mathbf{r}) - n_0^{\downarrow}(\mathbf{r}) \qquad (1.11)$$

and the total density is given by

$$n_0(\mathbf{r}) = n_0^{\uparrow}(\mathbf{r}) + n_0^{\downarrow}(\mathbf{r}). \tag{1.12}$$

The spin-dependent exchange-correlation potential is given by:

$$v_{xc}^{\uparrow\downarrow} = \frac{\partial}{\partial n^{\uparrow\downarrow}} n\epsilon_{xc}(n,m)\Big|_{n^{\uparrow\downarrow}=n_0^{\uparrow\downarrow}}. \tag{1.13}$$

where $\epsilon_{xc}(n,m)$ is the exchange-correlation potential energy per particle of a homogeneous electron gas which is stabilised in the spin-polarised state by a uniform magnetic field.

1.2 The Schrödinger equation at the surface

Having derived a set of single-particle Schrödinger equations for describing ground state properties of the electronic system, the next problem is to solve these equations self-consistently for electrons in a semi-infinite crystal. In a bulk crystal the effective potential v_{eff} felt by an electron has three-dimensional periodicity but at the surface the periodicity is destroyed in the perpendicular direction. However, the resulting semi-infinite crystal still has two-dimensional periodicity parallel to the surface – as long as there are no surface defects or impurities:

$$v_{eff}(\mathbf{r}_{||} + \mathbf{R}_{||}, z) = v_{eff}(\mathbf{r}_{||}, z) \tag{1.14}$$

where $\mathbf{r}_{||}$ is the vector parallel to the surface, z measures the distance perpendicular and $\mathbf{R}_{||}$ is a vector in the two-dimensional surface mesh. The two-dimensional periodicity of the potential means that the electronic wave-functions can be labelled by a two-dimensional Bloch wave-vector and satisfy the equation:

$$[-\frac{1}{2}\nabla^2 + v_{eff}(\mathbf{r}_{||}, z)]\psi_{\mathbf{k}_{||}}(\mathbf{r}_{||}, z) = E(\mathbf{k}_{||})\psi_{\mathbf{k}_{||}}(\mathbf{r}_{||}, z) \tag{1.15}$$

and the Bloch property[13]

$$\psi_{\mathbf{k}_{||}}(\mathbf{r}_{||} + \mathbf{R}_{||}, z) = \exp(i\mathbf{k}_{||}.\mathbf{R}_{||})\psi_{\mathbf{k}_{||}}(\mathbf{r}_{||}, z), \tag{1.16}$$

which implies that (1.15) needs only to be solved in one surface unit cell, but it has to be integrated from $-\infty$ to $+\infty$ in the perpendicular direction. Just as in the case of a bulk crystal, where the wave-functions are labelled by the three-dimensional Bloch wave-vector, $\mathbf{k}_{||}$ is only defined to within a *surface* reciprocal lattice vector $\mathbf{g}$ given by:

$$\mathbf{g}.\mathbf{R}_{||} = 2\pi \times \text{integer} \tag{1.17}$$

which can be added to $\mathbf{k}_{||}$ without changing the phase factor in (1.16). This lack of uniqueness in the Bloch wave-vector means that we can restrict $\mathbf{k}_{||}$ to lie in the surface Brillouin zone (BZ).

Ideal surfaces are identified by the bulk plane of termination, e.g., Cu(100) or Fe(110). When the periodicity and the orientation of the surface mesh is the same as the underlying bulk lattice (1 × 1 structures), the surface Brillouin zone is obtained by projecting the bulk Brillouin zone onto the surface plane [13]. This is illustrated in figure 1.1 for the (100) surface of face-centred cubic (fcc) crystal.

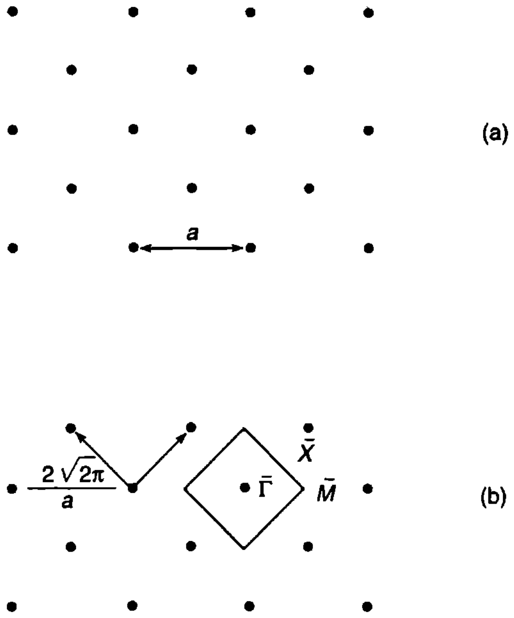

Figure 1.1: Surface mesh (a) and surface Brillouin zone of a face-centred cubic (100) crystal.

1.3 Single-particle Green function

Green functions are fascinating mathematical tools and their application is now well-established in condensed matter theory [16, 17]. In comparison with wavefunctions they carry little surplus information and provide an economical way of calculating observable quantities of general interest such as the expectation value of any single-particle operator in the ground state of the system. In addition, in solving the Schrödinger equation they provide a convenient way of handling changes in boundary conditions which occur at surfaces and interfaces for example. For these reasons we shall make extensive use of Green functions in our calculations. Since we are primarily interested in solving the single-particle Kohn-Sham equations, we restrict ourselves to discussing the corresponding single-particle Green function and its properties.

Definition and properties

We define the single-particle Green function as the solution of

$$[-\frac{1}{2}\nabla^2 + v_{eff}(\mathbf{r}) - \zeta]G(\mathbf{r},\mathbf{r}';\zeta) = \delta(\mathbf{r}-\mathbf{r}') \tag{1.18}$$

where ζ is assumed to be complex in general and $G(\mathbf{r},\mathbf{r}';\zeta)$ is subject to prescribed boundary conditions. The Hamiltonian

$$H = -\frac{1}{2}\nabla^2 + v_{eff}(\mathbf{r}) \tag{1.19}$$

has a complete set of eigenfunctions $\{\psi_\imath\}$ satisfying

$$[-\frac{1}{2}\nabla^2 + v_{eff}(\mathbf{r})]\psi_\imath(\mathbf{r}) = \epsilon_\imath\psi_\imath(\mathbf{r}) \tag{1.20}$$

and the same boundary conditions as G, and we can expand G in terms of these (orthonormal) eigenfunctions. This yields the spectral representation:

$$G(\mathbf{r},\mathbf{r}';\zeta) = \sum_\imath \frac{\psi_\imath(\mathbf{r})\psi_\imath^*(\mathbf{r}')}{\epsilon_\imath - \zeta}. \tag{1.21}$$

In general H may have both a discrete and a continuous spectrum and $\sum_\imath$ should be interpreted as a genuine summation over the discrete energies plus an integration over the continuous parts of the spectrum. It follows from (1.21) that G is an analytic function of ζ everywhere in the complex plane except along the real axis where it has simple (first order) poles at the position of discrete bound-state eigenvalues of H and branch cuts along those parts of the real axis which correspond to the continuous spectrum of H.

The retarded (advanced) Green function, defined for real ζ is obtained from G by putting $\zeta = E \pm \imath\delta$ with δ a positive (negative) infinitesimal and E real, and taking the limit as δ approaches zero. For E belonging to the continuous spectrum of H, the retarded Green function so obtained consists only of outgoing waves and the advanced Green function consists of only incoming waves. For E *not* belonging to the continuous spectrum, the retarded and advanced Green function coincide and both agree with the "general" Green function defined by (1.18). In the following and throughout this work we shall restrict ourselves to the retarded Green function, taking $E = E + i\delta$ with δ positive, and finite in practice.

Using the eigenvalue expansion (1.21) we can express quantities of interest such as the charge density, local density of states and response functions of the system in terms of the Green function. The local density of states is defined as the charge density of states having a particular energy,

$$\sigma(\mathbf{r}, E) = \sum_\imath \delta(E - \epsilon_\imath)|\psi_\imath(\mathbf{r})|^2. \tag{1.22}$$

This is given by:

$$\sigma(\mathbf{r}, E) = \frac{1}{\pi}\mathcal{I}m G(\mathbf{r},\mathbf{r}; E) \tag{1.23}$$

and the charge density of an individual (non-degenerate) state $\psi_\imath$ is given by:

$$|\psi_\imath(\mathbf{r})|^2 = Res\{G(\mathbf{r},\mathbf{r};\epsilon_\imath)\} \tag{1.24}$$

The total charge density can be find from G by integrating (1.21) over occupied states. Making use of the analyticity of G in the upper-half plane, the integration can be performed along a contour deformed into the complex plane. Contour integration provides a very economical way for calculating sums over states since in general sharp structures and singularities in G on the real axis will be smoothed by going to complex energies.

We shall discuss the single-particle density response function in part III. Evaluating this function involves infinite sums over states which can be slowly convergent. The use of Green functions allow us to express these sums in a closed-form resulting in a considerable simplification of its calculation.

Surface Green function

The surface Green function can be obtained by summing over the two-dimensional Bloch waves of the perfect semi-infinite crystal (normalised within the surface unit cell):

$$G(\mathbf{r}_{\|}, z, \mathbf{r}'_{\|}, z'; E) = \sum_{\mathbf{k}_{\|}, n} \frac{\psi_{\mathbf{k}_{\|} n}(\mathbf{r}_{\|}, z)\psi^*_{\mathbf{k}_{\|} n}(\mathbf{r}'_{\|}, z')}{E_n(\mathbf{k}_{\|}) - E + i\delta} \tag{1.25}$$

where $\mathbf{k}_{\|}$ is the wavevector parallel to the surface lying in the surface Brillouin zone, n is the band index and the sum is over all two-dimensional bands. In actual calculations it is more useful to work with the $\mathbf{k}_{\|}$-resolved Green function

$$G_{\mathbf{k}_{\|}}(\mathbf{r}_{\|}, z, \mathbf{r}'_{\|}, z'; E) = \sum_{n} \frac{\psi_{\mathbf{k}_{\|} n}(\mathbf{r}_{\|}, z)\psi^*_{\mathbf{k}_{\|} n}(\mathbf{r}'_{\|}, z')}{E_n(\mathbf{k}_{\|}) - E + i\delta}. \tag{1.26}$$

It follows from (1.26) that $G_{\mathbf{k}_{\|}}$ has the Bloch property:

$$G_{\mathbf{k}_{\|}}(\mathbf{r}_{\|} + \mathbf{R}_{\|}, z, \mathbf{r}'_{\|}, z'; E) = \exp(i\mathbf{k}_{\|}.\mathbf{R}_{\|}) G_{\mathbf{k}_{\|}}(\mathbf{r}_{\|}, z, \mathbf{r}'_{\|}, z'; E) \tag{1.27}$$

and hence $G_{\mathbf{k}_{\|}}$ needs to be evaluated only within the surface unit cell. The full Green function for the semi-infinite crystal and the charge density $n(\mathbf{r}_{\|}, z)$ can be obtained from $G_{\mathbf{k}_{\|}}$ by summing over $\mathcal{N}$ independent wavevectors in the surface Brillouin zone:

$$G(\mathbf{r}_{\|}, z, \mathbf{r}'_{\|}, z'; E) = \sum_{\mathbf{k}_{\|} \in BZ} G_{\mathbf{k}_{\|}}(\mathbf{r}_{\|}, z, \mathbf{r}'_{\|}, z'; E) \tag{1.28}$$

and

$$n(\mathbf{r}_{\|}, z) = \frac{1}{\pi} \sum_{\mathbf{k}_{\|} \in BZ} \int_{E \leq E_F} dE \sigma_{\mathbf{k}_{\|}}(\mathbf{r}_{\|}, z; E) \tag{1.29}$$

where E_F is the Fermi energy and $\sigma_{\mathbf{k}_{\|}}$ is the local density of states with a particular surface wavevector $\mathbf{k}_{\|}$ and energy E given by:

$$\sigma_{\mathbf{k}_{\|}}(\mathbf{r}_{\|}, z; E) = \frac{1}{\pi} \mathcal{I}m G_{\mathbf{k}_{\|}}(\mathbf{r}_{\|}, z, \mathbf{r}_{\|}, z; E). \tag{1.30}$$

We note that $\sigma_{\mathbf{k}_{\|}}$ characterises individual electronic states at the surface and can be probed by angle-resolved photoemission (for an occupied state) and $\mathbf{k}_{\|}$-resolved inverse photoemission (for an unoccupied state) [4, 5].

References

[1] E. Wimmer H. Krakauer, M. Weinert and A.J. Freeman, Phys. Rev. B **24**, 864 (1981).

[2] M. Needs, M.C. Payne and J.D. Joannopoulos, Phys. Rev. Lett. **65**, 3148 (1987).

[3] M. Methfessel, D. Henning and M. Scheffler, Phys. Rev. B **45**, 9410 (1992).

[4] S.D. Kevan, *Angle-Resolved Photoemission, Theory and Current Applications* (Elsevier, Amsterdam, 1992).

[5] J.C. Fuggle and J.E. Inglesfield, in *Unoccupied Electronic States*, eds. J. C. Fuggle and J. E. Inglesfield (Springer-Verlag, Berlin, 1991).

[6] J.E. Inglesfield, J. Phys. C, 3795 (1981).

[7] For a recent review see, W. Steinman and Th. Fauster, in *Laser Spectroscopy and Photochemistry on Metal Surfaces*, eds. Hai-Lung Dai and Wilson Ho (World Scientific, Singapore, 1993); P.M. Echenique and J.B. Pendry, Prog. Surf. Sci. **32**, 111 (1989).

[8] J. Callaway *Quantum Theory of the Solid State* (Academic Press, San Diego, 1991).

[9] P. Hohenberg and W. Kohn, Phys. Rev. **136**, B864 (1964).

[10] W. Kohn W and L.J. Sham, Phys. Rev. **140**, A1133 (1965).

[11] D.M. Ceperley and B.I. Alder, Phys. Rev. Lett. **45**, 566 (1980); parameterised in J.P. Perdew and A. Zunger, Phys. Rev. B **32**, 5048 (1981).

[12] H.L. Skriver and N.M. Rosengaard, Phys. Rev. B **45**, 9410 (1992).

[13] A. Zangwill *Physics at Surfaces* (Cambridge University Press, Cambridge, 1988).

[14] U. von Barth and L. Hedin, J. Phys. C **5**, 1692 (1972).

[15] J. Callaway and A.K. Rajagopal, Phys. Rev. B **7**, 1912 (1973).

[16] G. Rickayzen *Green's Functions and Condensed Matter*, (Academic Press, London, 1980).

[17] E.N. Economou, *Green's Functions in Quantum Physics* (Springer-Verlag, Berlin, 1979).

Part I

Embedding surfaces and confined quantum systems

Chapter 2

Introduction

The problem which we are considering in this part is how to solve the single-particle Schrödinger equation

$$[-\frac{1}{2}\nabla^2 + v_{eff}(\mathbf{r})]\Phi(\mathbf{r}) = E\Phi(\mathbf{r}) \tag{2.1}$$

explicitly, and usually self-consistently, within a subregion of space while implicitly accounting for the rest. Examples of systems for which this analysis is relevant are: solid surfaces, impurity atoms in solids and adsorbed atoms and molecules on surfaces. In all these cases the presence of a defect results in a significant change of the effective potential and lowers the symmetry of the system (e.g. creating a surface reduces the periodicity from three to two) or even destroys it completely (an impurity in a perfect crystal). Because symmetry is broken, solving the full Schrödinger equation for the resulting extended system is usually not tractable. On the other hand, the perturbation caused by the defect is *localised* to a finite region (e.g. a few atomic layers in the case of metal surfaces) around the defect and it is usually this small portion of the system which is relevant to the new physical phenomena which we try to understand.

The above considerations motivate the idea of exploiting the spatial localisation of the perturbation and solving the Schrödinger equation self-consistently only within the *finite* region of interest while including the coupling of electronic wavefunctions to the fixed substrate potential implicitly. This idea is in fact the starting point for approaches such as the Dyson equation formalism [1-3], the multiple scattering approach [4, 5], and finally the embedding method [6-8] for treating surfaces, interfaces and point defects.

Since the potential entering (2.1) is *local*, the coupling between the defect region and the substrate is only through the matching conditions imposed on the wavefunction and its normal derivative on the boundary, separating this region from the rest of the substrate. Consequently, one possible way of treating the problem is by direct wavefunction matching: we start with a guess for the perturbing potential, solve the Schrödinger equation explicitly in the (effectively) *finite* defect region, match the wavefunctions to the known solutions of the unperturbed system, calculate a new potential and carry on this process until self-consistency is reached .

Unfortunately explicit wavefunction matching is very involved for real three-dimensional problems in which self-consistency is required. In the embedding method [6] one avoids explicitly matching wavefunctions by adding to the Hamiltonian in the region of interest an extra effective energy-dependent *embedding potential* acting upon the boundaries of this region which forces the wavefunctions to match correctly to the substrate solutions. The embedding potential depends only on the unperturbed substrate potential outside the region of interest. Hence for a given substrate potential and a given defect geometry, that is a surface or an impurity, it can be calculated once and for all. In this way the infinite substrate is removed from the problem and all the calculational effort can be concentrated on solving an effective Schrödinger equation within the finite region of interest – the embedded region.

In the embedding formalism all the information on the substrate is contained in the embedding potential, which can be related to the the substrate Green function, and a major difficulty in applying the method to realistic systems is calculating this quantity for general substrates. The main portions of this part (chapters 3 and 4) describes contributions to developing efficient schemes for calculating the embedding potential for surface and interface problem. In addition, in chapter 5 we show how the embedding approach can be applied to the problem of finding eigenvalues of a quantum systems confined to cavities of *arbitrary* shape. The analysis is relevant for studying electronic states and energy levels in e.g. quantum well and quantum wire devices.

To make this part self-contained, we start with two introductory section giving a detailed description of the embedding formalism.

2.1 The embedding equation

To derive an effective Schrödinger equation for the wavefunction in an (effectively) finite subregion (region I in figure 2.1) embedded into the unperturbed substrate (region II), we start from the variational formulation of the Schrödinger equation for the whole space $I+II$: in the domain of all admissible functions (continuous and with continuous first derivative) defined over $I+II$ and satisfying appropriate boundary condition at infinity (or any other outer boundary of II), we are seeking a function Φ which minimises the expectation value of the Hamiltonian:

$$E[\Phi] = \frac{\int_{I+II} d\mathbf{r}\Phi^*(\mathbf{r})H\Phi(\mathbf{r})}{\int_{I+II} d\mathbf{r}\Phi^*(\mathbf{r})\Phi(\mathbf{r})}. \tag{2.2}$$

We then construct a composite trial function build up of an arbitrary function ϕ in the embedded region extended into the substrate with the solution of the unperturbed Schrödinger equation ψ at some trial energy ϵ

$$[-\frac{1}{2}\nabla^2 + v_{eff}(\mathbf{r})]\psi(\mathbf{r}) = \epsilon\psi(\mathbf{r}) \quad \mathbf{r} \in II \tag{2.3}$$

which matches in amplitude onto ϕ over the interface S between the two regions:

$$\phi(\mathbf{r}_s) = \psi(\mathbf{r}_s) \tag{2.4}$$

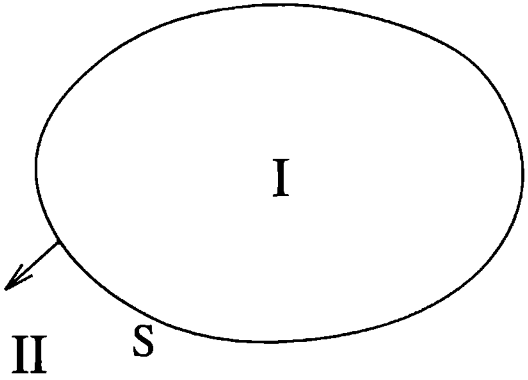

Figure 2.1: The region of interest I embedded onto the substrate II.

and satisfies prescribed boundary conditions at infinity.

In general we cannot match the normal derivative as well as the amplitude if ϕ is an arbitrary function. Therefore, we extend the class of our trial functions to include those which are continuous and smooth everywhere except at surface S where the normal derivative of Φ is allowed to have a jump across the interface. The corresponding variational principle is then given by:

$$E[\phi,\psi] = \frac{\int_I d\mathbf{r}\phi^* H\phi + \epsilon\int_{II} d\mathbf{r}\psi^*\psi + \frac{1}{2}\int_S d\mathbf{r}_s \left(\phi^*\frac{\partial\phi}{\partial n_s} - \psi^*\frac{\partial\psi}{\partial n_s}\right)}{\int_I d\mathbf{r}\phi^*\phi + \int_{II} d\mathbf{r}\psi^*\psi} \tag{2.5}$$

where n_s is the surface normal (from I to II) and the surface integral term in the numerator comes from the the effect of kinetic energy operator on the discontinuity in the normal derivatives $\partial\phi/\partial n_s$ and $\partial\psi/\partial n_s$ across the interface.

The fundamental principle of embedding is that the terms in (2.5) involving ψ can be eliminated in terms of ϕ and the parameter ϵ. To achieve this, we assume that we can define a generalised logarithmic derivative $\Sigma(\mathbf{r},\mathbf{r}';\epsilon)$ relating the normal derivative of ψ at S to its amplitude at this surface through:

$$\frac{\partial\psi(\mathbf{r}_s)}{\partial n_s} = -2\int_S d^2\mathbf{r}'_s\Sigma(\mathbf{r}_s,\mathbf{r}'_s;\epsilon)\psi(\mathbf{r}'_s) \qquad \mathbf{r}_S \text{ on } S. \tag{2.6}$$

We shall show how to construct Σ from the substrate Green function in the next section.

Making use of the above definition and the continuity assumption (2.4), we can write the normal derivative term in the numerator of (2.5) as:

$$-\frac{1}{2}\int_S d\mathbf{r}_s\psi^*\frac{\partial\psi}{\partial n_s} = \int_S d\mathbf{r}_s\int_S d\mathbf{r}'_s\phi^*(\mathbf{r}_s)\Sigma(\mathbf{r}_s,\mathbf{r}'_s;\epsilon)\phi(\mathbf{r}'_s). \tag{2.7}$$

To eliminate the remaining volume integrals, we differentiate equation (2.3) with respect to ϵ to obtain

$$[-\frac{1}{2}\nabla^2 + v_{eff}(\mathbf{r}) - \epsilon]\frac{\partial\psi(\mathbf{r})}{\partial\epsilon} = \psi(\mathbf{r}). \tag{2.8}$$

Multiplying this equation by ψ^* and the complex conjugate of (2.3) by $\partial\psi/\partial\epsilon$, subtracting the resulting equations and integrating through region II gives

$$\int_{II} d\mathbf{r}\psi^*\psi = -\frac{1}{2}\int_{II} d\mathbf{r}\left((\psi^*\nabla^2\frac{\partial\psi}{\partial\epsilon} - \frac{\partial\psi}{\partial\epsilon}\nabla^2\psi\right). \tag{2.9}$$

The use of Green's theorem converts the volume integral into a surface integral over S giving

$$\int_{II} d\mathbf{r}\psi^*\psi = \frac{1}{2}\int_S d\mathbf{r}_s\left(\psi^*\frac{\partial^2\psi}{\partial n_s\partial\epsilon} - \frac{\partial\psi^*}{\partial\epsilon}\frac{\partial\psi}{\partial n_s}\right). \tag{2.10}$$

The second term vanishes since $\psi(\mathbf{r}_s)$ is fixed by condition (2.4) and using (2.6) we end up with

$$\int_{II} d\mathbf{r}\psi^*\psi = -\int_S d^2\mathbf{r}_s\int_S d^2\mathbf{r}'_s\phi^*(\mathbf{r}_s)\frac{\partial\Sigma(\mathbf{r}_s,\mathbf{r}'_s;\epsilon)}{\partial\epsilon}\phi(\mathbf{r}'_s). \tag{2.11}$$

In this way we have eliminated all explicit references to the trial wavefunction outside the embedded region. The final expression for E becomes:

$$E[\phi,\epsilon] = \frac{\int_I d\mathbf{r}\phi^* H\phi + \frac{1}{2}\int_S d\mathbf{r}_s\phi^*\frac{\partial\phi}{\partial n_s} + \int_S d\mathbf{r}_s\int_S d\mathbf{r}'_s\phi^*\left[\Sigma - \epsilon\partial\Sigma/\partial\epsilon\right]\phi}{\int_I d\mathbf{r}\phi^*\phi - \int_S d\mathbf{r}_s\int_S d\mathbf{r}'_s\phi^*\partial\Sigma/\partial\epsilon\phi}. \tag{2.12}$$

This is a true variational principle in terms of the trial wavefunction ϕ and the parameter ϵ, giving an upper limit to the energy. By minimising E with respect to variations in ϕ and ϵ we obtain the solutions of the Schrödinger equation in I which matches *both* in amplitude and derivative onto the solution in II.

To derive an effective Schrödinger equation from the above variational principle we vary the trial function ϕ to minimise E obtaining

$$\begin{aligned}
[-\frac{1}{2}\nabla^2 &+ \frac{1}{2}\delta(\mathbf{n}-\mathbf{n}_s)\frac{\partial}{\partial\mathbf{n}_s} + v_{eff}(\mathbf{r})]\phi(\mathbf{r}) \\
&+ \delta(\mathbf{n}-\mathbf{n}_s)\int_S d^2\mathbf{r}'_s\left[\Sigma(\mathbf{r}_s,\mathbf{r}'_s;\epsilon) + (E-\epsilon)\frac{\partial\Sigma(\mathbf{r}_s,\mathbf{r}'_s;\epsilon)}{\partial\epsilon}\right]\phi(\mathbf{r}'_s) \\
&= E\phi(\mathbf{r}) \quad \mathbf{r}\in II,
\end{aligned} \tag{2.13}$$

where $\mathbf{n}$ is the component of $\mathbf{r}$ perpendicular to S. In the above equation, the normal derivative term inside the bracket ensures the Hermiticity of the kinetic energy operator for a finite system. More importantly, we see that the term inside the surface integral acts as a non-local energy-dependent potential – the embedding potential - incorporating the effect of the substrate into the Schrödinger equation. Note that the variational parameter ϵ appearing in the embedding potential $\Sigma(\mathbf{r}_s,\mathbf{r}'_s;\epsilon)$ is still undetermined and the term inside the integral is the linearisation of $\Sigma(\mathbf{r}_s,\mathbf{r}'_s;E)$ around this parameter:

$$\Sigma(\mathbf{r}_s,\mathbf{r}'_s;E) \approx \Sigma(\mathbf{r}_s,\mathbf{r}'_s;\epsilon) + (E-\epsilon)\frac{\partial\Sigma(\mathbf{r}_s,\mathbf{r}'_s;\epsilon)}{\partial\epsilon}. \tag{2.14}$$

Varying ϵ to make $E[\phi,\epsilon]$ stationary, gives the additional condition:

$$(E-\epsilon)\int_S d^2\mathbf{r}_s \int_S d^2\mathbf{r}'_s\phi^*(\mathbf{r}_s)\frac{\partial^2\Sigma(\mathbf{r}_s;\mathbf{r}'_s;\epsilon)}{\partial\epsilon^2}\phi(\mathbf{r}'_s). \tag{2.15}$$

This is fulfilled if we take

$$\epsilon = E \tag{2.16}$$

or otherwise at those values of ϵ for which

$$\frac{\partial^2\Sigma(\mathbf{r}_s,\mathbf{r}'_s;\epsilon)}{\partial\epsilon^2} = 0. \tag{2.17}$$

It seems, therefore, that two classes of solutions are possible, one corresponding to (2.16) and the other to (2.17). Below, we show that (2.16) together with equation (2.13) results in an admissible solution of the Schrodinger equation in the whole space. This excludes the second class obtained from (2.17) since for a given set of boundary conditions, the variational problem (2.2) has a unique solution.

Inserting (2.16) into equation (2.13) results in the simpler equation

$$[-\frac{1}{2}\nabla^2 + v_{eff}(\mathbf{r}) - E]\phi(\mathbf{r}) + \delta(\mathbf{n}-\mathbf{n}_s)[\frac{1}{2}\frac{\partial\phi(\mathbf{r}_s)}{\partial\mathbf{n}_s} + \int_S d\mathbf{r}'_s\Sigma(\mathbf{r}_s,\mathbf{r}'_s;E)\phi(\mathbf{r}'_s)] = 0. \tag{2.18}$$

This is satisfied if ϕ is a solution of the ordinary Schrödinger equation at energy E

$$[-\frac{1}{2}\nabla^2 + v_{eff}(\mathbf{r})]\phi(\mathbf{r}) = E\phi(\mathbf{r}) \quad \mathbf{r}\in I \tag{2.19}$$

inside the embedded region and satisfies the *non-local* boundary condition

$$\frac{\partial\phi(\mathbf{r}_s)}{\partial n_s} = -2\int_S d^2\mathbf{r}'_S\Sigma(\mathbf{r}_s,\mathbf{r}'_s;E)\phi(\mathbf{r}'_s) \qquad \mathbf{r}_S \text{ on } S. \tag{2.20}$$

But with $\epsilon = E$, it follows from (2.6) that ψ also satisfies this condition. We see that ϕ and ψ satisfy the Schrödinger equation at the same energy E in their regions of definition and join smoothly together (i.e. with continuous amplitude and derivative) on S. Therefore, the composite wavefunction Φ is an admissible function everywhere and satisfies the Schrodinger equation over the whole space. It thus *minimises* the expectation value of the total Hamiltonian equation (2.2) and is the desired function. Consequently, the second class of functions corresponding to condition (2.18) can be safely disregarded. [1]

As it stands (2.18) is a non-linear eigenvalue equation which has to be solved by some iterative technique, requiring the knowledge of Σ over a range of trial energies. However, the quantity in which we are really interested is the one-particle Green function which is the solution of:

$$\begin{aligned} &[-\frac{1}{2}\nabla^2 + v_{eff}(\mathbf{r}) - E]G(\mathbf{r},\mathbf{r}';E) \quad + \\ &\delta(\mathbf{n}-\mathbf{n}_s)[\frac{1}{2}\frac{\partial G(\mathbf{r}_s,\mathbf{r}';E)}{\partial\mathbf{n}_s} \quad + \quad \int_S d^2\mathbf{r}''_s\Sigma(\mathbf{r}_s,\mathbf{r}''_s;E)G(\mathbf{r}''_s,\mathbf{r}';E)] \\ &= \delta(\mathbf{r}-\mathbf{r}') \qquad \mathbf{r},\mathbf{r}'\in I. \end{aligned} \tag{2.21}$$

---

[1] Such spurious solutions can creep in because in setting up the variational principle (2.5), we widen the class of acceptable solutions to those with a discontinuous normal derivative at the interface

G can be calculated at any arbitrary energy and from G all quantities of interest such as charge density in the embedded region are obtained.

In our calculations we usually expand G in a basis $\{\chi_i(\mathbf{r})\}$

$$G(\mathbf{r},\mathbf{r}';E) = \sum_{ij} \mathcal{G}_{ij}(E)\chi_i(\mathbf{r})\chi_j^*(\mathbf{r}') \tag{2.22}$$

Inserting this expansion in (2.21) and integrating over the embedded region results then in the following matrix equation for the coefficients:

$$\sum_k [H_{ik} + (\Sigma(E))_{ik} - EO_{ik}]\,\mathcal{G}_{kj}(E) = \delta_{ij} \tag{2.23}$$

Here,

$$\begin{aligned}
H_{ik} &= \int_I d\mathbf{r}\chi_i^*(\mathbf{r})H\chi_k(\mathbf{r}) + \frac{1}{2}\int_S d\mathbf{r}_s\chi_i^*(\mathbf{r}_s)\frac{\partial\chi_k(\mathbf{r}_s)}{\partial n_s} && (2.24)\\
(\Sigma(E))_{ik} &= \int_S d\mathbf{r}_s \int_S d\mathbf{r}'_s\chi_i^*(\mathbf{r}_S)\Sigma(\mathbf{r}_s,\mathbf{r}'_s;E)\chi_k(\mathbf{r}'_s) && (2.25)\\
O_{ik} &= \int_I d\mathbf{r}\chi_i^*(\mathbf{r})\chi_k(\mathbf{r}). && (2.26)
\end{aligned}$$

H_{ik} is the matrix element of the Hamiltonian plus the surface derivative term; O_{ik} is the overlap matrix element in the embedded region. $(\Sigma(E))_{ik}$ is the matrix element of the embedding potential.

We note that in deriving the embedding equation (2.21), no assumption is made about the potential inside the embedded region and the character of the Green function. Thus to represent the Green function inside the embedded region, we have the freedom to choose *any* convenient set of basis functions as long as these functions represent a wide class of physically meaningful wavefunctions within the embedded region. The only assumption in making expansion (2.22) is that the basis functions do not satisfy any particular boundary condition on S, so that they have enough flexibility to span a wide range of values of $\phi(\mathbf{r}_s)$ and $\partial\phi(\mathbf{r}_s)/\partial n_s$.

Having obtained an effective Schrödinger equation, we now turn to constructing the substrate embedding potential $\Sigma(\mathbf{r}_s,\mathbf{r}'_s;E)$ entering this equation.

2.2 The embedding potential and its properties

The embedding potential is directly related to the substrate Green function. To show this let $v_b(\mathbf{r})$ be the unperturbed potential of the substrate, i.e.

$$v_{eff}(\mathbf{r}) = v_b(\mathbf{r}) \qquad \mathbf{r} \in II, \tag{2.27}$$

ϕ a wavefunction satisfying the Schrödinger equation

$$[-\frac{1}{2}\nabla^2 + v_b(\mathbf{r}) - E]\phi = 0 \tag{2.28}$$

over the whole space and $G_b(\mathbf{r}, \mathbf{r}'; E)$ the corresponding Green function defined by:

$$[-\frac{1}{2}\nabla^2 + v_b(\mathbf{r}) - E]G_b(\mathbf{r}, \mathbf{r}'; E) = \delta(\mathbf{r} - \mathbf{r}') \tag{2.29}$$

and satisfying appropriate boundary conditions at infinity but no special condition on S. Multiplying (2.28) by G_b and (2.29) by ψ, subtracting the equations and integrating throughout region II gives:

$$\psi(\mathbf{r}) = -\frac{1}{2}\int_S d\mathbf{r}'_s \left(G_b(\mathbf{r}, \mathbf{r}'_s; E)\frac{\partial\psi(\mathbf{r}'_s)}{\partial n'_s} - \psi(\mathbf{r}'_s)\frac{\partial G_b(\mathbf{r}, \mathbf{r}'_s; E)}{\partial n'_s} \right) \tag{2.30}$$

where, again, Green's theorem is used to convert the volume integral into a surface integral. Now letting $\mathbf{r}$ approach the boundary from region II gives:

$$\psi(\mathbf{r}_s) = -\frac{1}{2}\int_s d\mathbf{r}'_s \left(G_b(\mathbf{r}_s, \mathbf{r}'_s; E)\frac{\partial\psi(\mathbf{r}'_s)}{\partial n'_s} - \psi(\mathbf{r}_s)\frac{\partial G_b(\mathbf{r}_s, \mathbf{r}'_s; E)}{\partial n'_s} \right) \tag{2.31}$$

This can be considered as an equation for $\partial\psi/\partial n_s$ in terms of $\psi(\mathbf{r}_s)$ which we can solve by introducing the surface inverse of our Green function, defined by:

$$\int_s d\mathbf{r}_s G_b^{-1}(\mathbf{r}''_s, \mathbf{r}_s; E) G_b(\mathbf{r}_s, \mathbf{r}'_s; E) = \delta(\mathbf{r}''_s - \mathbf{r}'_s). \tag{2.32}$$

Multiplying (2.31) by $G_b^{-1}(\mathbf{r}''_s; \mathbf{r}_s; E)$ and integrating over S gives:

$$\frac{\partial\psi(\mathbf{r}''_s)}{\partial n''_s} = -2\int_S d\mathbf{r}_s \left(G_b^{-1}(\mathbf{r}''_s, \mathbf{r}_s; E) - \frac{1}{2}\int_S d\mathbf{r}'_s G_b^{-1}(\mathbf{r}''_s, \mathbf{r}'_s; E)\frac{\partial G_b(\mathbf{r}'_s, \mathbf{r}_s; E)}{\partial n_s}) \right) \psi(\mathbf{r}_s) \tag{2.33}$$

Comparing this result with the definition of the embedding potential (2.6) shows that Σ is related to the substrate Green function and its surface inverse by:

$$\Sigma(\mathbf{r}_s, \mathbf{r}'_s; E) = G_b^{-1}(\mathbf{r}_s, \mathbf{r}'_s; E) - \frac{1}{2}\int_S d\mathbf{r}''_s G_b^{-1}(\mathbf{r}_s, \mathbf{r}''_s; E)\frac{\partial G_b(\mathbf{r}''_s, \mathbf{r}'_s; E)}{\partial n'_s}. \tag{2.34}$$

Equation (2.34) becomes especially simple if the Green function is constructed such that it satisfies the (von Neumann) boundary condition on S [6]:

$$\frac{\partial G_b(\mathbf{r}''_s, \mathbf{r}'_s; E)}{\partial n'_s} = 0. \tag{2.35}$$

The embedding potential is then simply the surface inverse of the substrate Green function with zero normal derivative on the embedding surface. Denoting this Green function by G_N

$$\Sigma(\mathbf{r}_s, \mathbf{r}'_s; E) = G_N^{-1}(\mathbf{r}_s, \mathbf{r}'_s; E). \tag{2.36}$$

An alternative representation for $\Sigma(\mathbf{r}_s, \mathbf{r}'_s; E)$ can be obtained [9] by starting from (2.30) and taking the Green function which satisfies the Dirichlet boundary condition

$$G_D(\mathbf{r}, \mathbf{r}'; E) = 0 \qquad \mathbf{r} \text{ or } \mathbf{r}' \text{ on } S, \tag{2.37}$$

This yields

$$\psi(\mathbf{r}) = \frac{1}{2}\int_s d\mathbf{r}'_s \psi(\mathbf{r}'_s)\frac{\partial G_D(\mathbf{r},\mathbf{r}'_s;E)}{\partial n'_s}. \tag{2.38}$$

Taking the normal derivative with respect to r and letting r to approach the boundary from region II we find

$$\frac{\partial\psi(\mathbf{r}_s)}{\partial n_s} = \frac{1}{2}\int_s d\mathbf{r}'_s \left(\frac{\partial^2}{\partial n_s \partial n'_s} G_D(\mathbf{r}_s,\mathbf{r}'_s;E)\right)\psi(\mathbf{r}'_s) \tag{2.39}$$

which shows that the embedding potential can also be found from:

$$\Sigma(\mathbf{r}_s,\mathbf{r}'_s;E) = -\frac{1}{4}\frac{\partial^2}{\partial n_s \partial n'_s} G_D(\mathbf{r}_s,\mathbf{r}'_s;E). \tag{2.40}$$

Using the spectral representation of G_D we can write this as:

$$\Sigma(\mathbf{r}_s,\mathbf{r}'_s;E) = -\frac{1}{4}\frac{\partial^2}{\partial n_s \partial n'_s}\sum_n \frac{\psi_n(\mathbf{r}_s)\psi^*_n(\mathbf{r}'_s)}{E_n - E} \tag{2.41}$$

where ψ_n is an eigenfunction of the substrate Schrödinger equation satisfying the Dirichlet condition on S:

$$\psi_n(\mathbf{r}_s) = 0. \tag{2.42}$$

The analytical structure of the embedding potential is evident from (2.41): just like the substrate Green function, the embedding potential is analytical in the whole complex plane except on the real axis where it may have poles and/or branch cuts.

For an infinitely extended substrate, the substrate Hamiltonian has a continuous spectrum and the embedding potential becomes complex for those energies which coincide with this continuum. With the embedding potential set to zero, a finite defect region (e.g. a slab or a cluster of atoms) will have a discrete energy spectrum. The complex character of the embedding potential, however, broadens these discrete states into the true continuum of the system coupled to the substrate. We note that discrete states of slab or cluster calculations are often broadened to simulate the effect of the substrate, However, unlike in the embedding method, this is usually done in an *ad hoc* way.

References

[1] P. Krüger and J. Pollmann Phys. Rev. Lett. **64**, 1808 (1990).

[2] P.J. Feibelman, Phys. Rev. B **35**, 2626 (1987).

[3] H.L. Skriver and N.M. Rosengaard, Phys. Rev. B **43**, 9583 (1991).

[4] B. Drittler, B. Weinert, M. Zeller and P.H. Dederichs, Phys. Rev. B **39**, 930 (1989).

[5] J.M. MacLaren, S. Crampin, D.D. Vvedensky and J.B. Pendry, Phys. Rev. B **40**, 12164 (1989).

[6] J.E. Inglesfield, J. Phys. C, 3795 (1981).

[7] J.E. Inglesfield and G.A. Benesh, Phys. Rev. B **37**, 6682 (1988).

[8] S. Crampin, J.A.B.N. van Hoof M. Nekovee and J.E. Inglesfield, J. Phys. C **4**, 1475 (1992).

[9] A.J. Fisher, J. Phys. C **2**, 6079 (1990).

Chapter 3

Full-potential embedding for surfaces and interfaces *

3.1 Introduction

Calculations of surface or interface electronic structure fall broadly into two categories, those which treat the semi-infinite substrate or substrates, and those which employ slab or supercell boundary conditions. In the latter, a surface is unphysically located in the vicinity of other surfaces, either across a region of vacuum and/or a finite number of atomic layers, but they have the benefit that conventional band structure techniques may be used. Indeed, they have achieved considerable success in the description of various surface properties, such as work functions, total energies, atomic reconstructions and magnetism, but their ability to describe individual states for comparison with surface spectroscopies such as photoemission and inverse-photoemission is less well established. Wavefunctions are far more sensitive to boundary conditions than integrated quantities such as charge densities and total energies, and may interact significantly over many atomic planes. In addition, both slabs and supercells provide a poor description of the bulk continuum.

Techniques which provide a correct description of the individual wavefunctions of the semi-infinite system and the bulk continuum are usually based upon the Green function and include multiple scattering methods such as layer Korringa-Kohn-Rostoker (LKKR) [1], where the semi-infinite substrate is incorporated via a reflection matrix which describes the scattering of electrons; tight-binding formulations which exploit the short-range nature of the overlap integrals [2]; the Green-function linear-muffin-tin-orbitals method (GF-LMTO) [3] in which structure constants within the tight-binding representation are short-ranged; and the surface embedding Green function method (SEGF) [4]. The SEGF method provides a full-potential solution of the Schrödinger equation within a limited region of space (containing the surface or interface), and the influence of the semi-

---

*Based on J. Phys. C 4, 1475 (1992) by: S. Crampin, J.B.A.N. van Hoof, M. Nekovee and J.E. Inglesfield.

infinite substrate is incorporated via an energy-dependent non-local embedding potential which ensures the surface wave-functions match correctly to bulk solutions. The embedding potential is a property of the substrate and need only be evaluated once for a given substrate direction (eg (111), (110), ...), but the energy dependence prevents linearisation (in common with the LKKR and GF-LMTO methods). However, only one or two atomic layers are normally required to model a metal surface — considerably fewer than for slab or supercell techniques in which the interaction between neighbouring surfaces must be kept to a minimum — and so in addition to the improved accuracy, the SEGF technique can be a computationally efficient approach to determining the electronic structure of surface and interfaces.

The embedding potential can be related to the reflection properties of the substrate. In previous applications this relationship has been used to determine the embedding potential for a semi-infinite "muffin-tin" substrate, in which the potential within the substrate is approximated by the spherical average within non-overlapping spheres centered upon the atomic sites and the volume average in the interstitial. The reflection matrix may then be determined by the well known techniques of LKKR or low-energy electron diffraction theory [5]. Whilst this provides an extremely convenient method for determining the embedding potential, the limitations are obvious in that however accurate the solution obtained within the surface or interface region, it is limited by errors in the embedding potential. The inherent difficulties become more severe the less close-packed the substrate is. An additional problem arises from the incompatibility of surface and substrate potentials, which can result in artificial charge transfer which reduces the stability of the self-consistent iteration scheme. Moreover, this can lead to spurious shifts in the determined position of surface states relative to bulk band edges.

In this chapter we describe a new approach by which the substrate embedding potential may be determined with an accuracy comparable to that achieved in the surface or interface region. Since the embedding potential need only be determined once, and subsequently read in when the surface potential is being iterated, we initially provide a justification for the use of an embedding *plane* to simulate embedding on a more complicated surface. This permits a simple representation of the embedding potential which is independent of the surface region, and requires significantly less memory storage than the use of a non-planar embedding surface. We then indicate how the embedding potential for an arbitrary stacking of atomic planes may be constructed and present an efficient algorithm for generating the embedding potential of a substrate with semi-infinite periodicity. Finally, we conclude with some remarks on how local properties within the surface or interface may be most efficiently determined.

3.2 Embedding on a plane

We showed in the previous chapter that a solution of the Schrödinger equation in the region of interest (region I in figure 3.1) which matches smoothly onto a solution in the

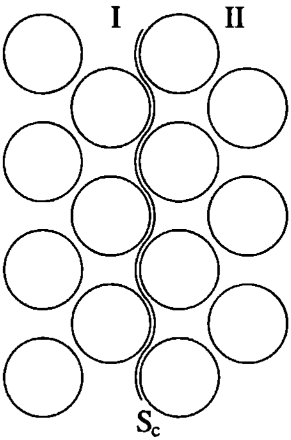

Figure 3.1: The region of interest I is separated from the substrate II by surface S_C.

substrate (region II) can be obtained by solving

$$H\phi = E\phi \tag{3.1}$$

explicitly in region I and imposing the condition

$$\frac{\partial\phi(\mathbf{r}_s)}{\partial n_s} = -2\int_{S_C} d^2\mathbf{r}'_s G_0^{-1}(\mathbf{r}_s, \mathbf{r}'_s)\phi(\mathbf{r}'_s) \qquad \mathbf{r}_s \text{ on } S_C. \tag{3.2}$$

on the normal derivative of ϕ across the boundary of this region, the surface S_C.

In the above formulation all information regarding the substrate enters through G_0^{-1}, the embedding potential, evaluated over S_C. However, this causes some problems when it comes to implementing the method in a particular basis, through difficulties in evaluating the surface integrals. A surface which respects the partitioning between substrate and surface atoms contains concave and convex sections where it curves around the muffin-tins (figure 3.2), whereas a plane surface, which permits a simple representation of the embedding potential, cuts through substrate muffin-tins, requiring the inclusion of substrate caps within the region I, and/or cuts through surface atoms, requiring the omission of surface atom caps. Inglesfield and Benesh [4] argued that it is possible to *transfer* the boundary condition contained in G_0^{-1} from the complicated surface which avoids cutting through muffin-tin spheres to a simpler planar surface, by integrating through a constant potential between the original surface and the new surface. We now show that this is indeed possible and show how the resulting embedding potential is obtained.

To do this we consider embedding our region of interest, I, onto free space, and determine under what conditions our trial solution ϕ is a solution of the Schrödinger equation within I with the correct boundary condition on S_C, the curvy surface, when the embedding surface is S, a plane. S_C separates regions I and Δ, and S regions Δ and II, and in region Δ we take the potential to be zero (figure 3.3). Let us define our trial solution

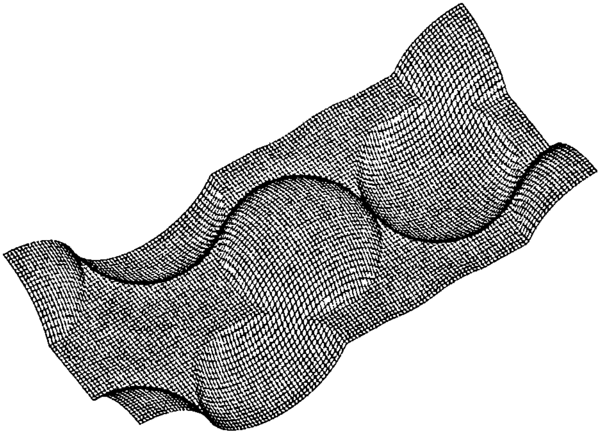

Figure 3.2: An embedding surface, in this case for fcc(210), which respects the partitioning of atoms into surface and substrate atoms in general consists of convex and concave caps due to protruding muffin-tins. Transferring the boundary condition from this complicated surface to a flat surface is greatly beneficial.

within I+Δ and match on S to χ, a solution of the free-electron Schrödinger equation at energy ε. As above the expectation value of the Hamiltonian is

$$E = \frac{\int_{I+\Delta} d^3\mathbf{r}\phi^* H\phi + \int_{II} d^3\mathbf{r}\chi^* H_0\chi + \frac{1}{2}\int_S d^2\mathbf{r}_s\,(\phi^*\partial\phi/\partial n_s - \chi^*\partial\chi/\partial n_s)}{\int_{I+\Delta} d^3\mathbf{r}\phi^*\phi + \int_{II} d^3\mathbf{r}\chi^*\chi}. \tag{3.3}$$

If G_F is the free-electron Green function with zero normal derivative on S, so that [6]:

$$\frac{\partial\chi(\mathbf{r}_s)}{\partial n_s} = -2\int_S d^2\mathbf{r}'_s G_F^{-1}(\mathbf{r}_s,\mathbf{r}'_s)\chi(\mathbf{r}'_s) \qquad \mathbf{r}_s \text{ on } S. \tag{3.4}$$

minimising (3.3) with respect to variations in ε gives

$$E = \frac{\int_{I+\Delta} d^3\mathbf{r}\phi^* H\phi + \frac{1}{2}\int_S d^2\mathbf{r}_s\phi^*\partial\phi/\partial n_s + \int_S d^2\mathbf{r}_s \int_S d^2\mathbf{r}'_s\phi^* G_F^{-1}\phi}{\int_{I+\Delta} d^3\mathbf{r}\phi^*\phi} \tag{3.5}$$

Varying ϕ, we find the energy is stationary when $H\phi = E\phi$ for $\mathbf{r}$ in region $I+\Delta$ and ϕ has the same logarithmic derivative on S as χ

$$\frac{\partial\phi(\mathbf{r}_s)}{\partial n_s} = -2\int_S d^2\mathbf{r}'_s G_F^{-1}(\mathbf{r}_s,\mathbf{r}'_s)\phi(\mathbf{r}'_s) \qquad \mathbf{r}_s \text{ on } S \tag{3.6}$$

We now note that in region Δ both ϕ and χ satisfy the free-electron Schrödinger equation. Thus, since they possess the same amplitude and derivative on S, they will possess the same amplitude and derivative on S_C. Hence, if we construct our free-electron solution

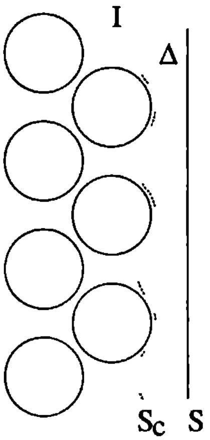

Figure 3.3: Embedding the region of interest (I) onto a free electron solution over surface S, with zero potential in the volume Δ between S and the true embedding surface, S_C. The conditions under which the trial solution has the correct boundary conditions over S_C lead to a prescription for determining the embedding potential on S.

χ to have the same logarithmic derivative as an exact bulk solution on S_C, on S it will have the necessary logarithmic derivative to ensure that ϕ too has the correct logarithmic solution on S_C. Since our trial solution also satisfies the Schrodinger equation in region I, it is by construction the solution we desire.

In the case of a substrate in which the true crystal potential is approximated by the muffin-tin form, in the (infinitesimal) region of zero potential between atoms of different layers (and in particular on surface S_C which curves around muffin-tins) a bulk wavefunction with wavevector $\mathbf{k}_\parallel$ may be written as

$$\begin{aligned}\psi(\mathbf{r}) &= \sum_{\mathbf{g}} \psi_{\mathbf{g}}(z)\, e_{\mathbf{g}}(\mathbf{r}_\parallel,\mathbf{k}_\parallel) \qquad e_{\mathbf{g}}(\mathbf{r}_\parallel,\mathbf{k}_\parallel) = \frac{1}{\sqrt{A}}\exp[i(\mathbf{g}+\mathbf{k}_\parallel)\cdot\mathbf{r}_\parallel] \\ \psi_{\mathbf{g}}(z) &= \sum_{\mathbf{g}'}\left[\delta_{\mathbf{gg}'}e^{ik_{\mathbf{g}z}z}+R_{\mathbf{gg}'}e^{-ik_{\mathbf{g}z}z}\right]a_{\mathbf{g}'} \qquad (3.7)\end{aligned}$$

where $k_{\mathbf{g}z} = \sqrt{2E-|\mathbf{g}+\mathbf{k}_\parallel|^2}$ and $R_{\mathbf{gg}'}$ is the reflection matrix of the semi-infinite half space. Since this is also a solution of the free-electron Schrodinger equation at energy E, if we continue this definition into the muffin-tin spheres and use this for χ, then our free-electron solution has the same logarithmic derivative on any surface within the interstitial region as the bulk wavefunction. If we assume the origin $z = 0$ is on the embedding plane, then from (3.4) we can construct the $\mathbf{k}_\parallel$ resolved embedding potential

$$\begin{aligned}G^{-1}_{F,\mathbf{k}_\parallel}(\mathbf{r}_\parallel,\mathbf{r}'_\parallel) &= \sum_{\mathbf{gg}'}(G^{-1}_{F,\mathbf{k}_\parallel})_{\mathbf{gg}'}\,e_{\mathbf{g}}(\mathbf{r}_\parallel,\mathbf{k}_\parallel)\,e^*_{\mathbf{g}'}(\mathbf{r}'_\parallel,\mathbf{k}_\parallel) \\ (G^{-1}_{F,\mathbf{k}_\parallel})_{\mathbf{gg}'} &= -\frac{ik_{\mathbf{g}z}}{2}\left[(1-R)\,(1+R)^{-1}\right]_{\mathbf{gg}'}. \qquad (3.8)\end{aligned}$$

This is the expression given by Inglesfield and Benesh [4].

It is relatively easy to show by matching Green functions that equation (3.8) represents an expansion on surface S of the surface-inverse of the free-space Green function with zero normal-derivative boundary conditions (on S) which integrated through to S_C coincides with the substrate Green function on this surface. Since both this Green function and our trial function satisfy the same differential equation within Δ, satisfying the modified boundary condition on S is entirely equivalent to satisfying the original boundary condition on S_C. Note that (3.7) is in fact a valid representation of a wavefunction outside any substrate (subject to in-plane periodicity requirements) truncated and matched onto free-space, so this argument is valid for general potentials.

In figure 3.3 we have considered the case when plane S lies entirely on the substrate side of surface S_C. In actual fact such a restriction is not necessary, and for example the plane S may be taken to be entirely on the surface side of S_C. Re-writing (3.5) as

$$E = \frac{\int_I d^3\mathbf{r}\phi^* H\phi + \int_\Delta d^3\mathbf{r}\phi^* H_0\phi + \frac{1}{2}\int_S d^2\mathbf{r}_s\phi^*\partial\phi/\partial n_s + \int_S d^2\mathbf{r}_s \int_S d^2\mathbf{r}'_s\phi^* G_F^{-1}\phi}{\int_I d^3\mathbf{r}\phi^*\phi + \int_\Delta d^3\mathbf{r}\phi^*\phi} \tag{3.9}$$

to distinguish integration volumes, we note that when S is not entirely on the substrate side of S_C, in this case Δ and I overlap. However, since we are attempting to minimise (3.9), we are free to use different expansions of the trial function for Δ and I. Thus within I, which includes the contribution from the atomic potentials, we can use the conventional linearised augmented plane-wave basis (LAPW) with an expansion in solutions of the atomic Schrödinger equation within the muffin-tins, whilst in Δ, and on surface S, we can use the plane wave component of the LAPW. The resulting matrix elements are then particularly easy to determine.

To demonstrate the validity of the use of a plane embedding surface, we consider the case of an internal interface, a Cu/Ni/Cu (100) monolayer sandwich (figure 3.4). Embedding an internal interface is essentially the two-surface generalisation of the previous analysis [8]. The effective Schrödinger equation is obtained by minimising (cf (3.5))

$$\begin{aligned} E = \quad & \Big[\int_{I+\Delta^L+\Delta^R} d^3\mathbf{r}\phi^* H\phi + \tfrac{1}{2}\int_{S^L} d^2\mathbf{r}_s\phi^*\partial\phi/\partial n_s + \tfrac{1}{2}\int_{S^R} d^2\mathbf{r}_s\phi^*\partial\phi/\partial n_s + \\ & \int_{S^L} d^2\mathbf{r}_s \int_{S^L} d^2\mathbf{r}'_s\phi^* G_L^{-1}\phi + \int_{S^R} d^2\mathbf{r}_s \int_{S^R} d^2\mathbf{r}'_s\phi^* G_R^{-1}\phi\Big] \Big/ \int_{I+\Delta^L+\Delta^R} d^3\mathbf{r}\phi^*\phi \end{aligned} \tag{3.10}$$

where Δ^L (Δ^R) is the volume between the curvy embedding surface S_C^L (S_C^R) and the embedding plane S^L (S^R). G_L^{-1} and G_R^{-1} are the embedding potentials of the left and right half-spaces which produce the correct logarithmic derivative on the true embedding surfaces. We expand ϕ in an LAPW basis $\{\chi_i(\mathbf{r};\mathbf{k}_{||})\}$ and by varying the coefficients to minimise E, obtain an effective Schrödinger equation. The corresponding Green function is given at energy E by

$$G(\mathbf{r},\mathbf{r}';\mathbf{k}_{||}) = \sum_{i,j} \mathcal{G}_{ij}(\mathbf{k}_{||})\chi_i(\mathbf{r};\mathbf{k}_{||})\chi_j^*(\mathbf{r}';\mathbf{k}_{||}) \tag{3.11}$$

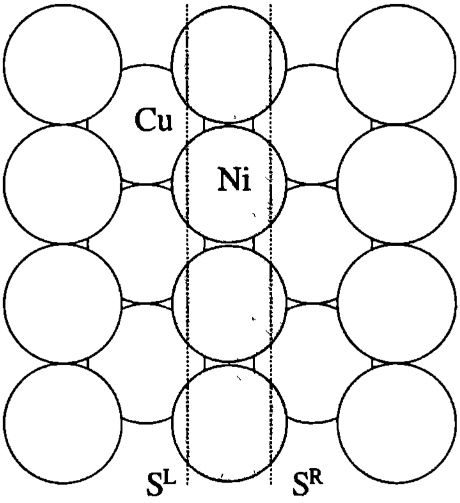

Figure 3.4: The embedding of a (100) Ni monolayer in Cu. The Cu substrates are replaced by embedding potentials on the planes S_L and S_R. For the examples described in the text, the planes cut through both Ni and Cu muffin-tins.

where the matrix of coefficients is given by

$$\mathcal{G} = \left[H + C^{\dagger}_{S^L}(G^{-1}_{L,\mathbf{k}_{\|}})C_{S^L} + C^{\dagger}_{S^R}(G^{-1}_{R,\mathbf{k}_{\|}})C_{S^R} - EO\right]^{-1} \tag{3.12}$$

$$H_{ij} = \int_{I+\Delta^L+\Delta^R} d^3\mathbf{r}\chi_i^* H\chi_j + \frac{1}{2}\int_{S^L} \chi_i^* \frac{\partial\chi_j}{\partial n_s} + \frac{1}{2}\int_{S^R} \chi_i^* \frac{\partial\chi_j}{\partial n_s} \tag{3.13}$$

$$(C_S)_{\mathbf{g}i} = \int_S d^2\mathbf{r}_s e^*_{\mathbf{g}}\chi_i \qquad O_{ij} = \int_{I+\Delta^L+\Delta^R} d^3\mathbf{r}\chi_i^*\chi_j. \tag{3.14}$$

The density of states is determined by integrating throughout the muffin-tin spheres the local density of states, obtained from $\varrho(\mathbf{r};\mathbf{k}_{\|}) = \mathrm{Im}G(\mathbf{r},\mathbf{r};\mathbf{k}_{\|})/\pi$. Figure 3.5 shows a comparison of the density of states within the Ni muffin-tin evaluated using the above formalism, with various positions of the embedding planes, and that determined by the LKKR method (see MacLaren [1] for further details of this part of the calculation) using an identical potential. We have used muffin-tin potentials for this comparison, bulk Cu potentials in the Cu substrate right up to the interface and a bulk Ni potential within the Ni monolayer. As in the conventional KKR method of band structure theory, the LKKR code uses a free space expansion within the interstitial and is thus exact for potentials of the muffin-tin form, spherically symmetric within non-overlapping spheres, zero elsewhere. The embedded Green function technique should be exact for all forms of potential, and so we expect both methods to comparable results. Despite the completely different approaches employed by the two methods, the LKKR results and those using embedding are in excellent agreement, indicating the validity of the use of a plane embedding surface.

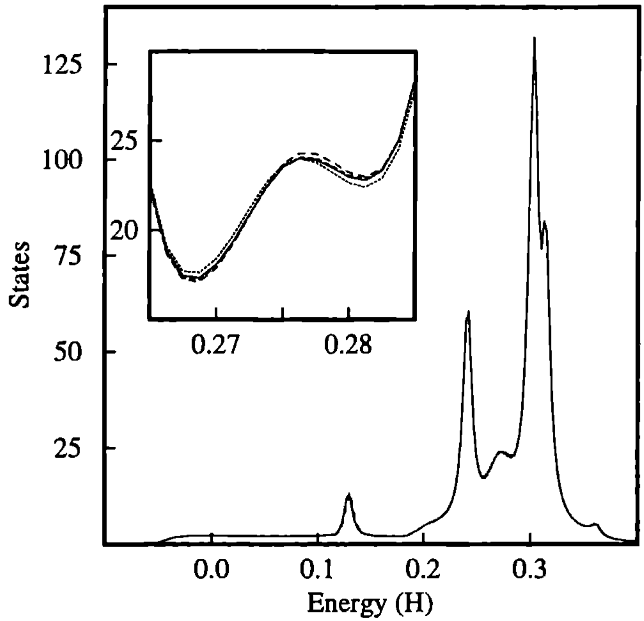

Figure 3.5: Muffin-tin density of states at $\mathbf{k}_{||} = (0, 0)$ (per spin-Hartree) for a (100) Cu/Ni/Cu sandwich. Four curves are plotted. The solid line is the LKKR results. The dashed curves are calculated with the embedded Green function method with the embedding planes at (short dash to long) 0.50, 0.55 and 0.60 times the interlayer separation. The results show remarkable agreement, as is evident from the inset which shows a section of the curve in detail. The density of states calculated within the varying embedded region as a whole differs by as much as 30% between the different embedding plane calculations. The energy contained an imaginary component of 0.005 H.

Note that we are comparing the muffin-tin density of states. By moving the embedding planes, the total density of states within the embedded region as a whole varies by virtue of the variation in the volume, but the contribution from the muffin-tin is constant. The remaining differences are numerical (for example, the two codes use different radial tabulations of the potentials) and finite basis sets (the LKKR calculations used 29 $\mathbf{g}$ vectors and ℓ up to 3; the LAPW basis consisted of 160 vectors, angular momentum expansions to $\ell = 8$ and the embedding potential was expanded with 29 reciprocal lattice vectors).

Our experience is that this degree of agreement does not extend indefinitely as the embedding planes are moved either toward the substrate or the Ni monolayer. In both cases differences appear at specific energy regions which increase as the embedding plane approaches the atomic planes. Those elements of the embedding potential which correspond to $\mathbf{g}$ with $|\mathbf{g} + \mathbf{k}_{||}|^2 > 2E$ vary exponentially with changes in the position of the embedding plane, and not only does the number of basis vectors required in the expansion (3.8) rapidly increase but errors increase due to the integration back and forth from the embedding plane to the embedding surface. It is evident from figure 3.4 that for an interface between materials of similar atomic size, an embedding plane midway between atomic planes minimises the distance over which the boundary condition is transferred, and other than to demonstrate the validity of the embedding procedure there is little need to consider alternative embedding positions.

One further problem, also occurring for general potentials, arises from the poor behaviour of the **g** basis for the expansion of the embedding potential as the interlayer separation decreases. This is analogous to the difficulties experienced with the LKKR technique in similar situations, where the **g** basis is used as an intermediate expansion of the propagator connecting sites in different layers. The importance of additional basis vectors decreases exponentially at a rate dependent upon the interlayer spacing *and* $|\mathbf{g}|$; since small interlayer spacings generally correspond to large reciprocal lattice meshes, the problems are particularly acute, and may only be overcome by using an alternative expansion basis for the problematic terms. Here, the solution is to augment the surface plane wave expansion (3.8) with additional functions.

3.3 Full-potential embedding

We now consider how to determine a substrate embedding potential which goes beyond the muffin-tin approximation. As mentioned previously, the accuracy of solution within the surface or interface is limited by the errors present in the embedding potential. Although screening lengths within metals are sufficiently short for the effects of these errors to be small, the materials which may be studied are largely restricted to those which have a relatively close-packed crystal structure. Even then, the anisotropy of the charge distribution within the vicinity of the embedding plane can be underestimated due to matching onto a muffin-tin potential, and a small degree of charge transfer between the substrate and embedded region, due to the incompatible potentials, can result in decreased stability during the self-consistent iterations and shifts in the location of surface/interface states.

It was established in the previous section that it is possible to embed on a plane surface and take matrix elements of the embedding potential with the plane wave component of the LAPW when the embedding potential is obtained from the substrate Green function, integrated through zero potential between the curvy embedding surface which avoids cutting muffin-tins and the embedding plane, and which has zero-normal derivative on this plane. Consider the right half space. Given an embedding potential, $G^{-1}_{R,\mathbf{k}_\parallel}$, we can add on an additional volume I and determine the Green function, G, using equations (3.11) and (3.12), where we leave $G^{-1}_{L,\mathbf{k}_\parallel}$ unspecified at present. This Green function is the projection within I of the Green function which satisfies the full Schrödinger equation within I + substrate, and within Δ^L the free-electron Schrödinger equation. The presence of $G^{-1}_{L,\mathbf{k}_\parallel}$ acts as a second boundary condition on G, constraining the normal derivative. Therefore, if we specify $G^{-1}_{L,\mathbf{k}_\parallel} = 0$ on surface S^L, G is the Green function for I + substrate which has zero normal-derivative boundary condition on S^L and G^{-1}

is therefore an embedding potential for $I+$ substrate. If we add an additional volume, I', so that S'^R and Δ'^R are coincident with the previous surface S^L and volume Δ^L, the zero normal-derivative boundary condition integrated from S'^R through Δ'^R results in the same boundary condition on $S_C'^R = S_C^L$ as was integrated through Δ^L to give it. Thus the resulting Green function is smooth and continuous over all $I' + I +$ substrate and satisfies the Schrödinger equation in that volume. This procedure can then be repeated, the embedding potential describing the original substrate plus the additional volumes. If a muffin-tin substrate was employed originally, adding regions in which a full potential description of the potential of the same material is used will decrease the errors in the embedding potential. Alternatively, starting from some arbitrary embedding potential, the zero matrix for example, and repeatedly adding identical volumes representing substrate atomic planes till convergence, will generate a full potential substrate embedding potential.

To see how this works in practice, we expand the Green function (3.11) on surface S^L when $G^{-1}_{L,\mathbf{k}_\parallel} = 0$ and invert to give the new embedding potential for the substrate plus one additional layer:

$$\begin{aligned}
G^{-1}_{\mathbf{k}_\parallel}(\mathbf{r}_\parallel, \mathbf{r}'_\parallel) &= \sum_{\mathbf{g}\mathbf{g}'} (G^{-1}_{\mathbf{k}_\parallel})_{\mathbf{g}\mathbf{g}'} e_{\mathbf{g}}(\mathbf{r}_\parallel, \mathbf{k}_\parallel) e^*_{\mathbf{g}'}(\mathbf{r}'_\parallel, \mathbf{k}_\parallel) \\
(G^{-1}_{\mathbf{k}_\parallel})_{\mathbf{g}\mathbf{g}'} &= \left[C_{S^L} \mathcal{G} C^\dagger_{S^L} \right]^{-1} \\
\mathcal{G} &= \left[H + C^\dagger_{S^R} (G^{-1}_{R,\mathbf{k}_\parallel}) C_{S^R} - EO \right]^{-1}.
\end{aligned} \tag{3.15}$$

Repeating this procedure allows the evaluation of the embedding potential for an arbitrary stacking of atomic planes.

If the layers are identical and any parallel translation ($\mathbf{R}_\parallel$) from layer to layer is incorporated within the embedding potential, the Hamiltonian and overlap matrices are unchanged. Thus the embedding potential with $n+1$ layers is related to that for n layers by

$$(G^{-1}_{R,\mathbf{k}_\parallel})^{n+1} = E_{\mathbf{R}_\parallel} \left[C_{S^L} \mathcal{G}^n C^\dagger_{S^L} \right]^{-1} E^\dagger_{\mathbf{R}_\parallel} \tag{3.16}$$

where

$$\left[E_{\mathbf{R}_\parallel} \right]_{\mathbf{g}\mathbf{g}'} = \delta_{\mathbf{g}\mathbf{g}'} e^{i\mathbf{g}\cdot\mathbf{R}_\parallel}. \tag{3.17}$$

Repeated iteration of (3.16) ultimately results in an embedding potential for a semi-infinite substrate. In effect the substrate is being assembled layer by layer, so although the procedure is guaranteed to converge (in the presence of a finite imaginary component in the energy), typically the addition of many hundred of layers is needed. This is analogous to the construction of the reflection matrix in LKKR or the low-energy electron diffraction problem, where more efficient algorithms such as layer doubling are used to accelerate the convergence. Here, too, layer stacking does not constitute a practical algorithm for generating the embedding potential. However, we can develop a more efficient algorithm by defining

$$F^n = (G^{-1}_{R,\mathbf{k}_\parallel})^n - E_{\mathbf{R}_\parallel} \left[C_{S^L} \mathcal{G}^n C^\dagger_{S^L} \right]^{-1} E^\dagger_{\mathbf{R}_\parallel} \tag{3.18}$$

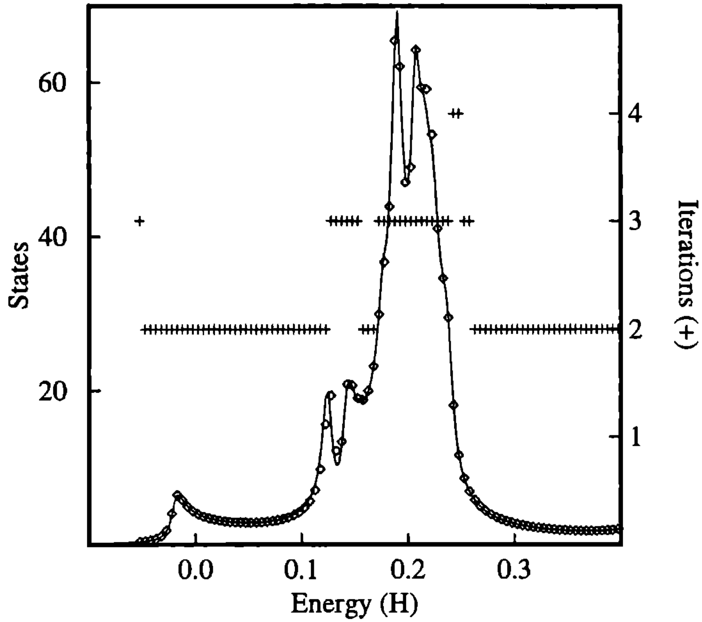

Figure 3.6: Muffin-tin density of states of bulk Cu at $\mathbf{k}_{\parallel} = (0.1, 0.2)$ a.u. (per spin-Hartree) with (100) taken as the normal direction. The solid line is the result obtained with LKKR theory. The diamonds indicate values obtained by embedding a single (100) monolayer of Cu, the embedding potentials having been found using the iterative algorithm described in the text (equations (3.18)-(3.25)). The number of iterations required to converge the embedding potential, indicated by +'s, are also discussed in the main text. Calculation parameters and imaginary energy were identical to the Cu/Ni/Cu sandwich calculation.

so that $F^n = 0$ defines the semi-infinite embedding potential. If $F^n \neq 0$ then we determine a new estimate

$$(G^{-1}_{R,\mathbf{k}_{\parallel}})^{n+1} = (G^{-1}_{R,\mathbf{k}_{\parallel}})^{n} - D^n \tag{3.19}$$

such that

$$F^{n+1} = 0. \tag{3.20}$$

Substituting (3.19) into (3.20) and retaining terms to first order in D^n gives

$$F^n = D^n - X^n D^n Y^n \tag{3.21}$$

$$X^n = E_{\mathbf{R}_{\parallel}} \left[C_{SL} \mathcal{G}^n C^{\dagger}_{SR} \right]^{-1} \tag{3.22}$$

$$Y^n = \left[C_{SR} \mathcal{G}^n C^{\dagger}_{SL} \right]^{-1} E^{\dagger}_{\mathbf{R}_{\parallel}} \tag{3.23}$$

where (3.21) may be solved by diagonalising X^n and Y^n [9]. In figure 3.6 we compare the density of states obtained with the LKKR code and that calculated by embedding with the embedding potentials determined using this new algorithm. In this case, the system studied is a (100) Cu monolayer with embedding potentials describing semi-infinite (100) Cu substrates - in effect, bulk Cu. The density of states is evaluated at $\mathbf{k}_{||} = (0.1, 0.2)$a.u., the embedding plane half-way between layers and the various parameters as before. Once again there is striking agreement between these two completely independent calculations. The iterative solution to (3.16)-(3.23) was obtained with the zero matrix as an initial guess for the lowest energy, and for subsequent energies (interval 0.005H) the embedding potential for the previous energy was the starting guess. We have found this to be the most efficient and stable procedure. As may be seen from figure 3.6, for most of the energy range only two iterations are necessary to converge the embedding potentials, and it is remarkable that halving the interval to 0.0025H between successive energies reduces this to one - in effect, providing more information for no extra cost. The number of iterations required rises when the nature of the states in that energy range is changing rapidly. What differences exist between the LKKR result and the embedded monolayer calculation are probably due to the LAPW basis, in which only two basis vectors correspond to each of the four largest expansion vectors of the embedding potential. We have found that by using the embedding potential obtained from the reflection matrix (equation (3.8)) as initial guess, our algorithm converges to the same embedding potential as before but in *three* iterations (for all the energies considered), with the largest changes occurring in precisely those matrix elements corresponding to large expansion vectors. As a word of caution, on occasions our algorithm has failed to pick up the correct solution, converging to an embedding potential which results in unphysical charge distributions. However, this has only ever occurred when our initial guess has been particularly poor, such as the zero matrix within the *d*-band. We have also established that this algorithm can evaluate the embedding potential at energies with arbitrarily small imaginary components, with little increase in the number of required iterations, thus permitting extremely detailed analysis of surface states.

3.4 Closing remarks

We have described how one may use an embedding plane to simulate embedding on a more complicated surface, and demonstrated the accuracy of such a procedure. The benefits arise from greatly simplified matrix elements, which may be evaluated with the plane-wave part of the LAPW basis functions. In addition, the embedding potential is a property of the substrate, independent of the surface or interface to which it is coupled. Therefore, it need only be evaluated once for a given substrate geometry and energy and wavevector, and for all subsequent uses it may be read in. It is a tremendous benefit to embed on a plane, as the expansion is compact.

We have then presented an algorithm for determining an embedding potential within the same framework as the subsequent evaluation of the surface or interface electronic structure. It is relatively easy to implement within the same program, and may be used to obtain an embedding potential with no shape approximation – unlike in previous

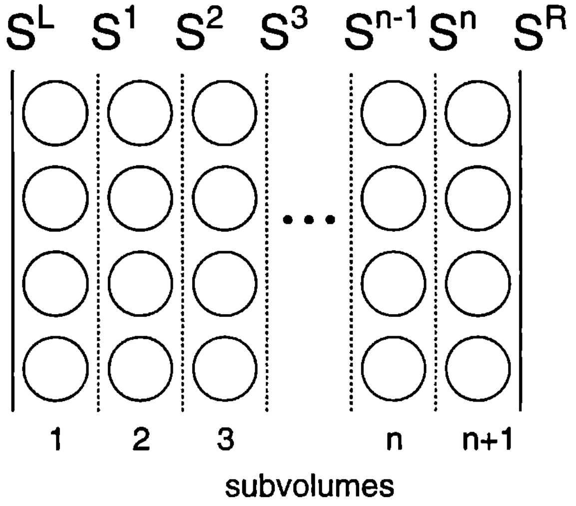

Figure 3.7: The atomic planes within the surface or interface region may be assigned to separate sub-volumes, and treated independently via embedding potentials.

applications of the embedding Green function method. The algorithm may be used to construct an embedding potential for an arbitrary arrangement of atomic planes – with the constraint that they possess the same in-plane periodicity – and in the case of a semi-infinite periodic substrate a particularly efficient iterative scheme has been described.

Even when the structural aspects of the surface or interface electronic structure problem are correctly treated, rather than approximated by slabs or supercells, the region of interest may contain a relatively large number of atoms. At a simple grain-boundary, for example, the electronic structure takes many atomic planes before it is bulk-like [7]. With the straightforward application of the LAPW basis to this problem, the calculation time scales roughly with the cube of the number of atomic planes, since matrix inversion is an N^3 process. However, it is possible to obtain local information such as the charge density more efficiently, through the embedding procedure. Consider the region of interest partitioned into subvolumes, $i = 1, 2, \cdots, n+1$, shown in figure. 3.7. A natural partitioning would assign one atomic plane to each subvolume, and at a surface the vacuum region would occupy one subvolume. The substrates have been removed and replaced by embedding potentials on S^L and S^R, in the case of a surface one of these being the free-electron or Coulomb embedding potential, depending upon the treatment of exchange and correlation. We now use (3.15) to obtain the embedding potential for substrate + volume 1, on surface S^1 which separates it from volume 2.

$$(G^{-1}_{L1,\mathbf{k}_\parallel})_{\mathbf{gg}'} = \left[C_{S^1}\left[H_1 + C^\dagger_{S^L}(G^{-1}_{L,\mathbf{k}_\parallel})C_{S^L} - EO_1\right]^{-1} C^\dagger_{S^1}\right]^{-1} \qquad (3.24)$$

Repeating, we can obtain all the necessary embedding planes for left embedding.

$$(G^{-1}_{L\imath,\mathbf{k}_\parallel})_{\mathbf{gg}'} = \left[C_{S^\imath}\left[H_\imath + C^\dagger_{S^{\imath-1}}(G^{-1}_{L(\imath-1),\mathbf{k}_\parallel})C_{S^{\imath-1}} - EO_\imath\right]^{-1} C^\dagger_{S^\imath}\right]^{-1} \tag{3.25}$$

The embedding planes for right embedding may be obtained by the reverse process, starting from the right substrate and adding additional volumes.

$$(G^{-1}_{Rn,\mathbf{k}_\parallel})_{\mathbf{gg}'} = \left[C_{S^n}\left[H_{n+1} + C^\dagger_{S^R}(G^{-1}_{R,\mathbf{k}_\parallel})C_{S^R} - EO_{n+1}\right]^{-1} C^\dagger_{S^n}\right]^{-1} \tag{3.26}$$

$$(G^{-1}_{R\imath,\mathbf{k}_\parallel})_{\mathbf{gg}'} = \left[C_{S^\imath}\left[H_{\imath+1} + C^\dagger_{S^{\imath+1}}(G^{-1}_{L(\imath+1),\mathbf{k}_\parallel})C_{S^{\imath+1}} - EO_{\imath+1}\right]^{-1} C^\dagger_{S^\imath}\right]^{-1} \tag{3.27}$$

These embedding potentials may then be used to embed the separate subvolumes and determine the charge density.

The benefit of this approach is that separate LAPW expansions may be made within each subvolume, and the corresponding matrix inversions are performed on considerably smaller matrices. Incorporating an additional atomic plane, assigned to a new sub-volume, does not increase the dimensions of the matrices to be inverted, and hence the approach has a linear scaling of the calculation time with the number of atomic planes. Of course one rarely gets something for nothing, and in this case the speed increase accompanies a loss of information. The off-diagonal elements of the Green-function in the position representation are no longer available over the whole region, but only within each separate subvolume.

References

[1] J.M. MacLaren, S. Crampin, D.D. Vvedensky and J.B. Pendry, Phys. Rev. B **40**, 12164 (1989).

[2] J. Pollmann and S.T. Pantelides, Phys. Rev, B **18** 5524 (1978).

[3] H.L. Skriver and N.M. Rosengaard, Phys. Rev. B **43**, 9538 (1991).

[4] J.E. Inglesfield and G.A. Benesh, Phys. Rev. B **37**, 6682 (1988).

[5] J.B. Pendry, *Low Energy Electron Diffraction* (Academic, London 1974).

[6] J.E. Inglesfield, J. Phys. C **14** , 3795 (1981).

[7] S. Crampin, D.D. Vvedensky, J.M. MacLaren and M.E. Eberhart, Phys. Rev. B **40**, 3413 (1989).

[8] C.P. Farquahar and J.E. Inglesfield, J. Phys. C **1**, 599 (1989).

[9] X.-G. Zhang, J.P. Rous, J.M. MacLaren, A. Gonis, M.A. Van Hove and G.A. Somerjai, Surf. Sci. **239**, 103 (1990).

Chapter 4

Subvolume embedding for interfacial electronic structure *

4.1 Introduction

In the previous chapter we proposed subvolume embedding as a new method capable of full-potential accuracy, which can treat semi-infinite substrates and which also has scaling of cpu/memory linear with the number of atomic planes. In this chapter we develop this approach further, and illustrate with some first applications.

4.2 Subvolume embedding

A technical outline of our method is given in [1]. The ideas have developed from the surface-embedded Green function (SEGF) method [2], and in particular the use of an embedding potential to constrain wavefunctions evaluated in a limited volume (the embedded region) to match correctly to substrate solutions of the one-electron Schrödinger equation. The embedding potential corresponds to the surface-inverse of the substrate Green function satisfying zero normal-derivative boundary conditions on the embedding surface. This observation leads to the following prescription for evaluating interfacial electronic structure. Beyond some distance to either side of the interface the crystal (or vacuum) potential is assumed unperturbed and is replaced by substrate embedding potentials (figure 3.7). The remaining atomic planes are partitioned into subvolumes. With reference to figure 3.7, the Green function in subvolume 1 is determined with the left substrate embedding potential applied on surface S^L and the embedding potential on surface S^1 set to zero. The resulting Green function matches correctly to the left substrate Green function, but has zero normal derivative on S^1 — so its surface inverse on S^1 is an embedding potential which can be used to constrain the Green function in subvolume 2 to match correctly to the Green function for the left substrate + subvolume 1. This procedure is

---

*Based on Surf. Sci. **287**, 732 (1993) by: S. Crampin, M. Nekovee, J.B.A.N. van Hoof and J.E. Inglesfield.

repeated recursively, producing successive embedding potentials for 'left' embedding, and then performed starting from the right with subvolume $n+1$ to derive embedding potentials for 'right' embedding. The final operation steps through the subvolumes determining the full Green function applying the relevant 'left' and 'right' embedding potentials on the embedding surfaces, thereby constructing a Green function expansion within each subvolume which correctly includes the influence of the surroundings.

Solving for the Green function involves a matrix inversion. With n subvolumes, this algorithm involves the determination of $2n-2$ embedding potentials (those of the left and right substrate are assumed known) and then n separate subvolume Green functions — in total $3n-2$ matrix inversions, the rate-limiting step in the computations. Note that with additional subvolumes the increase is linear, and each expansion is local to the particular subvolume so the matrix dimensions do not increase. Thus, in addition to correctly incorporating semi-infinite substrate boundary conditions, this method becomes increasingly efficient as the number of atomic planes increases when compared to conventional slab/supercell methods which use a single expansion which increases in dimension (matrix inversion scales with the cube of the dimension). Because the basis is not constructed to satisfy the boundary conditions, but does so 'variationally' via the constraint of the embedding potential, the number of basis functions per atom tends to be slightly greater than is employed in slab/supercell calculations where the basis functions automatically satisfy the artificial boundary conditions. Nevertheless, even for smaller systems, with no need to include buffer layers to reduce surface-surface interactions this approach can be efficient. For example, in the limit $n = 1$ we have recently used the SEGF method to determine the surface states/resonances on Ta(011), finding excellent agreement with experiment in essentially a one atom/unit cell calculation [3]. The use of basis sets such as the linear-augmented plane wave basis is relatively simple and permits the study of transition metal systems.

4.3 Application: stepped surface of jellium

To illustrate these ideas we consider the jellium model of metallic surfaces. This model, first treated self-consistently in the pioneering work of Lang and Kohn [4, 5], has since become a test bed for new surface calculation techniques and provides benchmark results with which to assess the accuracy of our method. We start with the standard planar surface model, with the ionic background charge density approximated by the form $n_+(\mathbf{r}) = \bar{n}\Theta(-z)$. The metallic substrate beyond -24 a.u. and the vacuum region beyond $+12$ a.u. are replaced by embedding potentials appropriate for electrons moving in a constant potential, in the latter case the value being determined self-consistently from the calculated dipole barrier during the iterative process. Figure 4.1 displays the results of two calculations where the embedded region of width 36 a.u. has been partitioned into 3 or 6 equal-sized subvolumes. The density profiles are essentially identical, and the positions of the embedding planes cannot be seen in any way as kinks or discontinuities. This shows how well the embedding potentials simulate the semi-infinite half-spaces on

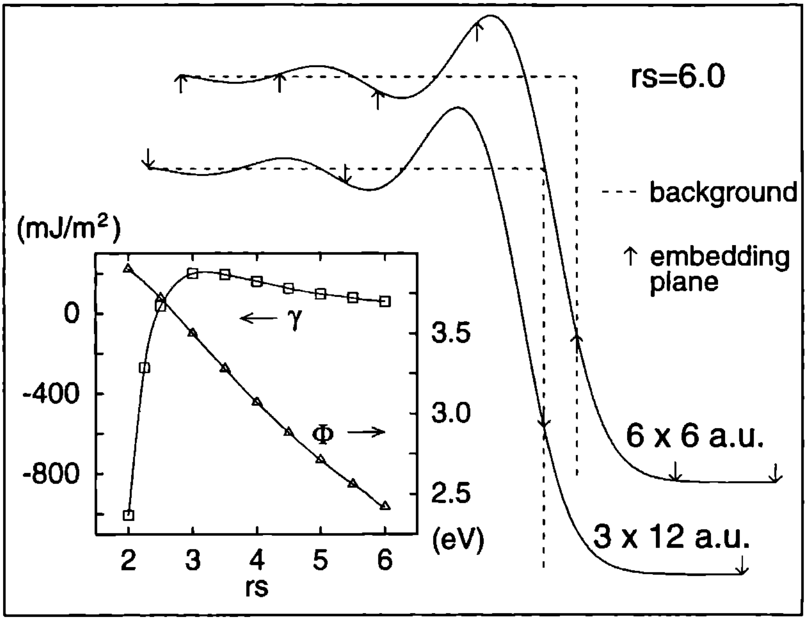

Figure 4.1: Planar jellium charge density profiles $r_s = 6$ calculated by subvolume embedding with 6 subvolumes each 6 a.u. wide and 3 subvolumes 12 a.u. wide. The position of the embedding planes in each calculation is indicated, along with the uniform positive background density. Inset: surface energies γ and work functions ϕ for the jellium surface calculated by subvolume embedding (using the Wigner exchange-correlation potential).

either side of each subvolume, and the accuracy of our procedure for recursively stepping across subvolumes. We have used 11 (7) z-dependent basis functions (sines/cosines defined over approximately twice the embedded length) in the 3 (6) subvolume calculations. Also shown on figure 4.1 are values for the work function and surface energy of the planar jellium surface, obtained from a series of similar 6-subvolume calculations. These are in complete agreement with the standard results, indicating that subvolume embedding is accurate on the scale of total energy calculations.

We now consider a stepped surface within the jellium approximation. All real surfaces exhibit imperfections such as steps, but their theoretical study represents an additional order of complexity over and above that of surfaces, which themselves have only become accessible to accurate electronic structure techniques within recent years. Here we treat the stepped surface Al(S)$-[m(111) \times (11\bar{1})]$ in the notation of Lang, Joyner and Somorjai [6], consisting of (111) terraces separated by monatomic steps of $(11\bar{1})$ orientation. This is modelled by jellium at $r_s = 2.07$ with the background density as illustrated in figure 4.2. Screening is particularly efficient at the high density corresponding to Al, and we treat an embedded region extending 12 a.u. into the metal and 12 a.u. into vacuum, partitioned into 4 subvolumes. Within each subvolume we use a basis set comprising of all combinations of 7 z-dependent functions and $2n_g+1$ periodic exponentials (n_g typically slightly larger than the terrace width index (figure 4.2) — convergence was checked). The direction parallel to the step edges is integrated out analytically.

The energy integrals required for evaluating the charge density are most efficiently calculated by contour integration since sharp structures and singularities in the Green function present on the real axis will be smoothed by going to complex energies . We evaluate these integrals along a semi-circular contour in the upper half energy-plane (32-point Gaussian- quadrature). The one-dimensional Brillouin zone integration are taken to convergence.

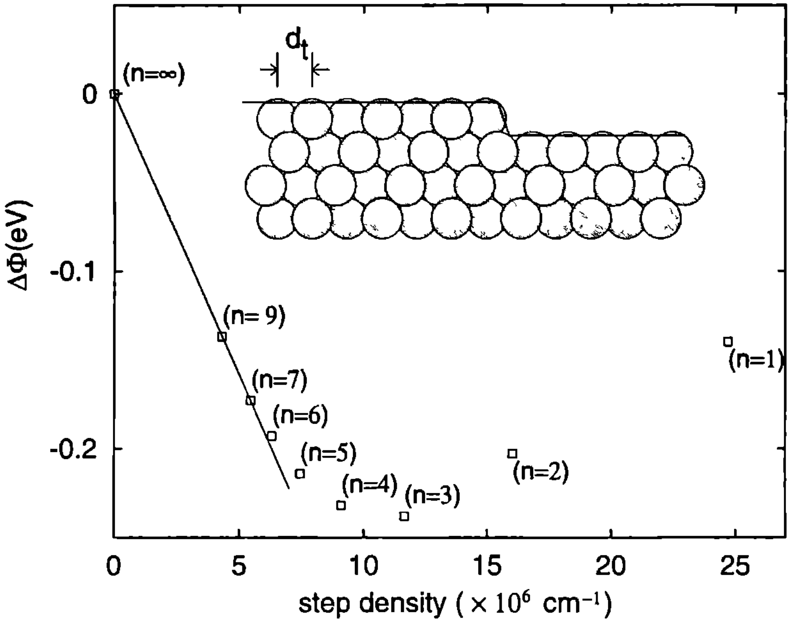

Figure 4.2: Work function variation ($\Delta\Phi$) with step density for the Al(111) surface with steps parallel to $[1\bar{1}0]$ and orientation $[11\bar{1}]$ calculated within the jellium approximation ($r_s = 2.07$). The step atomic-structure is illustrated and the jellium edge used to model it indicated. Alongside the calculated values are given the corresponding terrace widths in units of $d_t = 3/8a$ ($a = 4.05\AA$).

Figure 4.2 plots the work function against step density, n_s. As expected, the stepped surfaces exhibit a lower work function than the flat surface. This arises from the incomplete screening of the background density, with the electron density profile smoother than the background because of the high kinetic energy costs associated with more rapid variations. This results in the formation of a double-layer which lowers the work function. However, we find that the minimum work function is not associated with the shortest terrace width, but reaches a minimum for a width $3 \times \sqrt{3/8}a$ ($a = 4.05Å$). This effect is probably due to interference between screening parallel to the surface and perpendicular, although we have yet to fully analyse the cause. For $n_s \leq 6 \times 10^6$ cm^{-1} the work function varies linearly. This indicates that we have entered the asymptotic regime where there is no step-step interaction - and corresponds to separations greater than $4a$, or 4.6 Fermi wavelengths. In the linear regime we can associate a fixed dipole contribution to the work function arising from each step. Following Besocke, Krahl-Urban and Wagner [7] we can relate the work function variation and dipole moment via the Helmholtz equation $\Delta\Phi = 300 \times 10^{-18} 4\pi n_s \mu$ with $\Delta\Phi$ in eV, n_s the number of steps per cm and μ the dipole moment per cm step length in Debye. We find $\mu = 8.4 \times 10^6$Dcm^{-1}. Although comparison is premature, requiring a complete treatment of ion-core effects, it is interesting to note that our value is significantly closer to experimental values [7] for similar steps in Au (7.1×10^6Dcm^{-1}) with its closed d shell than Pt (18.8×10^6Dcm^{-1}) where more significant *d*-electron effects would be expected. We are not aware of experimental studies which have examined the onset of step-step interactions in workfunction measurements. We note that Ishida and Liebsch performed recently a similar theoretical study within the jellium model but for the stepped surface Al(S)$-$[m(001) $\times$ (100)] [8].

4.4 Summary

We have described subvolume embedding, a new approach to interfacial electronic structure calculations which combines full-potential accuracy with linear scaling of cpu/memory requirements. Calculations of the work function and surface energy of the jellium surface indicate the accuracy of the method, and we have applied the method to the stepped surface of jellium. The ability to prepare artificial sandwich and multilayer systems with novel electronic and magnetic properties, combined with advances in experimental techniques such as photoemission and inverse photoemission have opened up new areas of research for which subvolume embedding is ideally suited. Implementation of this method with the linear-augmented plane wave basis is currently underway.

References

[1] S. Crampin, J.B.A.N. van Hoof, M. Nekovee and J.E. Inglesfield, J. Phys. C **4**, 1475 (1992).

[2] J.E. Inglesfield and G.A. Benesh, Phys. Rev. B **37**, 6682 (1988).

[3] J.B.A.N. van Hoof, S. Crampin and J.E. Inglesfield, J. Phys. C **4**, 8477 (1992).

[4] N.D. Lang and W. Kohn, Phys. Rev. B **3**, 1215 (1971).

[5] N.D. Lang and W. Kohn, Phys. Rev. B **1**, 4555 (1970).

[6] B. Lang, R.W. Joyner and G.A. Somorjai, Surf. Sci. **30**, 440 (1972).

[7] K. Besocke, B. Krahl-Urban and H. Wagner, Surf. Sci. **68** 39 (1977).

[8] H. Ishida and A. Liebsch, Phys. Rev. B **46**, 7153 (1992).

Chapter 5

Embedding method for confined quantum systems *

5.1 Introduction

In this chapter we show how the embedding method [1], can be used to find the eigenstates of quantum systems confined by an effectively infinite potential barrier. There have been several papers recently on this type of problem, in particular for solving the Schrödinger equation for a H atom confined in cylindrical [2, 3, 4] and spherical [5, 6, 7] cavities. These have used trial wavefunctions vanishing on the boundary walls (the requirement on the exact solution of the problem) [2-5], non-vanishing basis functions with constraints that the trial function vanishes at a finite set of points [6], and a stationary principle due to Brownstein [7] for a trial function not necessarily vanishing on the boundary. The embedding method can tackle this class of problem, and it gives a minimum variational principle. Advances in nanostructure fabrication techniques mean that this is not of purely theoretical interest – for example the cylindrical confinement problem is relevant to an impurity atom in a quantum wire [4], and the spherical case to an impurity in a quantum dot [8].

5.2 Infinite barrier embedding

In the embedding method [1] we consider the region of interest I joined on to region II, and derive a variational principle for a trial function ϕ defined explicitly *only* in region I – the boundary condition that the wavefunction must be joined on to the solution of the Schrödinger equation in region II is replaced by additional boundary terms in the Hamiltonian for region I. The original motivation for this approach was to develop a method for solving the Schrödinger equation in a defect region of a solid, using basis functions of finite extent in the defect region (I) and the embedding potential taking care of the infinitely extended substrate (II). Here region I is the cavity, and the infinite potential

---

*Based on Phys. Rev. B **51**, 7318 (1995) by: S. Crampin, M. Nekovee and J.E. Inglesfield.

beyond the boundary of the cavity constitutes region II. The embedding potential cannot be defined for an infinite potential in II, and so to apply this method to confined systems we choose a constant but very large potential V in II. As a result, the variational principle will converge from above to the lowest eigenvalue of this system, but this will in principle lie *below* the true eigenvalue of the actual confined system, as there is slight leakage of the wavefunction out of I. We discuss below how this error may be assessed. The large potential leads to a great simplification in the embedding formalism. Let us consider for example confinement in a spherical cavity of radius R, for which the embedding potential can be expanded as a sum over spherical harmonics:

$$G_0^{-1}(\mathbf{r}_S,\mathbf{r}'_S) = \sum_L \mathcal{G}_L Y_L(\Omega) Y_L^*(\Omega'). \tag{5.1}$$

For large V $\mathcal{G}_L$ is given by

$$\mathcal{G}_L = \frac{\sqrt{2V}}{2R^2}\left[1 + \mathcal{O}\left(\frac{\epsilon}{V}\right)\right] + \mathcal{O}(1), \tag{5.2}$$

so

$$G_0^{-1}(\mathbf{r}_S,\mathbf{r}'_S) \approx \sqrt{\frac{V}{2}}\delta(\mathbf{r}_S - \mathbf{r}'_S). \tag{5.3}$$

Because $\partial G_0^{-1}/\partial\epsilon$ is negligible compared with G_0^{-1} for large V, the variational expression (2.12) then simplifies to

$$E = \frac{\int_I d^3r\phi H\phi + \int_S d^2r_S\left\{\frac{1}{2}\phi\frac{\partial\phi}{\partial n_S} + \sqrt{\frac{V}{2}}\phi^2\right\}}{\int_I d^3r\phi^2}. \tag{5.4}$$

This holds for a cavity of arbitrary shape, as minimizing E leads to a wavefunction ϕ not only satisfying the Schrödinger equation within I, but also satisfying

$$\frac{\partial\phi}{\partial n_S} = -\sqrt{2V}\phi \tag{5.5}$$

over S, which for large V and well-behaved functions means:

$$\phi(\mathbf{r}_S) \approx 0, \tag{5.6}$$

as we require.

In practice very large values of V can be used, so the error in the eigenvalue due to leakage can be made as small as we require. Furthermore, the error varies approximately as $1/\sqrt{V}$, and so extrapolation of the eigenvalue to complete confinement can be made. To show this behaviour, we consider ψ – the solution we require – which satisfies the Schrödinger equation in I with zero amplitude boundary condition on S at energy E_0. Then from Green's theorem the difference between E_0 and E, the energy of ϕ satisfying the Schrödinger equation with boundary condition (5.5), is given by

$$E_0 - E = \frac{-\frac{1}{2}\int_S d^2r_S\phi\frac{\partial\psi}{\partial n_S}}{\int_I d^3r\phi\psi}, \tag{5.7}$$

and using (5.5) this becomes

$$\begin{aligned} E_0 - E &= \frac{1}{2\sqrt{2V}} \frac{\int_S d^2r_S \frac{\partial\phi}{\partial n_S} \cdot \frac{\partial\psi}{\partial n_S}}{\int_I d^3r \phi\psi} \\ &\approx \frac{1}{2\sqrt{2V}} \int_S d^2r_S \left(\frac{\partial\psi}{\partial n_S}\right)^2 \end{aligned} \tag{5.8}$$

(assuming normalized wavefunctions). Hence we obtain a $1/\sqrt{V}$ variation, and knowing this error behaviour removes the apparent drawback of using a finite V.

5.3 Examples and conclusion

As a first example we consider the same model problem as Brownstein [7], a free electron in two dimensions confined within a quadrant of a circle with radius R. The exact solutions of this problem have the form (using cylindrical polar coordinates)

$$\phi_{p,k}(\rho, \theta) = J_p(\lambda_{p,k}\rho/R)\sin(p\theta), \tag{5.9}$$

where p is an even integer, J_p is a Bessel function and $J_p(\lambda_{p,k}) = 0$. The corresponding eigenenergies are [10]

$$E_{p,k} = \frac{1}{2}\left(\frac{\lambda_{p,k}}{R}\right)^2. \tag{5.10}$$

To test (5.4) we use the same basis functions as Brownstein, expanding ϕ in (5.4) in terms of

$$\psi_{m,n}(x, y) = \sin(m\pi x/R)\sin(n\pi y/R), \tag{5.11}$$

with m, n varying from 1 up to a maximum value M. These functions automatically satisfy the zero amplitude requirement over the straight lines $x = 0$, $y = 0$, and the integral over S in (5.4) reduces to a line integral over the perimeter of the quadrant.

Typical results for this system are shown in Fig. 5.1 where we study the second lowest eigenvalue obtained with various basis set dimensions and confining potentials, and we also compare with the estimates obtained using the stationary method derived by Brownstein [7]. Brownstein's method gives a variable number of ghost states below the ground state and so in this case we select the eigenvalue closest to the exact answer. We see uniform convergence in the embedding results with increasing basis set size, unlike the eigenvalues given by Brownstein's method from which it would be impossible to deduce an accurate eigenvalue. Estimates obtained using small confining potentials are better at small basis set sizes due to a cancellation of errors — leakage reduces the eigenvalue, whilst the variational solution means the result lies above that obtained with a larger basis set — but for large basis sizes the value converges *below* the exact eigenvalue. The inset shows the behaviour of the eigenvalue with confining potential, from which it is clear that the error due to leakage can be accurately estimated and corrected for.

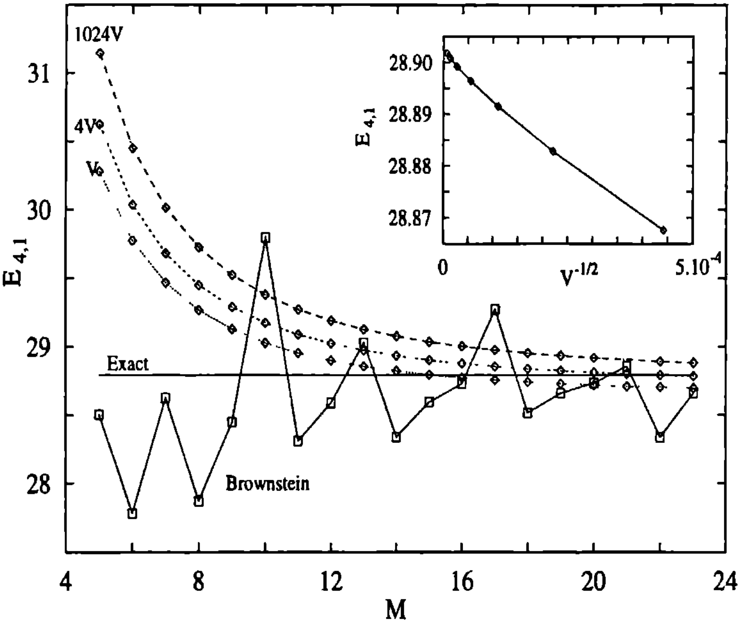

Figure 5.1: Variational estimates of the $E_{4,1}$ eigenstate (Eq. (11)) of a two-dimensional free electron confined to a quadrant of radius $R = 1$ a.u. Energies evaluated with the embedding method for confining potentials V, $4V$ and $1024V$, where $V = 8 \times 10^4$, are compared with those given by Brownstein's method (Ref. [7]) as a function of M (see text -- basis set size M^2). The inset shows the variation of the eigenvalue given by the embedding method with the confining potential V, for the basis set with $M = 22$. Similar behaviour occurs for smaller basis sets. The exact value of the eigenvalue is $E_{4,1} = 28.7915$.

Even for large basis sets the eigenvalues calculated for this problem retain considerable error. This is due to the choice of basis set, which does not contain sufficient flexibility to satisfy the zero amplitude boundary conditions. A better chosen basis set would greatly improve convergence. This is shown in a second more physical example which was also considered by Brownstein [7], and by Gorecki and Byers Brown [5] and Diamond, Goodfriend and Tsonchev [6], where a H atom is placed 0.5 a.u. off centre in a spherical cavity of radius 3 a.u. Our results are presented in Table 7.1 along with those of Brownstein, in both cases using the basis functions

$$u_{\alpha,\beta}(r,\theta) = e^{-r} r^{\alpha} \cos^{\beta}(\theta), \tag{5.12}$$

where r and θ are the radial and polar coordinate relative to the atom at the origin, and $\alpha = 0, 1, \ldots (N-1), \beta = 0, 1, \ldots (M-1)$. Both methods converge to the same ground state energy with rather few basis functions. The embedding results have been obtained with a confining potential of $V = 1.8 \times 10^9$ a.u. so that there is negligible error due to

Method	$N=2$	$N=4$	$N=6$
embedding	-0.31730(1)	-0.41323(1)	-0.41389(1)
Brownstein	-0.44906(1)	-0.41013(4)	-0.41389(7)

Table 5.1: Ground state energy (in a.u.) of a H atom displaced 0.5 a.u. off centre in a spherical cavity, radius 3 a.u. The embedding method results are calculated using Brownstein's basis set (Ref. [7]), with $M = N$ so the number of basis functions is N^2. V in Eq. (5) is taken to be 1.8×10^9 a.u. The number in brackets after the eigenvalue is the position of the eigenvalue as ordered by size.

leakage. Again they converge uniformly from above, unlike the estimates obtained by Brownstein. To conclude, we have shown how the embedding method can be used to find the eigenstates of confined quantum systems. Like the method due to Brownstein, in the embedding approach there is no need to construct basis functions which implicitly satisfy the boundary conditions — which can be difficult or impossible for complicated geometries — as the boundary condition is imposed as a variational constraint. In contrast to the method due to Brownstein embedding represents a true minimum principle, but, in addition to requiring the evaluation of similar volume integrals, also requires a sometimes tedious surface integral over S [11]. Interestingly enough, in the case of the Neumann boundary condition on S ($\frac{\partial\phi}{\partial n_S} = 0$), Brownstein's result [7] is the same as embedding (i.e. (2.12) with $G_0^{-1} = 0$) [12].

Finally, we would point out that ideal confinement is invariably a theoretical approximation, and that the embedding method can equally well handle less severe boundary conditions (e.g. those used in Ref. [8]).

References

[1] J.E. Inglesfield, J. Phys. C: Solid State Phys. **14**, 3795 (1981).

[2] G.W. Bryant, Phys. Rev. B **29**, 6632 (1984).

[3] J.W. Brown and H.N. Spector, J. Appl. Phys. **59**, 1179 (1986).

[4] P. Csavinszky and H. Oyoko, Phys. Rev. B **43**, 9262 (1991).

[5] J. Gorecki and W. Byers Brown, J. Phys. B: At. Mol. Opt. Phys. **22**, 2659 (1989).

[6] J.J. Diamond, P.L. Goodfriend and S. Tsonchev, J. Phys. B: At. Mol. Opt. Phys. **24**, 3669 (1991).

[7] K.R. Brownstein, Phys. Rev. Lett. **71**, 1427 (1993).

[8] J.L. Zhu and X. Chen, Phys. Rev. B **50**, 4497 (1994).

[9] M.I. Trioni, J.B.A.N. van Hoof, S. Crampin, G.P. Brivio and J.E. Inglesfield, Surface Sci. **307/309**, 41 (1994).

[10] The results presented in Table III of Ref. [7] are in Rydberg atomic units, 2 Rydbergs = 1 Hartree. In Ref. [7], the factor (1/2) in Eq. (20) and the factor 2 in Eq. (24) are incorrect and should be omitted.

[11] Note, however, with regard to Eq. (5), that $-\int u\nabla^2 v d\tau + \int u\nabla v\cdot d\mathbf{S} = \int(\nabla u)\cdot(\nabla v)d\tau$. This allows the surface integral involving the normal derivative — which will be especially difficult for complicated surfaces — to be combined with the kinetic energy term in H and replaced with a single volume integral. The remaining surface integral only involves the amplitude of the trial function on the surface.

[12] S. Crampin, J.B.A.N. van Hoof, M. Nekovee and J.E. Inglesfield, J. Phys.: Condens. Matter **4**, 1475 (1992).

Part II

Image potential states at real metal surfaces

Chapter 6

Introduction

At large distances from a metal surface the effective potential experienced by an electron has the asymptotic image form:

$$V_{im}(z) = E_v - \frac{1}{4|z - z_o|} \tag{6.1}$$

with E_v the vacuum level and z_o the image plane position. An electron can be trapped by this potential if its energy E lies below the vacuum level and it is reflected from the metal due to the lack of allowed bulk states in the range of its energy. This situation occurs when for a particular wave-vector parallel to the surface $\mathrm{k}_{||}$ there is a gap in the bulk band structure, a situation sketched in figure 6.1.

Note that the condition that there should be a band gap in the metal is not in contradiction with the fact that metals exhibit a continuum of allowed states below the Fermi energy E_F. This only holds if E is integrated over all $\mathrm{k}_{||}$ values. For particular directions in the surface Brillouin zone there may well be energy gaps. In fact noble metal and transition metal surface frequently have a gap in the (usually *sp* band) around the vacuum level [1].

At these surfaces the long range character of the image potential gives rise to a series of *unoccupied* electronic states that converge toward the vacuum level and are called *image states* or Rydberg surface states. The binding energy of these states are usually referred to the vacuum level and to a first approximation is given by a Rydberg-like series (at $\mathrm{k}_{||} = 0$)

$$E_n = E_v - \frac{1}{32n^2}. \tag{6.2}$$

An electron trapped in an image state is localised outside the surface and its wavefunction has only a small overlap with the supporting substrate. In the direction parallel to the surface the electron is delocalised and its motion is described by a Bloch wavefunction characterised by a two-dimensional Bloch wavevector.

Unlike other surfaces states, image states are induced by the long-range image tail of the surface barrier and are a *common feature* of all metallic surfaces. Even in the absence of a gap around the vacuum level, they may survive as image resonances: an

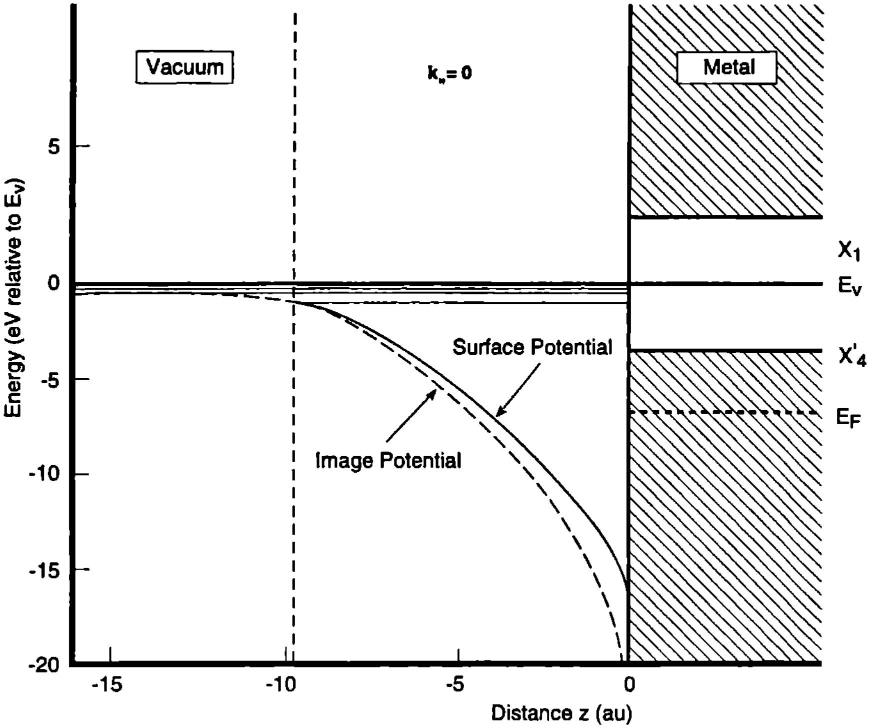

Figure 6.1: Schematic potential diagram for image-potential surface-states at Cu(001) indicating the surface-barrier, its asymptotic image tail and the projected bulk $s-p$ band gap for $\mathbf{k}_{\|} = 0$ (the $\bar{\Gamma}$ point of surface Brillouin zone). The shaded regions are continua of bulk states.

infinite series of states which can decay into the crystal but with an enhanced weight in the surface region.

The physics of image states is governed by the dual features of the long-range Coulomb interaction, which results in the image potential, and localisation at the surface. Thus these states are probes of many-body effects and electronic structure at and in the vicinity of the surface. The binding energies of such states provide information on the shape of the surface barrier [2, 3], from their lifetime broadening information about the nature of inelastic processes at the surface can be obtained [4] while from the convergence behaviour of their binding energies *local* changes in the workfunction can be detected [5]. In addition, when populated by a certain excitation process, image states form an ideal two-dimensional electron gas which is coupled only weakly to the substrate and provide a simple prototype system to study low-dimensional electron dynamics [6].

These unique features of Rydberg surface states have received wide attention from

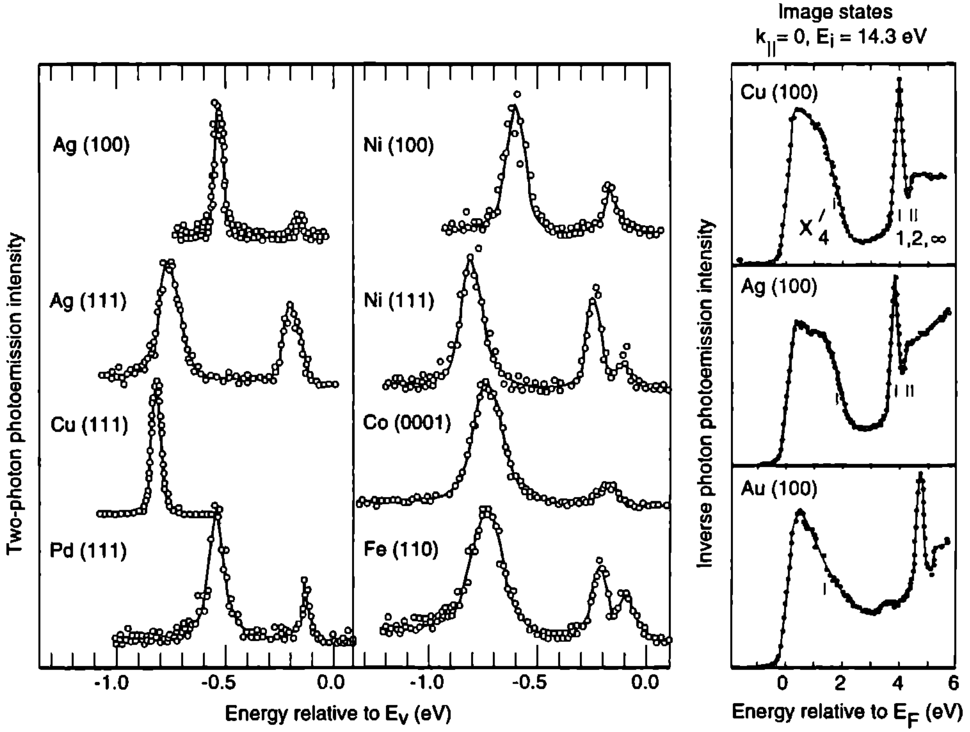

Figure 6.2: Inverse photoemission spectra (right) of image states at several metal surfaces [11]. The second hump above the $n = 1$ state is due to the higher states joined to the continuum of states above the vacuum level. The higher image states can be resolved using two-photon photoemission (left) which has a much higher energy resolution ($<$ 30 meV) [12].

both theory and experiment in recent years. On metals image states were first detected experimentally by low-energy electron diffraction (LEED) fine-structure analysis [7] and investigated in more details by the techniques of inverse photoemission (IPE) [1, 8, 9, 10], two-photon photoemission (2PPE) [12] and scanning tunneling microscopy (STM) [13]. These investigations have concentrated on the binding energy, effective mass, lifetime and the exchange splitting of these states on clean and adsorbate-covered surfaces.

Theoretically, Echenique and Pendry discussed the detection and existence of these states some years ago [14]. They viewed these states as standing wave resonances of an electron bouncing back and forth between the semi-infinite solid and the surface barrier in the direction normal to the surface and moving freely in the parallel direction. In this picture both the crystal and the barrier are simply characterised by complex electron reflectivities $r_c e^{i\phi}$ and $r_b e^{i\phi}$. By considering the round-trip phase accumulation ϕ of such an electron, they derived a Sommerfeld-like quantisation condition for the energy levels of an electron confined at the surface:

$$\phi(\epsilon) = \phi_c(\epsilon) + \phi_b(\epsilon) = 2\pi n \tag{6.3}$$

where n is an integer and

$$\epsilon = E - \frac{1}{2}k_{\|}^2. \tag{6.4}$$

Within the WKB-approximation the image potential phase shift is give by [15]

$$\phi_b(\epsilon) = \pi \left[\sqrt{\frac{1}{8(E_v - \epsilon)}} - 1\right] \tag{6.5}$$

which diverges at $\epsilon = E_v$, permitting equation (6.3) to be satisfied *ad infinitum* and generating a Rydberg series converging on the effective vacuum level $E_v + 1/2k_{\|}^2$. For the vacuum level lying well inside the gap the barrier phase shift varies much faster than the crystal phase shift within the energy range of the image states. Neglecting the energy variation of ϕ_c altogether, condition (6.3) yields for the binding energy of these states

$$\epsilon_n = E_v - \frac{1}{32(n+a)^2} \tag{6.6}$$

where

$$a = \frac{1}{2}(1 - \frac{\phi}{\pi}) \tag{6.7}$$

is the so-called quantum defect. The ideal Rydberg series of equation (6.2) is then obtained by putting $\phi_c = \pi$. This corresponds to replacing the crystal by an infinite barrier which prevents electrons from penetrating into the solid.

At real surfaces, significant corrections to (6.6) can arise because of deviations of the potential from the Coulombic form near the surface, the fact that the crystal phase shift is energy dependent, and the corrugations in the surface potential. For example in a so-called Shockley-inverted s-p band gap the crystal phase shift varies smoothly from 0 at the bottom of the gap to π at the top of the gap causing the binding energy of the $n = 1$ state at different surfaces to vary approximately between -0.85 and -0.55 eV.

Smith [9] combined the multiple-reflection ideas of Echenique and Pendry with a nearly-free electron (NFE) parameterisation of the sp bulk band edges usually supporting these states to account for the energy and wave-vector dependence of the crystal phase shift. The resulting one-dimensional model and its more elaborate versions [15-17] have been rather successful in describing the systematics of the binding energy and dispersion relation of these states as long as the underlying assumptions (NFE description of the projected bulk band gaps and the continuum of bulk states, negligible potential variation parallel to the surface and small changes of the potential at the surface) are valid. An accurate and unified description of image states at clean and adsorbate-covered surfaces, however, requires going beyond such model calculations. For example, in the case of ferromagnetic surfaces, where the gap is affected by the presence of spin-split d-bands, the discrepancy between experiment and model calculation is at least three times as large as the experimental limits of error [12]. Furthermore, the influence of adsorption, which is found experimentally to change the binding energy and lifetime of the image states quite differently for different adsorbates, is not understood even qualitatively within such models.

Unfortunately, evaluating the image states from first principles is impeded by the fact that the local density approximation, a crucial element for practical surface electronic structure calculations, fails to produce the correct asymptotic image tail of the surface barrier responsible for the existence of these states. Thus image states are in principle beyond the realm of the LDA calculations. By incorporating long-range correlation effects neglected in the LDA, it is possible to produce a self-consistent surface barrier which is image-like in the vacuum [20]. However, such calculations, which are discussed briefly in the next section, consist of several self-consistency cycles and require evaluating the non-local and energy-dependent electron self-energy at the surface. Consequently the computational effort required for obtaining the image potential increases dramatically as one tries to move from the jellium surface to real surfaces. In particular, in the case of noble metal and transition metal surfaces for which the physics of image states becomes really interesting, the evaluation of the image potential from the first-principles is still beyond the current capabilities.

For the above reason, our more pragmatic strategy is to concentrate not on evaluating the image potential itself but rather on calculating *the effect of its presence* on electronic states of real surfaces. For this purpose we partition the space into three regions: the substrate where the LDA works well and for which we can calculate the electronic structure and effective potential accurately using the surface-embedded Green function method of Inglesfield and Benesh [21], the vacuum region where the potential has the image form and finally a transition region in between, extending a few angstroms into the vacuum (the *near-surface region*). The exact form of the potential felt by an electron in the near-surface region is not known and this makes it necessary to introduce an *Ansatz* for the potential in this region. The final step is to solve the resulting Schrödinger equation in the near-surface region, where image states have most weight and in which we are primarily interested. This is done using the embedding method described in part I. The Schrödinger equation is solved explicitly in the near-surface region, and embedding potentials are added on to the Hamiltonian to describe the scattering of the electronic states by the asymptotic Coulomb potential (6.1), and the atoms in the surface and semi-infinite substrate.

We give a description of our near-surface embedding method in chapter 7. A central quantity in studying electronic structure of surfaces is the surface density of states, the charge density of electrons with a particular energy and spatially integrated over the surface region. In chapter 7 we apply our method to investigate how the image potential affects the threshold behaviour of this quantity at the vacuum level. We will show that in addition to giving rise to image states, the long-range character of this potential results in a threshold behaviour of the surface density of states which is *common* to all metallic surfaces and is observable by the technique of inverse photoemission. In chapter 8 we apply the spin-polarised version of our method to examine the possibility of creating a spin-polarised two-dimensional electron gas of image states on the top of a ferromagnetic surface by calculating the magnetic splitting of these states at the Fe(110) surface, a surface with a relatively high magnetic moment and investigating its origin. In chapter 9 we continue our study of spin-polarised image states and resonances at the Fe(110) surface by examining spin-dependent behaviour of image states as they disperse into the spin-polarised band gaps of Fe(110) and their transition into spin-polarised image resonances. In the remaining of this chapter we examine the physics of the potential barrier and the origin of its long-range image tail.

6.1 The physics of the potential barrier at metal surfaces

It is well known from classical electrostatics [22] that an electron outside an ideal metal surface, occupying the half-space $z > 0$, is attracted to its image with a potential function of the form:

$$V(z) = -\frac{1}{4|z|} \tag{6.8}$$

where the factor of 4 comes from 2 (from the distance between the charge and its image) × 2 (because the image charge is induced by the electron itself).

This solution is clearly unsatisfactory near the surface, where $V(z) \to -\infty$. The first quantum mechanical attempt to go beyond this classical picture was by Bardeen [23] who examined the potential barrier for the jellium model of a simple metal. Bardeen performed approximately self-consistent Hartree-Fock calculations, assuming a local density description of the correlation. He found that the electron-surface interaction far outside the surface ($z \to -\infty$) is described by the image form (6.8), but there are large deviations as the electron approaches the surface. In their pioneering work Lang and Kohn [24] performed self-consistent density functional calculations for the same model of the metal-vacuum interface using a local description of the exchange and correlation and determined charge densities and effective potentials for an electron in the surface region. They found that the effective potential obtained from their calculations had an exponential decay as $z \to -\infty$ due to their use of the local density approximation for the exchange and correlation potential. On the other hand, at distances asymptotically far from the surface an electron may be considered as a distinguishable classical particle and its interaction with the surface determined. Thus treating the electron as an external point charge, Lang and Kohn calculated [25] the charge density distribution induced by a this charge within linear response theory, and showed the energy of interaction to have the classical image form

$$V(z) = -\frac{1}{4|z - z_0|} \tag{6.9}$$

with the quantum mechanical modification that the reference plane z_0 is shifted outwards from its classical position $z = 0$ and corresponds to the centre of gravity of the induced charge distribution in the metal. The jellium calculations of Lang and Kohn yields an image plane lying $1-2$ atomic units outside the geometrical surface (half an interlayer spacing beyond the last atomic plane of the metal). Recent calculation by Aers and Inglesfield [26] indicate that the image plane seen by a test charge at a real surface can be significantly closer to the geometrical surface than the jellium results suggested.

The failure of the LDA in giving the correct asymptotic form of the surface barrier can be easily understood since general quantum mechanical arguments show [27] that the electron density far outside a finite system or a surface has an exponential decay. The density functional surface barrier consists of an electrostatic part, which originates from the dipole layer formed at the surface by the spreading out of the electrons past the edge of the background, plus an exchange and correlation part. The exponential decay of the electron density implies a corresponding short-range form of the electrostatic contribution to the barrier outside the surface. Hence the asymptotic form of the potential is determined by the exchange-correlation contribution. Now, within the LDA, the exchange-correlation part of the barrier is a *local* function of the electron density $n(\mathbf{r})$, having an approximately $n^{1/3}(\mathbf{r})$ functional dependence. Therefore, an exponential decay of electron density outside the surface results in a corresponding *exponential* decay of the exchange-correlation contribution to the barrier.

Note, however, that because of the Hohenberg-Kohn theorem the exact exchange-correlation potential entering the Kohn-Sham equations is bound to have the correct asymptotic form in order to exactly reproduce the spatial variations of the ground state density everywhere including the vacuum region. Indeed, Almbladh and von Barth [27] obtained asymptotically exact results for the charge density distribution of the interacting system far outside the metal surface from which they deduced the image-like asymptotic form of the exact exchange-correlation potential:

$$v_{xc}(\mathbf{r}) \approx -1/4|z| \qquad z \to -\infty. \tag{6.10}$$

As discussed in chapter 1 the exact exchange-correlation potential of density functional theory is defined by the equation $v_{xc} = \delta E_{xc}[n]/\delta n(\mathbf{r})$, where $E_{xc}[n]$ is the exchange and correlation energy functional of the interacting electron system. In fact, several functional forms of E_{xc} have been suggested [28, 29] in recent years which enforce the presence of an image tail of v_{xc}. These functionals, however, are usually introduced in a more or less *ad hoc* way.

Strictly speaking the density functional exchange-correlation potential applies only to a Kohn-Sham electron (i.e. an independent "electron" described by an eigenfunction of the Kohn-Sham equations). From a quantum mechanical point of view, however, an electron outside the surface is part of the many-electron system. It is in fact a quasi-particle (a single-particle like approximate eigenstate of the many-electron system which can be probed in spectroscopic measurements) whose motion is described by the Schrödinger-like equation [30]

$$[-\frac{1}{2}\nabla^2 + V_c(\mathbf{r}) - E]\Phi(\mathbf{r}) = \int d\mathbf{r}'\Sigma(\mathbf{r},\mathbf{r}';E)\Phi(\mathbf{r}') \tag{6.11}$$

where $\Sigma(\mathbf{r},\mathbf{r}';E)$ is the complex energy dependent electron self-energy [30] and $V_c(\mathbf{r})$ is the electrostatic potential due to the nuclei plus the average electron density. The real part of

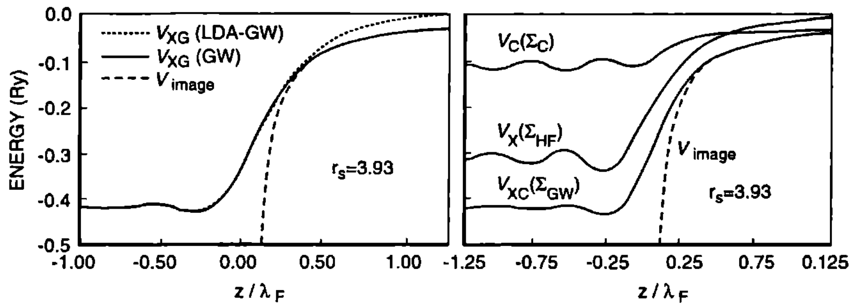

Figure 6.3: (left) $v_{xc}(z)$ at the jellium surface for $r_s = 3.93$ (for which $\lambda_F = 12.9$ a.u.). The solid curve is the density-functional potential obtained from the electron self-energy, and the dotted curve is the corresponding LDA potential. The dashed curve is the image-potential $V_{im} = -e^2/4(z - z_0)$. (right) v_{xc} for three approximations for the self-energy: Σ_{HF} (Hartree-Fock). Σ_c (correlation), and Σ_{GW} (sum of the previous two) [20].

the self-energy acts as a non-local potential while its imaginary part gives the broadening of the quasi-particle states. Thus in order to determine the potential encountered by "real" electrons (i.e. those which can be probed experimentally) far outside the surface one should be determining the asymptotic form of the self-energy.

The state-of-the-art method for calculating the self-energy in solids [31] is the GW approximation due to Hedin [32]:

$$\Sigma(\mathbf{r}, \mathbf{r}'; E) = \frac{i}{2\pi} \int dE' e^{iE'\delta} W(\mathbf{r}, \mathbf{r}'; E) G(\mathbf{r}, \mathbf{r}'; E + E'). \tag{6.12}$$

Here W is the screened Coulomb interaction and G is the quasi-particle Green function corresponding to equation (6.11). Employing this approximation together with the random-phase approximation of W, Eguiluz and co-workers evaluated the electron self-energy of a thick jellium slab simulating the semi-infinite crystal [20]. Their results confirm the classical picture, i.e. as an electron moves away from the surface the real part of the self-energy approaches the $-1/4z$ form (the metal occupies the half-space $z < 0$ in these calculations). More importantly, they used an exact integral equation due to Sham and Schlüter [33] to calculate the exact exchange-correlation potential $v_{xc}(\mathbf{r})$ within GW at the surface and found that this quantity merges with the (shifted) image potential $-1/4(z - z_o)$ a few angstroms outside the surface (figure 6.3). According to these calculations the asymptotic $-1/4z$ behaviour is due to the Coulomb-correlation effects present in the correlation part of the exchange-correlation potential. [1] It is thus the same for a Kohn-Sham electron and a classical test charge. However, the position of the effective image plane z_0 includes a significant contribution from the exchange-only part v_{xc}, which is

---

[1] This conclusion agrees with earlier results of Almbladh and von Barth [27] and Sham [34]; it disagrees with the conclusion of Harbola and Sahni [35], who equated v_{xc} for large z with work performed against the bare-exchange hole.

absent for a classical test charge. Thus the image-plane position characterising the barrier experienced by Kohn-Sham electrons is *not* the same as its counterpart obtained for a test charge. This conclusion is supported by the fact that the image-plane position deduced from measured binding energies of the image states shows a systematic discrepancy with those obtained from the centre of gravity of the induced surface charge (for example the Ag(100) image plane position deduced from inverse-photoemission experiments is 0.18 *a.u.* on the *solid* side of the surface while the theoretical prediction is 0.98 a.u. on the *vacuum* side [26].

References

[1] D. Straub and F.J. Himpsel, Phys. Rev. B **33**, 2256 (1986).

[2] N.V. Smith and C.T. Chen, Surf. Sci. **274**, 133 (1991).

[3] M. Nekovee, S. Crampin and J.E. Inglesfield, Phys. Rev. Lett. **70**, 3099 (1993).

[4] S. Schuppler, N. Fischer, Th. Fauster and W. Steinmann Phys. Rev. B **46**, 13539 (1992).

[5] N. Fischer, S. Schuppler, R. Fischer, Th. Fauster and W. Steinmann, Phys. Rev. B **42**, 9717 (1990).

[6] P.M. Echenique and J.B. Pendry, Prog. Surf. Sci. **32**, 111 (1989).

[7] J. Rundgren and G. Malmström, Phys. Rev. Lett. **38**, 836 (1977).

[8] V. Dose, W. Altmann, A. Goldmann, U. Kolac and J. Rogzik, Phys. Rev. Lett. **21**, 1919 (1984).

[9] N.V. Smith, Rep. Prog. Phys. **51**, 991 (1985).

[10] F. Passek and M. Donath, Phys. Rev. Lett. **69**, 1101 (1992).

[11] F.J. Himpsel and J.E. Ortega, Phys. Rev. B **46**, 9719 (1992).

[12] W. Steinmann and Th. Fauster, in *Laser Spectroscopy and Photochemistry on Metal Surfaces*, edited by Hai-Lung Dai and Wilson Ho (World Scientific, Singapore, 1993).

[13] G. Binning et al, Phys. Rev. Lett. **55**, 991 (1985).

[14] P.M. Echenique and J.B. Pendry, J. Phys. C **11**, 2065 (1978).

[15] E.G. McRae and M.L. Kane, Surf. Sci. **108**, 435 (1981).

[16] N.V. Smith, Phys. Rev. B **32**, 3549 (1985).

[17] M. Radny, Surf. Sci. 231, **43** (1990).

[18] L. Jurczyszyn, Solid State Comm. **68**, 197 (1988).

[19] W.L. Schaich, Phys. Rev. B **45**, 3744 (1992).

[20] A.G. Eguiluz, M. Heinrischmeier, A. Fleszar and W. Hanke, Phys. Rev. Lett. **68**, 1359 (1992).

[21] J.E. Inglesfield, G.A. Benesh, Phys. Rev. B **37**, 6682 (1988).

[22] J.D. Jackson *Classical Electrodynamics* (John Wiley & Sons, New York 1975).

[23] J. Bardeen, Phys. Rev. **49**, 653 (1936); **58**, 727 (1940).

[24] For a review of this work, see N.D. Lang, Solid State Physics **28**, 225 (1973).

[25] N.D. Lang and W. Kohn, Phys. Rev. B **7**, 3541 (1973).

[26] G.C. Aers and J.E. Inglesfield, Surf. Sci. **217**, 367 (1989).

[27] C.O. Almbladh and U. von Barth, Phys. Rev. B **31**, 3231 (1985).

[28] S. Ossicini, C.M. Bertoni and P. Gies, Europhys. Lett. **1**, 661 (1986); O. Gunnarsson and R.O. Jones, Phys. Scr. **21**, 394 (1980).

[29] P.A. Serrena, J.M. Soler and N. Garcia, Phys. Rev. B. **34**, 6767 (1986).

[30] A.L. Fetter and J.D. Walecka, *Quantum Theory of Many-Particle Systems* (McGraw-Hill New York 1971).

[31] R.W. Godby, M. Schlüter and L.J. Sham, Phys. Rev. Lett. **56**, 2415 (1906); Phys. Rev. B **37**, 10159 (1988).

[32] L. Hedin and S. Lundqvist, Solid Stat. Physics **23**, 1 (1971).

[33] L.J. Sham and M. Schlüter, Phys. Rev. Lett. **51**, 1888 (1983).

[34] L.J. Sham, Phys. Rev. B **32**, 3876 (1985).

[35] M.K. Harbola and V. Sahni, Phys. Rev. B **39**, 10437 (1989).

Chapter 7

Threshold behaviour of surface density of states at the vacuum level *

7.1 Introduction

In this chapter we investigate the behaviour of the electronic density of states at metal surfaces, for energies in the vicinity of the vacuum level. These states, normally unoccupied, can be probed using inverse photoemission (IPES) [1], and the main feature studied to date is the infinite series of Rydberg-like states (image states) just below the vacuum level due to the image tail of the surface potential [2, 3]. We present here results calculated for two completely different substrates, Ni and Al, which show that at the vacuum level, the image tail also completely removes any kind of edge singularity, or "onset" behaviour, which might be expected at this threshold. This result is of conceptual importance for interpreting IPES features near the vacuum level: it means that *in principle* the vacuum level can not be detected.

7.2 Near-surface embedding

Our method of calculation is an extension of the surface embedded Green function (SEGF) method of Inglesfield and Benesh [4] for calculating electronic structure of surface layers embedded onto a semi-infinite substrate. In this method the Green function in the surface region is expanded in a set of LAPW's. These are constructed by dividing space into three regions: a muffin-tin (MT) sphere around each atom, an interstitial region between the muffin-tins, and a vacuum region outside the surface layers. The numerical basis in the MT and the vacuum regions are first generated separately and then augmented to the plane waves in the interstitial region by requiring continuity in both the wave function and their derivatives at the boundaries. In addition each basis is linearised in energy, i.e.

---

*Based on Europhys. Lett. 19, 535 (1992) by. M Nekovee and J.E. Inglesfield.

expanded in terms of a basis function at a proper energy-parameter (pivot energy) and its first order derivative in energy. In the vacuum region the basis functions have the form

$$\phi_m(\mathbf{r}) = [Cv_m(z) + F\dot{v}_m(z)]\exp(i\mathbf{K}_m.\mathbf{R}), \tag{7.1}$$

with

$$\mathbf{K}_m = \mathbf{k}_{\|} + \mathbf{G}_m \tag{7.2}$$

and $\mathbf{G}_m$ a surface reciprocal-lattice vector. The function $v_m(z)\exp(i\mathbf{K}_m.\mathbf{R})$ decays exponentially in the vacuum region and satisfies the Schrödinger equation with the planar averaged vacuum potential at a pivot energy E_{vac}:

$$-\frac{1}{2}\frac{d^2v_m(z)}{dz^2} + [V(z) + \frac{1}{2}|\mathbf{K}_m|^2 - E_{\mathrm{vac}}]v_m(z) = 0, \tag{7.3}$$

and $\dot{v}_m$ is its energy derivative. C and F are determined by the condition of continuity in amplitude and derivative across the boundary between the interstitial and the vacuum regions. The above basis functions give a satisfactory description of the tail of *occupied* electronic states of the semi-infinite system outside the surface. However, because of their exponentially decaying form, they are not able to describe the wave functions of image states correctly. These energetic states lie just below the vacuum level and their wavefunctions show strong oscillations in the vacuum region which cannot be reproduced by a set of exponentially decaying basis functions.

In our near-surface embedding method we resolve this problem by treating explicitly the region just above the surface extending a few angstroms into the vacuum – we call this the near surface region (nsr). Both the semi-infinite metal substrate and the vacuum half-space are removed and replaced by embedding potentials [4] acting on the boundaries of the near surface region (figure 7.1). Since, unlike in the original SEGF method, we are effectively dealing with a finite vacuum region, the basis functions need not to satisfy any particular boundary condition in the vacuum region and we can expand the Green function in the embedded region in a set of plane waves of the form

$$\chi_{m,n} = \sqrt{2/AD}\exp(i\mathbf{K}_m.\mathbf{R}) \times \begin{cases} \cos(k_n z) & n \text{ even} \\ \sin(k_n z) & n \text{ odd} \end{cases} \tag{7.4}$$

where $k_n = n\pi/L$, A is the area of surface unit mesh and D the thickness of the near surface region. L is chosen to be somewhat bigger than D. Unlike the exponentially decaying basis functions, the above functions provide an accurate and convenient basis for describing the Green function in the embedded region at arbitrary energies since on the one hand, the variation of the potential in the embedded region parallel to the surface is relatively weak and on the other hand, the use of plane waves to describe the z dependence allows both the bound states and the extended states of the vacuum to be treated on the same footing. In the calculations reported here we found 80-100 plane waves sufficient to guarantee convergence.

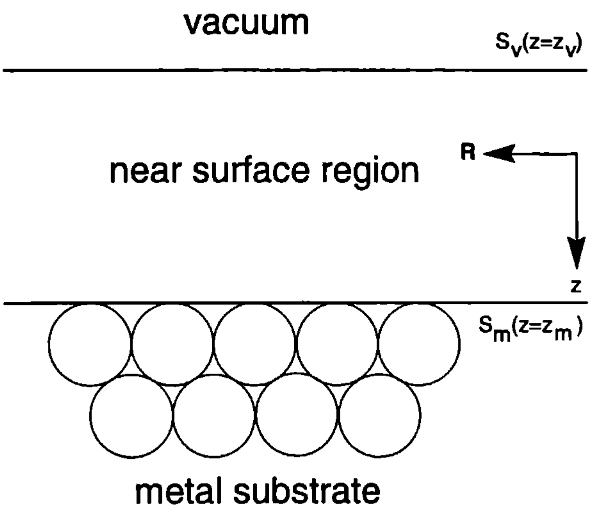

Figure 7.1: Calculation geometry for the near surface region embedded onto metal substrate and vacuum.

The matrix elements of the Green function in the embedded region satisfy the effective Schrödinger equation [4, 5]

$$\sum_{m'n'} [H_{mn,m'n'} + (G_M^{-1})_{mn,m'n'} + (G_V^{-1})_{mn,m'n'} - EO_{mn,m'n'}]G_{mn,m''n''} = \delta_{mn,m''n''} \qquad (7.5)$$

where $H_{mn,m'n'}$ is the matrix element of the Hamiltonian in the embedded region plus additional surface integrals on the boundaries to ensure Hermiticity, $(G_M^{-1})_{mn,m'n'}$ and $(G_V^{-1})_{mn,m'n'}$ are the matrix elements of embedding potentials which replace metal and vacuum half-spaces respectively and $O_{mn,m'n'}$ is the overlap matrix . The metal embedding potential G_M^{-1} acting over S_m describes the influence of the substrate potential exactly. It is the surface-inverse of the substrate Green function with zero normal-derivative on S_m, obtained from a full-potential self-consistent LDA density functional calculation of a single layer of metal embedded onto the bulk (for details of this calculation see [4]).

The potential in the near surface region is taken from the same self-consistent calculation. It is fully three-dimensional with its planar average smoothly varying through this region to join the potential in the vacuum half-space, which is assumed to have the classical image form

$$V_{im}(z) = E_v - \frac{1}{4|z - z_o|} \qquad (7.6)$$

with E_v the self-consistently calculated vacuum level. The position of the effective image plane, z_o, is not fixed a priori but is rather an adjustable parameter of the calculations. The interpolation between the self-consistent LDA potential and the image potential is done by gradually mixing the planar average part of the LDA potential $V_{LDA}(z)$ with the image potential according to the following formula

$$V(z) = [1 - I_x(a,b)]V_{LDA}(z) + I_x(a,b)V_{im}(z). \tag{7.7}$$

with

$$x = -\frac{z - z_m}{z_m - z_v}. \tag{7.8}$$

$I_x(a,b)$ is the incomplete Beta function [6] which rises from zero at z_m to unity at z_v. We found that putting $a = 8$ and $b = 10$ in the above formula results in a smooth variation of the resulting potential (an alternative interpolation scheme often used is the JJJ form [7]).

The vacuum embedding potential G_V^{-1}, which is crucial for a correct description of the energy spectrum near the vacuum level, is found by the matching Green function method [8]. Its matrix element is given by

$$(G_V^{-1})_{mn,m'n'} = \frac{2}{D}\left\{ \begin{array}{c} \cos(k_n z_v) \\ \sin(k_n z_v) \end{array} \right\} \times \left(-\frac{\phi'(z_v;\epsilon_m)}{\phi(z_v;\epsilon_m)}\right) \left\{ \begin{array}{c} \cos(k_{n'} z_v) \\ \sin(k_{n'} z_v) \end{array} \right\} \delta_{m,m'}. \tag{7.9}$$

Here ϕ is the solution of the one-dimensional Schrödinger equation in the vacuum region:

$$[-\frac{1}{2}\frac{d^2}{dz^2} - \frac{1}{4|z - z_o|} - \epsilon_m]\phi(z;\epsilon_m) = 0 \qquad z \leq z_o \tag{7.10}$$

which is irregular at $z = z_o$ and satisfies outgoing wave boundary conditions at $-\infty$. With the help of the definitions

$$\zeta = \sqrt{2\epsilon_m}(z_o - z) \qquad \eta = \frac{1}{4\sqrt{2\epsilon_m}} \tag{7.11}$$

(7.11) reduces to the equation of the s-state Coulomb wavefunctions [9]

$$\frac{d^2\phi(\zeta;\eta)}{d\zeta^2} + (1 - \frac{2\eta}{\zeta})\phi(\zeta;\eta) = 0. \tag{7.12}$$

We calculate ϕ and its derivative numerically using the continued fraction algorithm of Thompson and Barnett [10] for evaluating Coulomb wave functions at complex energies.

7.3 Threshold behaviour and its origin

As the first example we consider the Ni(001) surface for which the vacuum level lies in the middle of the $X_4' - X_1$ gap of the bulk band structure (our self-consistently calculated vacuum level is $E_v = E_F + 5.71$ eV with E_F the Fermi energy). Figure 7.2. shows the calculated density of states

$$\sigma(E) = \frac{1}{\pi}\int_{nsr} d\mathbf{r}\, \mathcal{I}m[G(\mathbf{r},\mathbf{r},E + i\delta)] \tag{7.13}$$

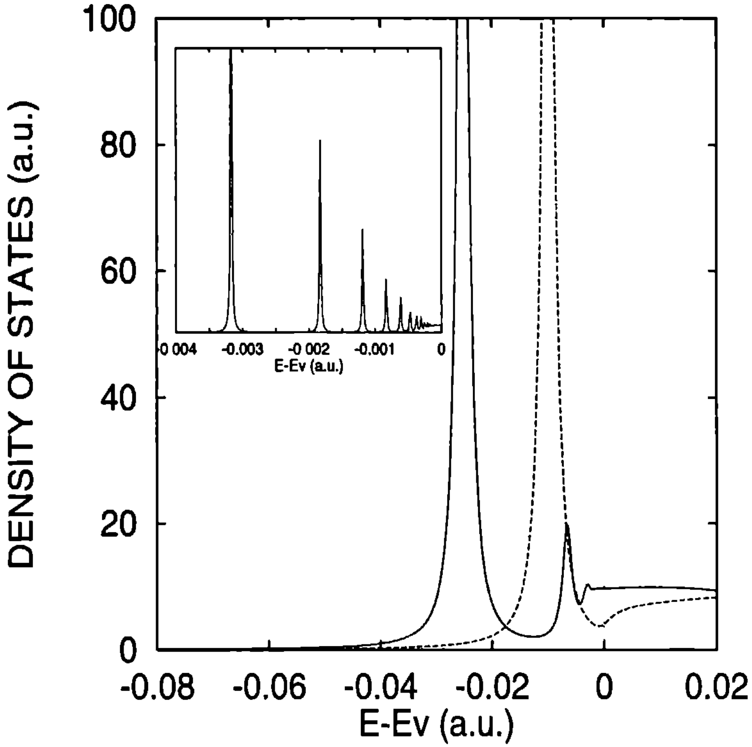

Figure 7.2: Density of states at $k_{||} = (0,0)$ for a 10 a.u. thick near surface region embedded onto the Ni(001) substrate (imaginary part of energy = (0.001 a.u.)) Results are shown for the short-range LDA potential (dashed lines), and the image potential (solid lines). The LDA result shows a singularity at the vacuum edge. This singularity is completely washed out by the long-range image potential which results in a smooth behaviour at the vacuum threshold. The steplike feature just below the threshold is the average of infinitely many image states and can be resolved by working at a much smaller imaginary energy as shown in the inset.

at $\overline{\Gamma}$ for the near surface region of thickness 10 a.u. embedded onto the Ni(001) substrate. The results of two different calculations are shown. The first calculation (dashed lines) is carried out with the exponentially decaying LDA surface potential and the vacuum embedding potential set equal to its free-electron value (i.e. no long-range image tail), while in the second calculation (solid lines) the image potential is included as described above. In these calculations the energy has been shifted off the real axis by 0.001 a.u. so that the discrete surface states are broadened slightly. The effect of the image potential on the density of states below X_4' is marginal, since these states lie too low in energy to feel the asymptotic form of the surface barrier. This situation changes completely within the gap. With the exponentially decaying LDA potential a single surface state is split off from the vacuum continuum. Immediately above the vacuum level, the vacuum continuum has a $(E - E_v)^{1/2}$ singularity, analogous to the singularity in the surface density of states at a bulk band edge [11]. The image potential, however, gives rise to the well-known infinite Rydberg series just below the vacuum level [12]. The $n = 1$ state is well separated from the rest of the series and, broadened by the imaginary part of the energy, shows up as a large Lorentzian, whose position is a function of the image plane z_o. In table 7.3 we list the computed binding energies of the first two image states for different values of this parameter. Clearly, both energy levels move down with the image plane moving outwards. Note, however, that the $n = 1$ state is much more sensitive to the variation of the image plane position. Putting the image plane at $z = 0.4$ a.u. on the vacuum side of the geometrical surface (the jellium edge) yields a binding energy of $E_1 = E_v - 0.6$ eV for this state, in accord with experimental data [13].

	$E - E_v$ (eV)	
$z - z_j$ (a.u.)	$n = 1$	$n = 2$
-1.30	-0.495	-0.147
-0.30	-0.554	-0.160
0.0	-0.576	-0.164
0.40	-0.606	-0.168
1.30	-0.658	-0.180

Table 7.1: Calculated binding energies of the first two image states at the Ni(001) surface for different image-plane positions (z_j is the jellium edge).

It is remarkable how the members of the surface Rydberg series with $n > 3$, which can be resolved by working at a much smaller imaginary energy (see the inset of figure 7.2), give rise to a steplike density of states which starts well below the vacuum level and, in contrast to the LDA results, goes *continuously* through the vacuum threshold to join the adjacent continuum: the vacuum level does not show up! This remarkable effect is a direct consequence of the Coulombic tail of the potential and is well-known in scattering theory [14] and in the context of optical absorption by excitons [15]. But we believe that this is the first time that it has been explored in the present context.

We can understand the above behaviour by assuming that for large values of n the image state wave functions are basically hydrogenic and can be well approximated by

$$\psi_n(Z) = \frac{1}{4\sqrt{An^3}} Z R_{n0}(Z/4) \tag{7.14}$$

with R_{n0} the radial solution of a s state of the hydrogen atom [16] and $Z = -(z - z_o)$.

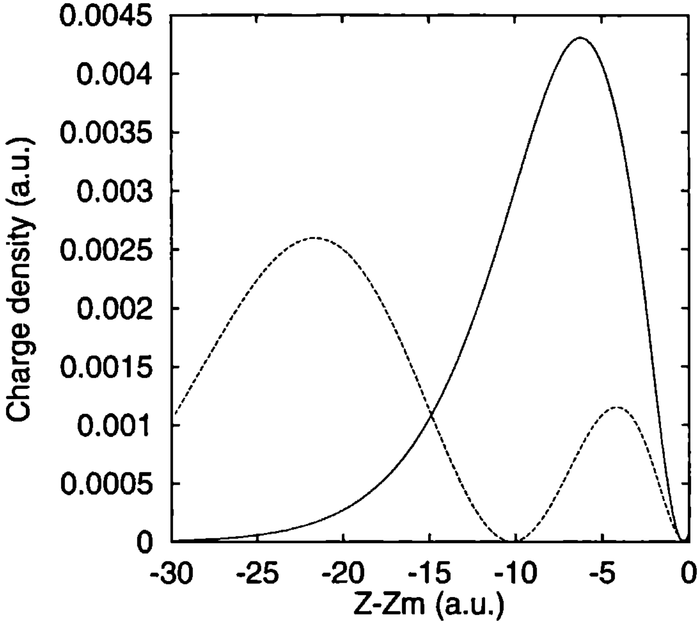

Figure 7.3: Planar averaged charge density of the first (solid line) and the second (dashed line) image states. The jellium edge is at $z = 0.6$ to the right of the metal embedding plane. The charge density is calculated for a 30 a.u. near surface region embedded on the Ni(001) substrate. The charge density in the substrate, not shown, is extremely small.

As can be seen from figure 7.3, in the case of the Ni(001) surface, which is rather closed-packed, this assumption works very well even for the lowest members of the series. For large n values the binding energy of the image states satisfies:

$$E_v - E_n = \epsilon_n = \frac{1}{32n^2}. \tag{7.15}$$

As the vacuum level is approached the infinite number of image states overlap at any finite energy broadening to form a "continuum" just below the vacuum edge. The density of states per unit energy is then given by

$$g(\epsilon) = \frac{1}{4}(2\epsilon)^{-\frac{3}{2}} = 16n^3. \tag{7.16}$$

This gives for the local density of states averaged over a small energy interval:

$$\sigma(Z;\epsilon) = \psi_\epsilon(Z)\psi_\epsilon(Z)g(\epsilon) = \frac{1}{A}\, Z^2 R_{\epsilon 0}(Z/4)R_{\epsilon 0}(Z/4) \tag{7.17}$$

which, in contrast to the total density of states, only weakly depends on energy and is regular at $\epsilon = 0^-$. In the true continuum, $\epsilon > 0$, the energy-normalised wave functions are given by

$$\psi_\epsilon(Z) = \frac{1}{\sqrt{A(1-e^{-\pi/2k})}} Z R_{\epsilon 0}(Z/4) \tag{7.18}$$

with $k = \sqrt{2\epsilon}$, and $R_{\epsilon 0}$ the radial s state eigenfunction of the hydrogen atom corresponding to the positive energy ϵ [16]. The local density of states, the charge density of electrons with energy ϵ is now given by

$$\sigma(Z;\epsilon) = \frac{1}{A(1-e^{-\pi/2k})} Z^2 R_{\epsilon 0}(Z/4) R_{\epsilon 0}(Z/4) \tag{7.19}$$

This joins smoothly to (7.18) as $\epsilon \to 0^+$, since the radial wave function is well-behaved at zero energy and the normalisation prefactor approaches $1/A$ as $k \to 0$.

We now turn to the case of Al which is a typical free-electron like metal with no gap at the vacuum level. In figure 7.4 we show the calculated $\overline{\Gamma}$ density of states for the near-surface region embedded onto the Al(001) substrate. The surface state seen at 0.007 a.u. above the bottom of the bulk band gap is the Shockley state well-known from photoemission [17]. In contrast to this state, the image states are attached to the vacuum level which now falls inside the bulk continuum (the self-consistently calculated vacuum level is $E_v = E_f + 4.63$ eV) . Consequently, they now show up as an infinite series of surface resonances superimposed on the bulk continuum and with an intrinsic width which decreases monotonically as the energy approaches the vacuum level (see inset of figure 7.4). This is behaviour which has also been predicted from one-dimensional model calculations [15-18]. The first image resonance is well separated from the higher members and is narrow enough to be seen experimentally (the experimental observation of this state at the Al(111) surface has been already reported [22]).

The asymmetric shape of this image resonance is due to the fact that it is now superimposed on the bulk continuum. In contrast to the case of Ni(001), the averaged density of states in the vicinity of E_v is not a constant due to this non-zero background. However, it is again perfectly well-behaved with no observable threshold. Once again the LDA density of states exhibits a completely different behaviour near the vacuum level: in contrast to the Ni(001) LDA case, the near surface region density of states varies continuously but it has an infinite slope at the vacuum level.

7.4 Conclusion

We have shown in this chapter that, in the vicinity of the vacuum threshold, the surface density of states is strongly affected by the asymptotic form of the surface potential. The behaviour at the threshold itself is solely determined by the Coulombic tail of the

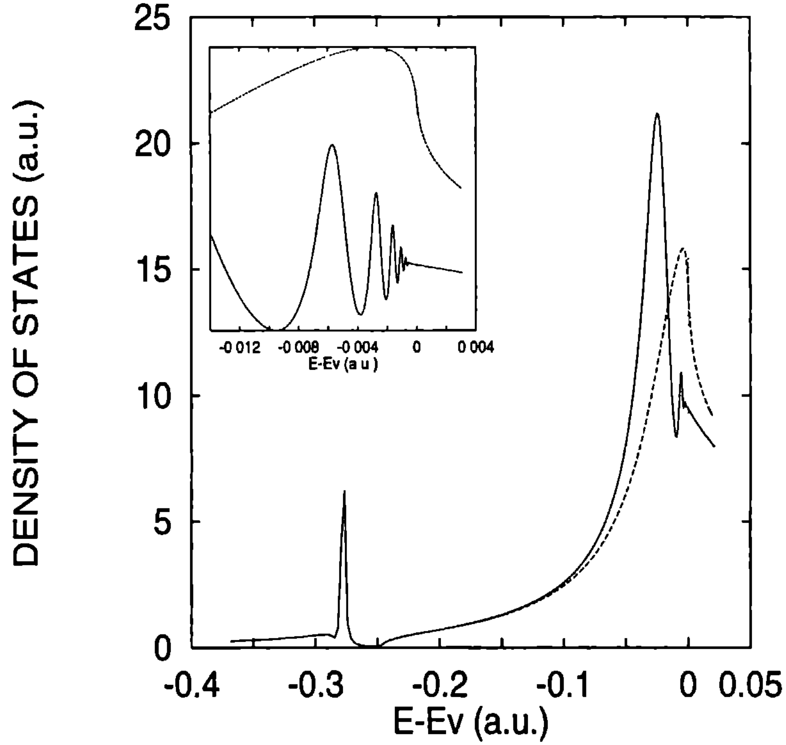

Figure 7.4: Density of states at $k_{||} = (0,0)$ for the near surface region embedded onto Al(001) substrate (imaginary part of energy = (0.001 a.u.)). Note that the LDA density of states (dashed lines) has an infinite slope at the vacuum level, while the image potential (solid lines) result joins smoothly to the continuum. The inset shows the results calculated with an imaginary energy of 0.0001 a.u.

potential. It removes threshold singularities associated with short-range potentials by giving rise to an infinite number of states, or resonances, just below the vacuum level. As the threshold is approached from below, the density of these states will increase infinitely to an accumulation point at the threshold. Nevertheless the density of states averaged over a small energy range, which is the quantity probed by IPES, tends to a finite value and joins smoothly to the limit from the high-energy side.

We remark that the steplike onset found in many IPES spectra of metals [2, 23] which follows the large peak associated with the first image state is always located below the vacuum level for the above reason. The results of our calculations also rule out the possibility of a surface density of states with a steplike onset precisely at the vacuum threshold as suggested in [24].

References

[1] N. V. Smith, Rep. Prog. Phys. **51**, 1227 (1988).

[2] D. Straub and F.J. Himpsel, Phys. Rev. B **33**, 2256 (1986).

[3] N.V. Smith and C.T. Chen, Surf. Sci. **247**, 133 (1991).

[4] J.E. Inglesfield and G.A. Benesh, Phys. Rev. B **37**, 6682 (1988).

[5] S. Crampin, J.B.A.N van Hoof, M. Nekovee and J.E. Inglesfield, J. Phys. Condensed Matter **4**, 1475 (1992).

[6] W.H. Press, B.P. Flannery, S.A. Teukolsky and W.T. Vetterling, *Numerical Recipes* (Cambridge University Press, Cambridge 1989).

[7] R.O. Jones, P.J. Jennings and O. Jepsen, Phys. Rev. B, **26**, 6474 (1984).

[8] J.E. Inglesfield J. Phys. C **4**, L14 (1971).

[9] M. Abramowitz, *Handbook of Mathematical functions* eds. M. Abramowitz and I.A. Stegun (Dover Publications, Inc. New York 1972).

[10] I.J. Thompson and A.R. Barnett, J. Comp. Phys. **64**, 490 (1986).

[11] J.E. Inglesfield, Rep. Prog. Phys. **45**, 224 (1982).

[12] P.M. Echenique and J.B. Pendry, J. Phys. C **11**, 2065 (1978).

[13] P.D. Johnson and N.V. Smith, Phys. Rev. B **27**, 2527 (1983).

[14] L. Fonda and R.G. Newton, Ann. Phys. **9**, 416 (1960).

[15] R.J. Elliott, Phys. Rev. **108**, 1384 (1957).

[16] L.D. Landau and E.M. Lifshitz *Course of Theoretical Physics Vol 3* (Pergamon Press, 1977), p123.

[17] E.W. Plummer, Surf. Sci. **152/153**, 162 (1985).

[18] S.A. Lindgren and L. Walldén, Phys. Rev. B **40**, 11546 (1988).

[19] M. Radny, Surf. Sci. **231**, 43 (1990).

[20] L. Jurczyszyn, private communication.

[21] W.L. Schaich and J.T. Lee, Phys. Rev. B **44**, 5973 (1991)

[22] D. Heskett, K.-H. Frank, K. Horn, E. Koch, H.J. Freund, A. Baddorf, K.D. Tseui and E.W. Plummer, Phys. Rev. B **37**, 10387 (1988).

[23] V. Dose, W. Altmann, A. Goldmann, U. Kolac, and J. Rogzik, Phys. Rev. Lett. **52**, 1919 (1984).

[24] P.A. Bruhwiler, G.M. Watson, E.W. Plummer, H.-J. Sagner and K.-H. Frank, Europhys. Lett. **11**, 573 (1990).

Chapter 8

Magnetic splitting of image states at Fe(110) *

Image-induced surface states which have their origin in the long range image tail of the surface potential have become in recent years a subject of extensive theoretical and experimental studies [1-7]. Up to now most of the work has been concerned with the binding energies, lifetimes and dispersion of these states. An exciting new topic concerns the interaction of image states with the surface of a ferromagnet which splits the spin degeneracy of these states [8,9,10]. Very recently, through the technique of spin-polarized inverse photoemission it has become possible to measure this splitting and the first direct measurements made on the Ni(111) surface give a splitting of 18 meV for the $n = 1$ state [11] while indirect measurements, using two-photon photoemission, had indicated larger splittings on Fe(110) and Co(111) surfaces [12]. A splitting of majority and minority spin image states larger than their lifetime broadening opens up the possibility of selectively populating the majority n=1 image states hence creating an ideal spin-polarised two-dimensional electron gas at the top of a ferromagnetic substrate. In addition, since image states are common to a large number of metal surfaces their magnetic splitting may serve as a probe of magnetic properties at and in the vicinity of magnetic surfaces.

In this chapter we concentrate on Fe(110) which has a relatively high bulk magnetic moment (2.2 μ_B as compared to 0.6 μ_B for Ni). We report here our calculated spin splitting of image states at this surface and investigate its origin. The spin splitting is the net result of two effects. Firstly, since the metal is ferromagnetic, spin up and spin down image states are scattered from different substrate potentials. From first order perturbation theory, the resulting splitting is proportional to the overlap of image state wave functions with the spin polarisation of the substrate effective potential $v^{\uparrow} - v^{\downarrow}$ where $v^{\uparrow}$ and $v^{\downarrow}$ are the potentials for spin up and spin down electrons respectively. On the other hand, in a multiple scattering picture this part of the splitting can be viewed as a bulk band structure effect caused by a difference in the position of spin up and spin down bulk band edges [8, 13]. Secondly, due to the exchange interaction near the crystal surface, the effective surface barrier experienced by electrons outside the metal is also spin-dependent.

---

*Based on Phys. Rev. Lett. 70, 3099 (1993) by: M. Nekovee, S. Crampin and J.E. Inglesfield.

We take both effects fully into account in our calculations and find that the spin splitting of image states is primarily due to the former effect, i.e. it is a consequence of exchange-processes in the substrate. More interestingly, we find that the relatively small contribution of the surface barrier to the splitting has a sign *opposite* to the substrate contribution. Thus, in contrast to the common picture [8, 9], the polarisation of the surface barrier actually reduces the spin splitting of image states instead of enhancing it. It will be shown that this surprising result is a consequence of a sign reversal in the surface layer magnetisation $m(\mathbf{r}) = n^{\uparrow}(\mathbf{r}) - n^{\downarrow}(\mathbf{r})$ (with $n^{\uparrow\downarrow}(\mathbf{r})$ the spin up (down) charge density) at the Fermi energy which result in a self-consistent way in a sign reversal in the planar average of the surface potential difference $v^{\uparrow}(\mathbf{r}) - v^{\downarrow}(\mathbf{r})$ experienced by image states outside the surface.

The calculations are performed using the spin-polarised version of our previously reported near-surface embedding method [14] for calculating image states at realistic metal surfaces. In this method the one-electron Schrödinger equation in a finite region just above the surface – the near surface region – is solved explicitly (see figure 7.1). The scattering of image states from the semi-infinite ferromagnetic substrate is reproduced by a spin-dependent surface embedding potential acting over S_m, while the long range image tail of the surface potential which is crucial for a correct description of image states is replaced by the Coulomb embedding potential acting over S_v. Both the spin-dependent substrate embedding potential and the spin-dependent surface barrier are the inputs of our calculations. These are obtained from a self-consistent spin-polarised full-potential surface embedded Green function (SEGF) calculation [15, 16] (using the von Barth-Hedin local spin density approximation [17]) of a single layer of Fe(110) embedded onto the ferromagnetic bulk. From this calculations we find a magnetic moment of 2.75 μ_B per surface atom (r_{MT} = 2.35 a.u.) in good agreement with 2.65 μ_B obtained from FLAPW slab calculations [18]. The calculated work functions is 5.30 eV, in good agreement with the experimental value of 5.1 eV [19]. The spin up and spin down potentials in the near surface region are fully three dimensional with their planar averages smoothly varied through this region to join with continuous derivative to their *common* asymptotic image tail given by

$$v(z) = E_v - \frac{1}{4|z - z_o|} \tag{8.1}$$

with E_v the self-consistently calculated vacuum level. The position of the effective image plane, z_o, which is in principle an adjustable parameter, is fixed in the present calculations at half an interlayer spacing beyond the outermost atomic layer (the jellium edge). Solving the Schrödinger equation in the near surface region, we find the one-particle Green function from which the density of states is calculated.

In figure 8.1(a) we display the calculated Fe(110) density of states at $\overline{\Gamma}$ for both spin directions, for energies inside the bulk band gaps. The image tail of the surface potential does not affect the density of states at lower energies. Inside the gap, however, it gives rise to the infinite series of magnetically split image states. The spin up states, corresponding to the majority states in the bulk, have slightly lower binding energies and the splitting is strongest for the $n = 1$ state. We find a splitting of 55 meV for this state (the binding energy of the $n = 1$ spin up state with respect to the vacuum level is -0.71 eV), three times larger than the splitting found experimentally for Ni(111) [11] and consistent with the upper limit of 80 meV deduced from high-resolution two-photon photoemission measurements [12]. Very recent measurements by Passek and Donath [20] have given a splitting of 57 meV, confirming our results with remarkable accuracy. The splitting, however, is less than the measured lifetime broadening of the image states [20] (70 meV for the $n = 1$ majority states, 140 meV for the minority state), suggesting that the use of image states in creating a spin-polarised two-dimensional electron gas might not be feasible (at least on clean Fe(110)).

As can be seen from figure 8.2, the binding energies of image states for both spin directions follow closely the Rydberg-like series:

$$E_n^{\uparrow\downarrow} = E_v - \frac{1}{32(n + a^{\uparrow\downarrow})^2} \tag{8.2}$$

with $a^{\uparrow} = 0.15$, $a^{\downarrow} = 0.22$ the spin-dependent quantum defects. Consequently, the spin splitting $\Delta E_n = E_n^{\downarrow} - E_n^{\uparrow}$ decreases monotonically with n, following an asymptotic $1/n^3$ scaling law:

$$\Delta E_n = \frac{a^{\downarrow} - a^{\uparrow}}{16n^3} \qquad n \text{ large.} \tag{8.3}$$

As described above, the spin splitting may be considered as the net result of a substrate and a surface contribution. To separate these two contributions from each other, we performed a second calculation with the spin-dependent substrate embedding potential replaced with a spin-independent embedding potential corresponding to an infinite barrier. In this way the substrate magnetism is switched off and the only contribution to the exchange splitting comes from the spin-dependence of the surface barrier. The result of this calculations is shown in figure 8.1(b). For comparison, we display in figure 8.1(c) the result of a third calculation performed with a spin-independent surface barrier (obtained by taking the average of spin up and spin down barriers). It is clearly seen that the splitting caused by the spin-dependence of the surface barrier alone is much smaller than the splitting due to the spin-dependent substrate potential, indicating that the exchange splitting of image states is primarily a substrate effect. We note that for this reason, calculations reported in [8] which assume a spin-independent surface barrier but take into account the spin-dependence of the bulk band edges yield a spin splitting of the same order as that reported here. The surprising result is that the two contributions have opposite sign (63 vs -14 meV for the $n = 1$ state). We are thus dealing with two competing effects: the spin polarisation of the substrate potential alone leads to a positive splitting ($E_n^{\downarrow} - E_n^{\uparrow} > 0$) while the spin polarisation of the surface barrier results in a negative splitting, the net result being positive since the substrate effect dominates.

To understand the physical origin of this result, we display in figure 8.3 the planar averages of the self-consistently calculated majority (spin up) and minority (spin down) charge densities and the surface barrier used in the calculations in the near surface region where z is measured from the substrate boundary z_m (which lies 2.35 a.u. outside the

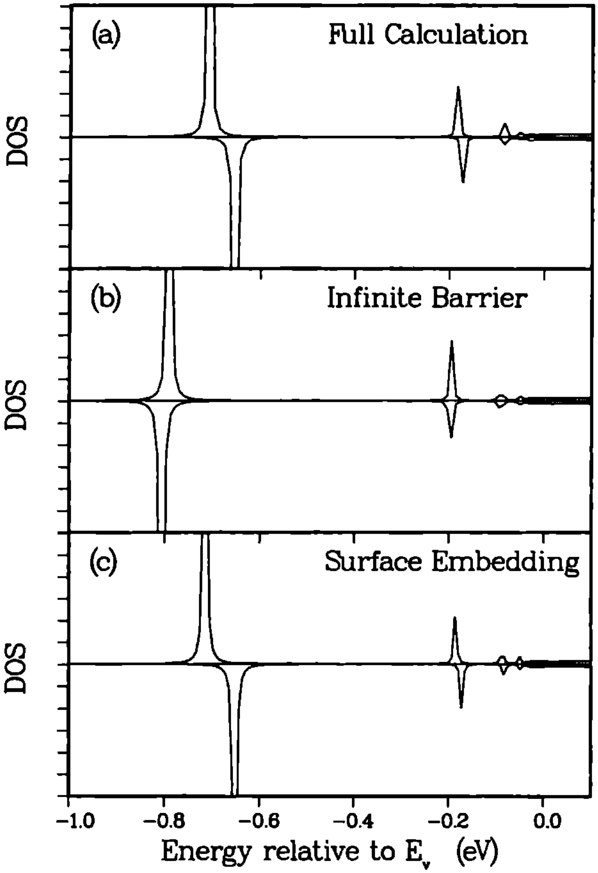

Figure 8.1: Fe(110) Spin-dependent density of states at $\overline{\Gamma}$ integrated through the near surface region (imaginary part of energy = 0.0001 a.u.). The magnetic splitting found from the full calculations (a). The splitting caused by the spin-dependent surface barrier alone (b) and by the spin-polariztion of the substrate potential alone (c). Note how the splitting changes sign and becomes negative as the substrate magnetism is switched off.

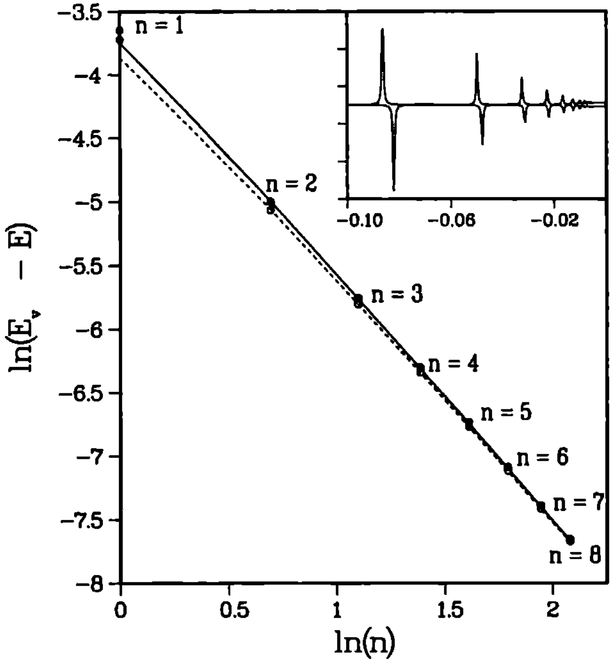

Figure 8.2: ln(E_n) vs ln(n) for spin up (filled circles) and spin down (open circles) image states at Fe(110) surface. The functions $-\ln(32(n + a^{\uparrow\downarrow})^2)$ with $a^\uparrow = 0.15$ (solid line) $a^\downarrow = 0.22$ (dashed line) are displayed for comparison. The inset shows the monotonic decrease of the spin splitting for $n > 2$ members of image series on Fe(110). These are resolved by working at very small imaginary part of energy.

outermost atomic layer (see figure 7.1)). As can be seen from figure 8.3(a), large positive magnetisation is found right at the surface but as we move away from the surface the exponential tail of the minority spin down charge density becomes dominant resulting in a negative spin density in the vacuum region. This behaviour is directly followed by the local exchange-correlation potential and the interpolated barrier used in the calculations (figure 8.3(b)): right at the surface, the spin up electrons experience a deeper potential but at about 1.5 a.u. away from the surface the potential for spin down states becomes more attractive. Image states have their maximum probability $|\psi_n|^2$ well outside the surface (see inset of figure 8.3 (b)). Therefore, when the substrate magnetism is switched off, the spin up image states experience on average a less attractive potential hence their binding energy goes up while the binding energy of the spin down states goes down. The net effect is then a negative splitting as found in the calculations.

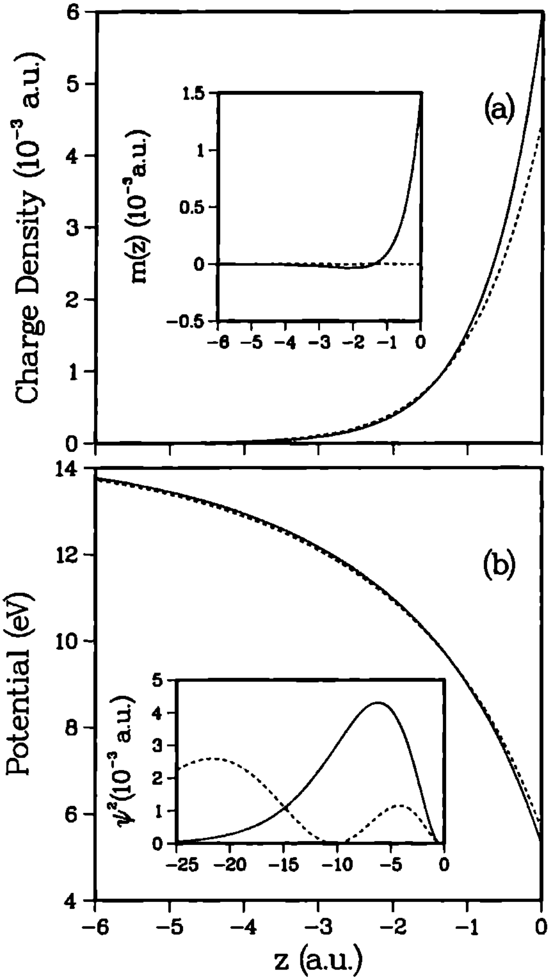

Figure 8.3: Planar averaged electron density (a), and the interpolated surface potential (b) for spin up (solid line) and spin down (dashed line) electrons in the near surface region. The insets show the magnetization (a) and the probability densities of the first (solid line) and the second (dashed line) image state (b).

The sign reversal in the local spin density outside the Fe(110) surface found in our one-layer embedding calculations, which gives rise to the above effect, may also be seen in the work of Wu and Freeman [21]. It can be understand in terms of the band-narrowing effect caused by a lower coordination number at the surface. Due to the narrowing of the DOS at the surface layer, in contrast to the bulk, the minority spin down states overwhelm the majority states around the Fermi energy [21]). Since the charge density leaking into the vacuum originates almost entirely from the states near the Fermi energy, the exponential tail of the minority charge density becomes dominant as we move away into the vacuum, resulting in a negative spin density outside the surface. While the effect of this sign reversal on the spin splitting of image states is masked by the much larger substrate contribution and thus cannot be measured explicitly, it should be possible to measure the sign reversal in the spin density itself directly from the spin- STM image of the Fe(110) surface (as a negative difference between tunnelling currents for majority and minority spins $I^\uparrow - I^\downarrow$).

References

[1] P.M. Echenique and J.B. Pendry, J. Phys. C **11**, 2065 (1978); P.M. Echenique and J.B. Pendry, Prog. Surf. Sci. **32**, 111 (1989) and references therein.

[2] L. Jurczyszyn Solid State Comm. **68**, 197 (1988).

[3] W.L. Schaich and J.T. Lee, Phys. Rev. B **44**, 5973 (1991).

[4] V. Dose, W. Altmann, A. Goldmann, U. Kolac, and J. Rogzik, Phys. Rev. Lett. **52**, 1919 (1984).

[5] D. Straub and F.J. Himpsel, Phys. Rev. B **33**, 2256 (1986).

[6] K. Giesen, F. Hage, F.J. Himpsel, J.J. Reiss, W. Steinmann, Phys. Rev. Lett. **55**, 300 (1985).

[7] N.V. Smith and C.T. Chen, Surf. Sci. **247**, 133 (1991).

[8] G. Borstel and G. Thörner, Surf. Sci. Rep. **8**, 1 (1988).

[9] R. Schneider, K. Strake, K. Ertl, M. Donath, V. Dose, J. Braun, M. Grass and G. Borstel, J. Phys. Condens. Matter **4**, 4293 (1992).

[10] F.J. Himpsel, Phys. Rev. B **43**, 13394 (1991).

[11] F. Passek and M. Donath, Phys. Rev. Lett. **69**, 1101 (1992).

[12] R. Fischer, N. Fischer, S. Schuppler, Th. Fauster and F.J. Himpsel, Phys. Rev. B **46**, 9691 (1992).

[13] Since the overlap of image states with the substrate potential is limited to the outer layers, the simple multiple-scattering picture of spin splitting based on spin-dependent bulk band edges is only valid if the magnetic properties of these layers are not very different from the bulk.

[14] M. Nekovee and J.E. Inglesfield, Europhys. Lett., **19**, 535 (1992).

[15] J.E. Inglesfield and G.A. Benesh, Phys Rev. B **37**, 6682 (1988).

[16] S. Crampin, J.B.A.N. van Hoof, M. Nekovee and J.E. Inglesfield, J. Phys. Condens. Matter **4**, 1475 (1992).

[17] U. von Barth and L. Hedin, J. Phys. C **5**, 1629 (1972).

[18] C. L. Fu and A.J. Freeman, J. Magn. Magn. Mater. **69**, L1 (1987).

[19] H. Scheidt, M. Glöbl, V. Dose and J. Kirschner, Phys. Rev. Lett. **51**, 1688 (1983).

[20] N. Fischer, S. Schuppler, Th. Fauster and W. Steinmann, Phys. Rev. B **42**, 9717 (1990).

[20] F. Passek, M. Donath, K. Ertl, and V. Dose (to be published).

[21] R. Wu and A.J. Freeman, Phys. Rev. Lett. **69**, 2867 (1992).

Chapter 9

Image-induced surface states and resonances at Fe(110) *

9.1 Introduction

Experimentally it is known that even on metal surfaces without an energy gap around the vacuum level, image-induced states persist as surface *resonances* [1, 2] — states which can leak into the substrate, but with enhanced weight in the surface region. In this chapter we shall study the dispersion of the surface states on Fe(110) with wavevector parallel to the surface, and we shall examine in detail their transition to image resonances as they enter the bulk continuum. The case of Fe(110) is particularly interesting, because the spin-up and spin-down image states show quite different behaviour in the vicinity of their respective spin-polarised continua.

The calculations are carried out with our near-surface embedding method outlined in chapters 7 using the same calculational parameters as in chapter 8.

9.2 Surface state dispersion

We have calculated the binding energies of image states for both spin directions along the $\bar{\Gamma}\bar{H}$ high symmetry line of the surface Brillouin zone (see figure 9.1). The results are shown in figure 9.2 together with the projected spin-polarised bulk bands. Only the projection of bulk bands with even symmetry is shown, as only these can interact with the image states. We shall concentrate mainly on the $n = 1$ states which are well-separated from the rest of the series; the results for higher n are similar to $n = 1$ though in general less significant.

As can be seen from figure 9.2 the spin-down (minority) bulk bands are shifted up in energy with respect to the majority spin bands. As the image states are pinned to the same reference energy (the vacuum level), spin-down image states reside in the lower part of the corresponding gap at $k_{\|} = 0$, while the spin-up states lie in the upper part of

---

*Based on Surface Review and Letters 1, 415 (1994) by: M. Nekovee and J.E. Inglesfield.

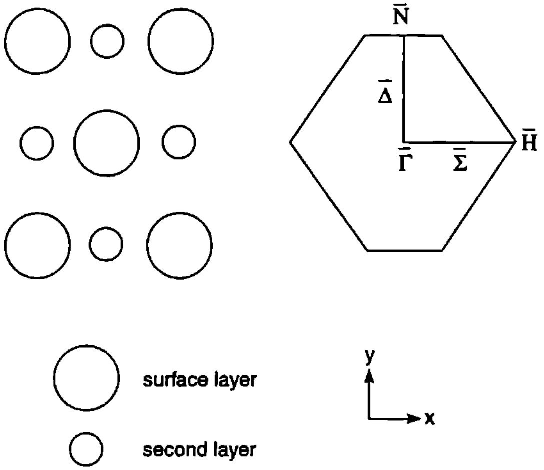

Figure 9.1: The real space structure of the Fe(110) surface and the associated Brillouin zone. The z direction is the surface normal.

the gap. With increasing $k_{\|}$, the effective vacuum level $E_v(k_{\|}) = E_v(0) + k_{\|}^2/2$ disperses upwards, thereby forcing the binding energies of the image states to shift up in the gap. It had been suggested [3] that a $k_{\|}$-dependent spin-splitting might then result. In fact we find that for the range $k_{\|} < 0.8$ Å^{-1} both spin directions show a free-electron dispersion relation (solid lines in figure 9.2):

$$E^{\uparrow\downarrow}(k_{\|}) = E^{\uparrow\downarrow}(0) + \frac{1}{2m^*}k_{\|}^2 \tag{9.1}$$

with effective mass $m^* = 1.0$, and therefore the magnetic splitting remains practically constant.

Things become more interesting at larger $k_{\|}$ as the image states approach the band edges and become nearly degenerate with the bulk continua. By second order perturbation theory this results in a repulsion of the image states by the bulk band edges. As can be seen from figure 9.2, the spin-up state approaches the bulk continuum from below and therefore level repulsion results in a downwards shift in its energy. The nett effect is then a flattening of this image band ($m^* > 1$) just before it is forced to enter the continuum. On the other hand, the spin-down image state approaches the lower band edge and is repelled upwards by the lower lying continuum. In this case the level repulsion is strong enough to keep the state from entering the continuum. Instead it traces the lower band edge all the way up to the point at which the gap closes, showing an effective mass $m^* < 1$.

The above results are consistent with experimental findings for other surfaces [4] which indicate that deviations from the free electron mass $m^* = 1$ occur mainly near the band edges. More importantly, increased effective masses are always found experimentally in

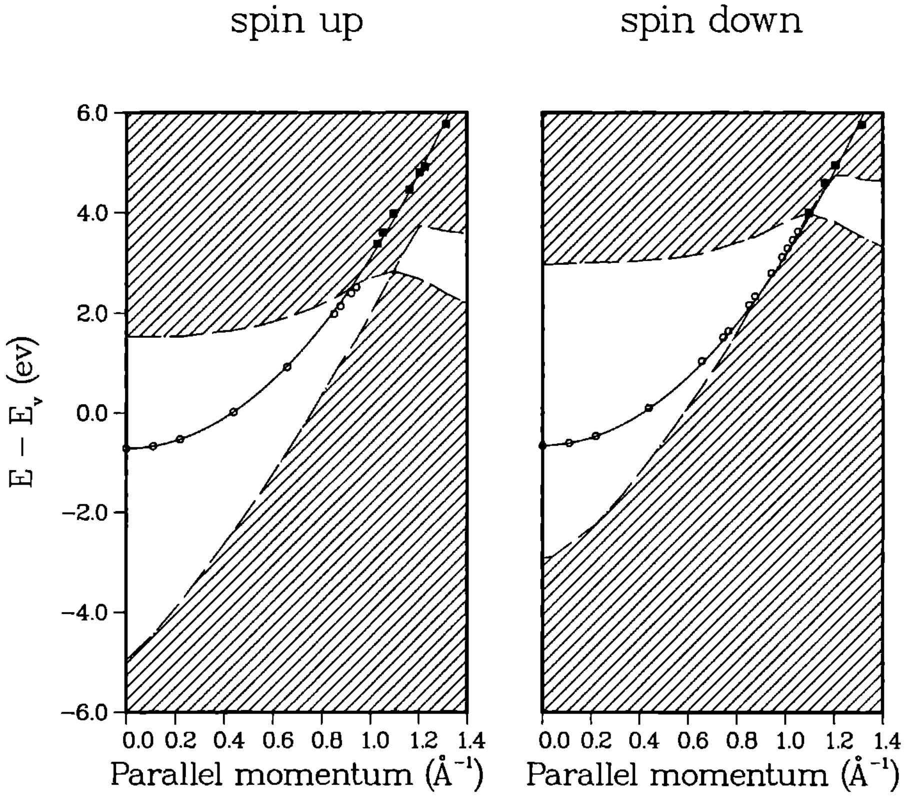

Figure 9.2: Calculated spin-split dispersion relation of image states on Fe(110) along $\bar{\Gamma}\bar{H}$. Open circles: image states; filled squares: image resonances. The shaded regions are the bulk continua (with even symmetry). Solid lines are the extrapolation of the free-electron parabola to $k_{||} > 0$.

cases in which the state lies near the upper band edge, while a decrease in effective mass has been observed when the surface state resides near the lower edge [4].

We note that the higher members of both series are more tightly bound to the vacuum level and in both cases enter the continuum much earlier than the $n = 1$ states.

9.3 Image state-image resonance transition

The transition from image states to image resonances occurs as the effective vacuum level disperses with increasing $k_{||}$ through the gap, forcing the states to follow it into the

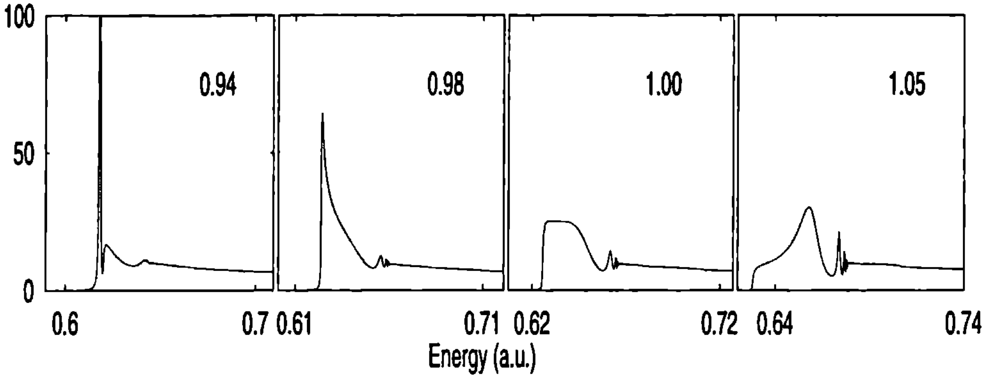

Figure 9.3: Density of states for spin-up electrons for successive $k_{||}$ in the range $0.94 \leq k_{||} \leq 1.05$ $\AA^{-1}$, illustrating transition from image states to image resonances.

continua. Due to the spin-dependence of the band gap, the behaviour is quite different for the two spin directions.

In figure 9.3 the $k_{||}$-resolved density of states is shown for the spin-up direction for successive values of $k_{||} \geq 0.94$ $\AA^{-1}$. Concentrating on the $n = 1$ state, we see that the weight of this state is transferred to the band edge as it enters the bulk continuum, a general phenomenon also seen in other surface state and impurity systems [5, 6]. It is surprising, however, that a further increase in $k_{||}$ does not immediately result in the appearance of the image resonance inside the continuum. In fact there is a small range of $k_{||}$ for which the $n = 1$ state is completely washed out (figure 9.2). With a further increase of $k_{||}$ beyond this range, the image state re-emerges as a resonance, taking back the weight from the edge and sharpening up eventually into a well-defined feature. This behaviour of the surface state re-emerging as a resonance is not seen for a Tamm state, for example, pulled off the band edge by a shift in the surface potential - a Tamm state simply disappears into the continuum, and the only way that a resonance can occur is when it overlaps with a *second* band [5]. The behaviour here is more analogous to the broadening of adsorbate energy levels by overlap with the continuum [7].

We can understand the change in width of the spin-up image resonances in terms of a corresponding change in the strength of coupling to the substrate. Within our approach, the coupling is provided by the substrate embedding potential which enters the Schrödinger equation as a complex energy-dependent potential acting on the substrate boundary of the near-surface region. The embedding potential is in fact a self-energy term, and provided that the real part is small, its imaginary part determines the broadening of the image states.

Figure 9.4 shows the image resonances for successive values of $k_{||}$ together with the imaginary part of the embedding potential (the $\mathbf{K}_m = 0$ component) at the energy of the $n = 1$ resonance. We can clearly see that the decrease in width of this image resonance is directly correlated to the corresponding decrease in the imaginary part of the embed-

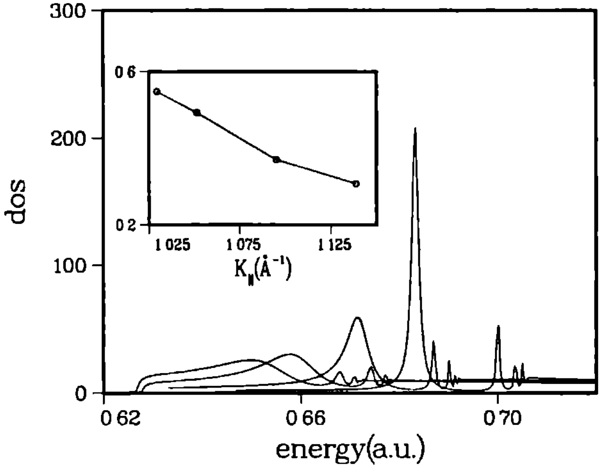

Figure 9.4: Spin-up density of states in the range $1.02 < k_{\parallel} < 1.13$ Å^{-1}, showing the evolution of the $n = 1$ resonance inside the continuum. The inset shows the imaginary part of the corresponding substrate embedding potential (in absolute value) at the energy of the resonance. This quantity decreases monotonically with $k_{\parallel}$ resulting in a corresponding decrease in the width of the resonance.

ding potential. Inside the gap the imaginary part of the embedding potential identically vanishes, resulting in infinitely sharp states - apart from many-body lifetime broadening effects which we do not include.

We now turn to the results for the spin-down states. As can be seen from figure 9.5, for states with $n > 1$, the surface resonance behaviour is very similar to the case of spin-up states. The $n = 1$ spin-down state shows, however, quite a different and complicated behaviour. Pushed up by the lower band edge this state enters the continuum exactly at the point at which the band edges come together (figure 9.2). The value of $k_{\parallel} = 1.09$ Å^{-1} at which this occurs corresponds to the high symmetry point P in the bulk bcc Brillouin zone. The spin-down density of states at this point consists of an extremely narrow peak coming from the $n = 1$ state superimposed on an apparently *continuous* background, to which most of the weight in the image state has been transferred. The position of the sharp peak, trapped as it is between the merged bands, is insensitive to the vacuum level, whereas the centre of gravity of the background feature varies. We find that when the Coulomb tail of the surface potential is switched off, the density of states at this point completely changes, with no narrow peak, and a discontinuity at the energy where the

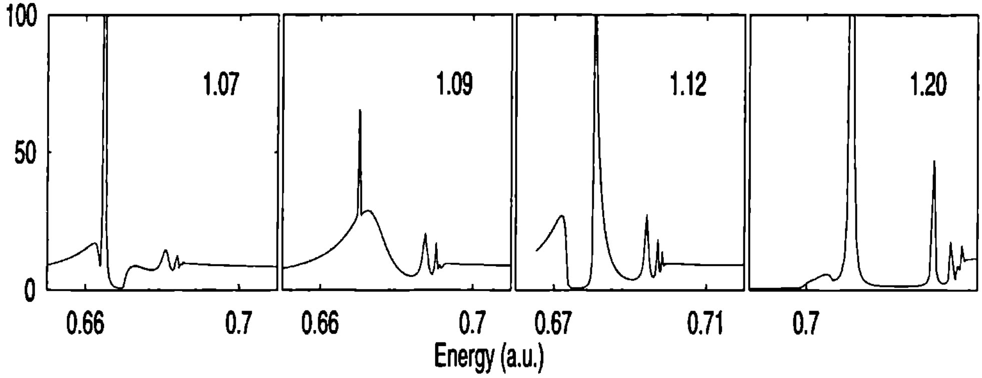

Figure 9.5: The same as figure 9.3 but for the spin-down state in the range $1.07 \leq k_{||} \leq 1.20\ \mathring{A}^{-1}$.

bands come together. It is clear that this is yet another example of how the long-range tail of the surface potential can dramatically change the non-analytic features in the surface density of states [8].

Moving to larger $k_{||}$ the continuum edges repel each other and the gap opens up again. The image state is now captured by the upper band edge which is thereby greatly enhanced. At still larger $k_{||}$ values, where the edge starts to disperse downwards (figure 9.2), the image state separates from the band edge and reappears as a sharp resonance.

The case of spin-up states provides a clear-cut example of the image state-image resonance transition which should be possible to study experimentally, tracing the evolution of the $n = 1$ resonance peak inside the continuum. As we have just seen, the spin-down behaviour is much more complicated. Some of the remarkable spin-down behaviour is accidental - the fact that the $n = 1$ state precisely tracks the lower band edge up to $k_{||} = 1.09\ \mathring{A}^{-1}$ can be altered by changing the vacuum level. However it is clear that the spin-up and spin-down states show quite different behaviour as a function of $k_{||}$, and this should show up in spectroscopic measurements.

9.4 Comparison with experiments

Our calculated spin splitting of image states is consistent with the upper limit of 80 meV obtained from two-photon photoemission experiments [9]. More interestingly, Passek *et al.*[10] reported very recently the first direct measurement of the splitting of the $n = 1$ state at Fe(110) using spin-polarised inverse photoemission. Their measured splitting of 57 ± 5 meV for the $n = 1$ state is in excellent agreement with our predicted value of 55 meV. The measurements by Passek [11] give an effective mass of 1.06 ± 0.01 along the $\bar{\Gamma} - \bar{N}$ direction of the surface Brillouin zone and independent of the spin direction. This result is consistent with our calculated effective mass of 1.0 along the $\Gamma - \bar{H}$ direction. The results for effective masses are not really surprising, since in both directions the vacuum level resides in the middle of the corresponding gaps implying a weak interaction of image states with the bulk band edges for a wide range of $k_{||}$.

We also note that very recent spin-polarised inverse photoemission experiments [12] on Co(10$\bar{1}$0) yield a splitting of 125 meV of the $n = 1$ state at $\bar{Y}$, at the surface zone boundary. The relatively larger splitting found at this surface might be due to the enhancement of the splitting by the spin-dependent surface corrugations on this more open surface, which are strongly felt by the states at the surface zone boundary.

References

[1] D. Heskett, K.-H. Frank, K. Horn, E. Koch, H.J. Freund, A. Baddorf, K.D. Tseui and E.W. Plummer, Phys. Rev. B **37**, 10387 (1988).

[2] S. Yang, R.A. Bartynski, G.P. Kochanski, S. Papadia , T. Fonden and M. Persson, Phys. Rev. Lett. **70**, 849 (1993).

[3] G. Borstel and G. Thörner Surf. Sci. Rep. **8**, 1 (1988).

[4] For a review see, W. Steinmann and Th. Fauster, in *Laser Spectroscopy and Photochemistry on Metal Surfaces*, ed. Hai-Lung Dai and Wilson Ho (World Scientific, Singapore, 1993); P.M. Echenique and J.B. Pendry, Prog. Surf. Sci. **32**, 111 (1989).

[5] J.B.A.N. van Hoof, S. Crampin and J.E. Inglesfield, J. Phys. C **4**, 8477 (1992).

[6] E.N. Economou *Green's Functions in Quantum Physics* (Springer-Verlag, Berlin, 1979), p105.

[7] A. Zangwell, *Physics at Surfaces* (Cambridge University Press, Cambridge, 1988), p214.

[8] M. Nekovee and J.E. Inglesfield, Europhys. Lett., **19**, 535 (1992).

[9] R. Fischer, N. Fischer, S. Schuppler, Th. Fauster and F.J. Himpsel, Phys. Rev. B **46**, 9691 (1992).

[10] F. Passek, M. Donath, K. Ertl and V. Dose, to be published.

[11] F. Passek, Thesis, University of Bayreuth 1994 (unpublished).

[12] S. Bode, K. Starke, P. Rech and G. Kaindl, Phys. Rev. Lett., **72**, 1072 (1994).

Part III

Dielectric response of simple metal surfaces

Chapter 10

Dielectric response of simple metal surfaces

In this chapter the problem which we consider is how to calculate the dielectric response of a metal surface to a weak external electromagnetic field. This problem is one of the basic topics in surface physics and is of interest because it covers important subjects such as surface elementary excitations and the screening of electromagnetic fields, whose knowledge is indispensable for a detailed understanding of the outcome of various surface spectroscopies such as photoemission and electron energy loss spectroscopy (EELS).

Dielectric response is only significant when the electrons of a medium can follow the variation of the externally imposed perturbation. This is reflected in the fact that the dielectric constant approaches 1 for frequencies much larger than the plasma frequency ω_p. In the case of external electromagnetic fields the restriction to low frequencies has an important consequence, namely that one is always in the long-wavelength regime, i.e. $|\mathbf{q}| \ll k_F$, with k_F the Fermi wavevector and $\mathbf{q}$ the wavevector of the incident field. In addition, using the usual "pillbox" arguments of classical electrodynamics applied to Maxwell's equations at the surface, it can be shown [1] that surface charge is only induced when the electric field has a component along the surface normal. This means that surface dielectric behaviour is important when one is dealing with either longitudinal electric fields, originating from charged or polarisable particles in the vicinity of the surface, or with p-polarised electromagnetic fields impinging on the surface.

In the long-wavelength regime and for external fields oriented perpendicular to the surface, the key quantity which characterises the linear response of a flat surface is the so-called d-parameter [1, 2, 3]. The d-parameter is a complex and frequency-dependent quantity which is defined as the centroid $d(\omega)$ of the screening density induced by a uniform electric field oriented perpendicular to the surface. Among observable quantities that are directly determined by $d(\omega)$ are the surface photoelectric yield (measured in photoemission), the linear coefficient of the surface plasma dispersion relation (measured in electron energy loss spectroscopy) and nonlocal corrections to the classical theory of reflection and refraction (measured in ellipsometry experiments) [1].

This quantity can be conveniently calculated by imposing a potential of the form (the metal occupies the half-space $z < 0$)

$$v^{ext}(z,\omega) = \frac{2\pi}{q} e^{i\mathbf{q}_{\|}\cdot\mathbf{R}+qz-i\omega t} \qquad q = |\mathbf{q}_{\|}| \tag{10.1}$$

and calculating the induced charge density in the long-wavelength limit ($q \to 0$).

In this chapter we calculate the dielectric response to the above potential. This limited scope has the advantage that one needs to consider (scalar) density and not (vector) current response, and solve Poisson's equation instead of the full Maxwell's equations.

Evaluating the response of the surface to the above external perturbation requires the solution of a set of integral equations for the induced charge density and potential. Because of broken symmetry at the surface and the non-local nature of the response, the range of integration in these equations extends to infinity in the direction normal to the surface. A major problem in evaluating the surface response is to reduce these integral equations to a compact domain suitable for numerical treatment. Just as in the case of ground state calculations, one possible way of circumventing the problem is to model the semi-infinite system by a slab of finite thickness. However, if the slab is to represent semi-infinite solid, the slab thickness L must satisfies $L \gg 1/q$. Thus from a practical point of view it is difficult to study the long-wavelength dynamic response (the small q limit) using finite slabs.

Here we tackle the above problem within the jellium model of the semi-infinite metal. We show that by finding an approximate form of the asymptotic potential deep inside the metal and making explicit use of this form, it is possible to reduce the response equations to a set of integral equations over a rather small region around the surface. Solving these reduced response equations we obtain, below the bulk plasma frequency, accurate results for the dynamic response of the *semi-infinite* system, and in particular the d-parameter.

Our jellium calculations are similar in spirit to those of Feibelman [4] and especially of Liebsch [5]. However, unlike the work of Feibelman, our calculational method does not require any knowledge of the analytic structure of the bulk dielectric function and gives accurate results in the whole range of frequencies below the bulk plasma frequency. In the work of Liebsch a set of equations for the charge and potential fluctuations away from a guessed model function is solved self-consistently on a real-space mesh. Our method does not need such model guesses and the response equations are solved by expanding the quantities of interest in a set of basis functions and inverting the resulting matrix equation for the coefficients. The ultimate aim of this work is to develop a method which can be applied to more realistic systems with band-structure included. There are still great difficulties in solving this important problem which we shall discuss in the final section.

10.1 Linear response formalism

Basic equations

We consider the response of an interacting electronic system to an externally imposed time-varying potential $V^{ext}(\mathbf{r},t)$ of the form

$$V^{ext}(\mathbf{r},t) = V^{ext}(\mathbf{r},\omega)e^{-\imath\omega t}. \tag{10.2}$$

This potential will induce a polarisation potential $V^{\imath nd}(\mathbf{r},t)$ in the solid. For sufficiently weak external potentials we may ignore all higher harmonics and assume that the induced potential oscillates in time at the same frequency as the external potential

$$V^{\imath nd}(\mathbf{r},t) = V^{\imath nd}(\mathbf{r},\omega)e^{-\imath\omega t}. \tag{10.3}$$

We now consider the linear response of the system to the total potential which is the sum of the external potential, and the polarisation potential induced by the latter:

$$V^{tot} = V^{ext} + V^{\imath nd}. \tag{10.4}$$

The induced potential is given by:

$$V^{\imath nd}(\mathbf{r},\omega) = \int d\mathbf{r}' \frac{\delta n(\mathbf{r}',\omega)}{|\mathbf{r}-\mathbf{r}'|}. \tag{10.5}$$

In this equation δn is the linearly induced density in the system which is related to the total potential through the non-local frequency dependent polarisability χ by the following equation:

$$\delta n(\mathbf{r},\omega) = \int d\mathbf{r}' \chi(\mathbf{r},\mathbf{r}',\omega) V^{tot}(\mathbf{r}',\omega). \tag{10.6}$$

The above set of equations uniquely specify the linear properties of the electronic system in the presence of an external potential, and is the starting point of our further analysis.

Time-dependent density functional approximation

First order time-dependent perturbation theory shows [6] that the polarisability of an interacting electronic system can be be written as the time Fourier transform of a retarded density-density correlation function,

$$\chi(\mathbf{r},\mathbf{r}';t-t') = -i\theta(t-t') < 0|[\hat{n}(\mathbf{r},t)\hat{n}(\mathbf{r}',t')]|0 > . \tag{10.7}$$

In this expression $\theta(t-t')$ is the unit step-function, $|0>$ the exact many particle ground state of electrons and $\hat{n}$ the Heisenberg density operator

$$\hat{n}(\mathbf{r},t) = \hat{\Psi}^{\dagger}(\mathbf{r},t)\hat{\Psi}(\mathbf{r},t) \tag{10.8}$$

with $\hat{\Psi}(\mathbf{r},t)$ the field operator in the Heisenberg picture.

Calculating χ requires knowledge of the ground state of the interacting system which is usually not available. In order to calculate the response of the system to an external potential one usually approximates χ by the polarisability of the corresponding non-interacting system. This is the random phase approximation (RPA) [6]. A simple way to go beyond RPA and include short-range correlations is the time-dependent density functional (TDLDA) approximation [7]. In this approximation one sets $\chi = \chi^0$, with χ^0 the polarisability of the non-interacting Kohn-Sham electrons, and replaces the induced potential (10.5) by

$$V^{ind}(\mathbf{r},\omega) = \int d\mathbf{r}' \frac{\delta n(\mathbf{r}',\omega)}{|\mathbf{r}-\mathbf{r}'|} + \frac{\partial v_{xc}}{\partial n}\Big|_{n=n_0(\mathbf{r})} \delta n(\mathbf{r},\omega) \tag{10.9}$$

where v_{xc} is the exchange-correlation potential calculated within the local density approximation and $n_0(\mathbf{r})$ is the ground state electron density.

The polarisability χ^0 is given in terms of the eigenvalues and eigenfunctions of the Kohn-Sham Hamiltonian by the equation:

$$\chi^0(\mathbf{r},\mathbf{r}',\omega) = 2\sum_{ij}(f_i - f_j)\frac{\phi_i^*(\mathbf{r})\phi_j(\mathbf{r})\phi_j^*(\mathbf{r}')\phi_i(\mathbf{r}')}{\omega - (\epsilon_j - \epsilon_i) + i\delta} \tag{10.10}$$

with f_i the zero temperature Fermi distribution function and δ a positive infinitesimal. The factor 2 represents the spin summation.

The evaluation of the LDA polarisability requires an explicit sum over the complete spectrum of the LDA effective Hamiltonian. That is, we not only require the occupied states calculated simultaneously with the effective potential but the infinite number of unoccupied states as well. Furthermore, in more realistic systems if the evaluation of χ^0 is to be based on a linearised band structure calculation method, it is preferable to avoid *explicit* use of the unoccupied states since these states may be poorly known.

One can circumvent the above problem by use of the Green function $G(\mathbf{r},\mathbf{r}';E)$ associated with the LDA Hamiltonian. Using the spectral representation of the Green function (section 1.3) one can express the sums in (10.10) in terms of G. This results in the following closed-form expression for χ^0:

$$\chi^0(\mathbf{r},\mathbf{r}',\omega) = -\frac{2}{\pi}\int_0^{E_F} dE Im[G(\mathbf{r},\mathbf{r}';E)][G(\mathbf{r},\mathbf{r}';E+\omega) + G^*(\mathbf{r},\mathbf{r}';E-\omega)]. \tag{10.11}$$

In the remaining of this work we shall adopt the TDLDA approximation. The use of TDLDA instead of RPA has the advantage of treating the ground state and excitation properties on the same level of approximation. For the particular case of surface calculations, this is necessary in order for a number of surface sum-rules for the d-parameter to hold [5, 8].

10.2 The jellium model

In the jellium model of an infinitely extended metal the discrete ion cores are replaced by a uniform positive background charge with density equal to the spatial average of the ion charge distribution. The electrostatic potential created by this charge distribution replaces the ion-electron potential. For the analogous surface problem, the semi-infinite ion lattice is smeared out similarly into a uniform positive charge that fills half of space:

$$n_+(\mathbf{r}) = \begin{cases} \bar{n} & z \leq 0 \\ 0 & z > 0. \end{cases} \tag{10.12}$$

Here, z is the direction normal to the surface. The positive background charge density $\bar{n}$ is expressed in terms of r_s, the Wigner radius as:

$$(4\pi/3)r_s^3 = 1/\bar{n}. \tag{10.13}$$

Typical values of r_s range from about 2 to 5. The bulk plasma frequency of jellium ω_p is given (in atomic units) by [9]

$$\omega_p = (4\pi\bar{n})^{1/2} \tag{10.14}$$

and the frequency-dependent dielectric function $\epsilon(\omega)$ is given by the Drude formula [9]

$$\epsilon(\omega) = 1 - \omega_p^2/\omega^2. \tag{10.15}$$

The total screening charge density $\sigma(\omega)$ induced at the surface by a uniform frequency-dependent external field $E_0 = 2\pi$, oriented normal to the surface is given by [10]

$$\sigma(\omega) = \frac{\epsilon(\omega) - 1}{\epsilon(\omega) + 1}. \tag{10.16}$$

This quantity diverges when

$$\epsilon(\omega) + 1 = 0 \tag{10.17}$$

defining the energy of the long-wavelength surface plasmon ω_{sp} in terms of the bulk dielectric function. Using the Drude formula for ϵ one finds:

$$\omega_{sp} = \frac{\omega_p}{\sqrt{2}}. \tag{10.18}$$

Basic integral equations

Within the formalism outlined in section 10.1, we wish to calculate the response of a jellium surface to an external potential of the form

$$V^{ext}(\mathbf{r}, t) = -\frac{2\pi}{q} e^{\imath \mathbf{q}_{\|} . R_{\|} + qz - \imath\omega t} \tag{10.19}$$

in the long-wavelength limit. Since the system is translationally invariant in the direction parallel to the surface, we can Fourier transform the $x - y$ coordinates to obtain a more convenient representation of the response equations. In the $q \to 0$ limit these equations are:

$$V^{ext}(z) = -2\pi z \tag{10.20}$$

$$\delta n(z,\omega) = \int dz' \chi^0(z,z',\omega)[V^{ext}(z') + V^{ind}(z',\omega)] \tag{10.21}$$

$$V^{ind}(z,\omega) = \int dz' k(z,z')\delta n(z',\omega) \tag{10.22}$$

$$k(z,z') = -2\pi|z-z'| + \delta(z-z')\frac{\partial v_{xc}}{\partial n}\Big|_{n(z')=n_0(z')} \tag{10.23}$$

where $-2\pi|z-z'|$ is the $\mathbf{q}_{||} = \mathbf{0}$ component of the Coulomb potential and the response function $\chi^0(z,z',\omega)$ is given by:

$$\chi^0(z,z',\omega) = -\frac{1}{\pi^2}\int_0^{E_f} dE(E_F - E)ImG(z,z';E)[G(z,z';E+\omega) + G^*(z,z';E-\omega)] \tag{10.24}$$

with $G(z,z';E)$ satisfying

$$[-\frac{1}{2}\frac{d^2}{dz^2} + v_{eff}(z) - E]G(z,z';E) = \delta(z-z') \tag{10.25}$$

and outgoing wave boundary conditions at $\pm\infty$.

The d-parameter: definition and properties

The linear response function of a jellium surface in the long-wavelength limit $d(\omega)$ is defined as the centroid of the charge density induced by a uniform electric field oriented perpendicular to the surface:

$$d(\omega) = \frac{\int dz z\delta n(z,\omega)}{\int dz\delta n(z,\omega)} = \frac{1}{\sigma(\omega)}\int dz z\delta n(z,\omega). \tag{10.26}$$

For $\omega \neq 0$, $d(\omega)$ is a complex number. It defines the frequency-dependent image-plane position according to the formula [10]

$$z_0(\omega) = \frac{\epsilon(\omega)}{\epsilon(\omega)+1}d(\omega). \tag{10.27}$$

In the static limit ($\omega = 0$) this reduces to $z_0(0)$, the reference plane position of the image potential experienced by a point charge outside the surface (see part II).

The absorptive part of the centroid, $Imd(\omega)$, represents the power absorption by the surface due to excitation of electron-hole pairs and to plasmons, if $\omega > \omega_p$. To see this we use equations (10.21) to rewrite $d(\omega)$ as

$$d(\omega) = \frac{1}{\sigma(\omega)}\int dz z\int dz' \chi^0(z,z',\omega)V^{tot}(z',\omega). \tag{10.28}$$

Putting

$$z = -\frac{V^{ext}(z)}{2\pi} \tag{10.29}$$

and using the fact that $\sigma(\omega)$ is a real quantity, we can write

$$Imd(\omega) = -\frac{1}{2\pi\sigma(\omega)} Im \int dz V^{ext}(z) \int dz' \chi^0(z, z', \omega) V^{tot}(z', \omega). \tag{10.30}$$

Now, expanding the imaginary part as $ImB = (B^* - B)/2\imath$ and using the self-consistent integral equation

$$V^{tot}(z, \omega) = V^{ext}(z, \omega) + \int dz_1 \int dz_2 K(z, z_1) \chi^0(z_1, z_2, \omega) V^{tot}(z_2, \omega) \tag{10.31}$$

obtained from (10.21) and (10.22), we obtain after some algebra

$$Imd(\omega) = -\frac{1}{2\pi\sigma(\omega)} \int dz (V^{tot}(z, \omega))^* \int dz' Im(\chi^0(z, z', \omega)) V^{tot}(z', \omega). \tag{10.32}$$

Finally, writing out $\chi^0(z, z', \omega)$ explicitly in terms of eigenfunctions and eigenvalues of (10.25), denoted by $\phi_\imath(z)$ and $\epsilon_\imath$, and using the relation

$$ImG(z, z'; E) = \pi \sum_\imath \phi_\imath(z) \phi_\imath^*(z') \delta(E - \epsilon_\imath) \tag{10.33}$$

we find

$$Imd(\omega) = \frac{1}{2\pi\sigma(\omega)} \sum_{\imath\jmath} (E_F - \epsilon_\imath) f_\imath (1 - f_\jmath) | < \jmath | V^{tot} | \imath > |^2 \delta(\epsilon_\jmath - \epsilon_\imath - \omega), \tag{10.34}$$

which corresponds to the the Golden Rule expression [9] for the rate at which electron-hole pairs are excited in the system by the *total* potential. From (10.34) it follows that

$$Im(d(\omega)) \geq 0 \tag{10.35}$$

independent of frequency.

The centroid $d(\omega)$ is a causal response function which satisfies the Kramers-Kronig relations

$$Red(\omega) = \frac{2}{\pi} P \int_0^\infty d\omega' \frac{\omega' Imd(\omega')}{(\omega')^2 - \omega^2} \tag{10.36}$$

$$Imd(\omega) = -\frac{2}{\pi} P \int_0^\infty d\omega' \frac{\omega Red(\omega')}{(\omega')^2 - \omega^2}. \tag{10.37}$$

From these relations and the known high-frequency behaviour of $d(\omega)$ [11], one can derive several frequency sum rules, e.g.,

$$\int_0^\infty d\omega \omega Imd(\omega) = \lambda(r_s) \omega_p^2 \tag{10.38}$$

$$\int_0^\infty d\omega Red(\omega) = 0 \tag{10.39}$$

where

$$\lambda(r_s) = \frac{\pi}{2}\int_0^\infty \frac{n_0(z)}{\bar{n}} \tag{10.40}$$

only depends on the ground-state electron density profile. We note that the integrand in (10.39) should change sign so that as a function of frequency the real part of the centroid will pass from one side of the jellium background edge ($z = 0$) to the other.

Another extremely useful sum rule for $d(\omega)$ is the so called force-sum rule which was derived by Sorbello [12] for atoms and finite systems and generalised to the semi-infinite jelium by Liebsch [5]. According to this sum rule, the first moment of the induced charge density inside the metal is related to the first moment outside through the relation

$$\frac{1}{\epsilon(\omega)}\int_0^\infty dzz\delta n(z,\omega) + \int_{-\infty}^0 dzz\delta n(z,\omega) = 0 \tag{10.41}$$

provided that electron-electron interactions are approximated on the same level in the ground state and the response calculations [5].

We note that direct numerical evaluation of $d(\omega)$ from (10.26) is difficult because of the slowly decaying Friedel oscillations which the induced charge density exhibits in the interior of the metal. Following Liebsch [5] we obtain from (10.41) the following alternative expression for $d(\omega)$:

$$d(\omega) = \frac{\epsilon(\omega)+1}{\epsilon(\omega)}\int_0^\infty dzz\delta n(z,\omega) \tag{10.42}$$

showing that $d(\omega)$ can be directly calculated from the induced charge density outside the surface.

Ground state, and one-electron Green function

The ground state calculations are done within the LDA (using von Barth-Hedin [13] parameterisation of the exchange-correlation potential), combined with the embedding method [14] to treat the semi-infinite metal. Only the embedded region $\eta_1 \le z \le \eta_2$ is treated explicitly, and the effects of the bulk jellium ($z < \eta_1$) and the vacuum ($z > \eta_2$) are expressed in terms of the embedding potentials acting over the embedding planes $z = \eta_1$ and $z = \eta_2$. The Green function in the embedded region is expanded in a set of non-orthogonal plane waves

$$h_i(z) = \frac{1}{\sqrt{D}}e^{ik_i z} \qquad k_i = \frac{2\pi}{L}i \tag{10.43}$$

as

$$G(z,z';E) = \sum_{ij}\mathcal{G}_{ij}(E)h_i(z)h_j^*(z') \tag{10.44}$$

where $D = \eta_2 - \eta_1$ and L is chosen somewhat larger than D. The coefficients $\mathcal{G}_{ij}$ satisfy

$$\sum_k\left[H_{ik} + (\Sigma_V(E))_{ik} + (\Sigma_J(E))_{ik} - EO_{ik}\right]\mathcal{G}_{kj}(E) = \delta_{ij}. \tag{10.45}$$

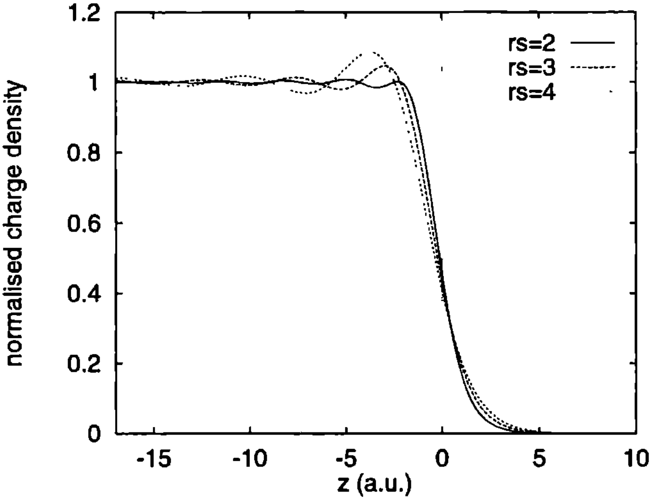

Figure 10.1: Normalised electron density profile $n(z)/\bar{n}$ calculated for simple metal surfaces with bulk densities corresponding to $r_s = 2, 3$ and 4 a.u.

Here, H_{ik} is the matrix element of the Hamiltonian in the embedded region plus additional normal-derivative terms at the embedding planes to ensure hermiticity, O_{ik} is the overlap matrix and $(\Sigma_v(E))_{ik}$ and $(\Sigma_j(E))_{ik}$ are the matrix elements of the vacuum and jellium embedding potentials respectively.

The matrix elements of the jellium embedding potential are given by:

$$(\Sigma_J(E))_{ik} = \sqrt{2E} h_i^*(\eta_1) h_k(\eta_1) \tag{10.46}$$

where the energy is measured from the bottom of the jellium band. The matrix elements of the vacuum embedding potential are obtained from (10.46) by replacing η_1 with η_2 and E with $E - E_v$, where E_v is the vacuum level which must be calculated self-consistency.

The Hamiltonian in the embedded region is given by

$$H = -\frac{1}{2}\frac{d^2}{dz^2} + v_{eff}(z) \tag{10.47}$$

with v_{eff} calculated self-consistently from

$$v_{eff}(z) = -2\pi \int_{\eta_1}^{\eta_2} dz' |z - z'| [n_o(z') - n_+(z')] + v_{xc}(n_o(z)). \tag{10.48}$$

The electron density is obtained from

$$n_o(z) = \frac{1}{\pi^2} \int_0^{E_F} dE (E_f - E) Im G(z, z'; E), \tag{10.49}$$

where the energy factor comes from averaging over the $x-y$ components of the wavevector. In figure 10.1 the normalised ground state electron densities $n_0(z)/\bar{n}$ is shown for several r_s values.

The above procedure yields the Green function only within the embedded region in which (10.44) is a valid expansion. In solving the linear response equations, however, we require $\chi^0(z,z';\omega)$, and hence $G(z,z';E)$, in the entire space. Once G is calculated within the embedded region, we can extend it into the bulk using the matching Green function method [15]. This yields:

$$G(z,z';E) = G(z,\eta_1;E)e^{-ik(z'-\eta_1)} \qquad z \geq \eta_1, \quad z' \leq \eta_1 \tag{10.50}$$

and

$$G(z,z';E) = \frac{e^{ik|z-z'|}}{-ik} + \left[\frac{1}{ik} + G(\eta_1,\eta_1;E)\right] e^{-ik(z+z'-2\eta_1)} \qquad z,z' \leq \eta_1 \tag{10.51}$$

with $k = \sqrt{2E}$. Similar expressions can be derived for the Green function in the vacuum. We note that the accuracy of the above "off-diagonal" Green function depends on the accuracy of $G(z,z';E)$ calculated when z,z' or both are on the embedding plane. We checked this numerically by calculating the Green function for a larger embedded region and found very good agreement with the results obtained from (10.50).

10.3 Reduced response equations for jellium

The main problem in solving the response equations is that because of the inhomogeneity introduced by the surface, the response function $\chi^0(z,z',\omega)$ is not only a function of the relative distance $|z-z'|$ but also depends on $z+z'$. Consequently, it is not possible to reduce the set of response equations to algebraic equations using Fourier transformation. On the other hand, because of the long-range character of the Coulomb kernel $|z-z'|$, simply truncating the integration range at any finite cut off results in significant errors in the induced charge density profile in the resulting finite system. The remainder of this section is devoted to an analytical scheme for reducing the response equations to a set of equations over a compact domain which can be treated numerically.

The first step in this direction is to realise that $\chi^0(z,z',\omega)$ is negligibly small if either z or z' is a few atomic units outside the surface. This can be easily seen from (10.24) since the first Green function in this expression is evaluated at energies below the Fermi level and hence decays rapidly outside the surface. Thus the upper limit of integrations in (10.21) can be safely replaced by a finite cut-off Z_v lying a few atomic units outside the surface. On the other hand, beyond a certain "microscopic distance" inside the metal $\chi^0(z,z',\omega)$ heals to its bulk form:

$$\chi^0(z,z',\omega) \approx \chi^h(|z-z'|,\omega) \tag{10.52}$$

with χ^h the response function of a uniform electron gas. This information implies that the total potential behaves asymptotically already at microscopic distances inside the metal. The remaining problem then is to find this asymptotic form.

For the jellium model, a thorough analysis of this problem has been given by Feibelman [4] who showed that the $z \to -\infty$ behaviour of the field is determined by the singularities of the bulk dielectric function $\epsilon(q, \omega)$ in the complex q plane. These can be investigated in detail once the explicit form of this quantity is calculated. Feibelman used the Lindhard dielectric function [9] for bulk jellium and found [4] the following asymptotic form of the electric field $E(z)$

$$E(z) = \frac{E^{out}}{\epsilon(\omega)} \left\{ 1 + pe^{ik_p z} + c_j \frac{e^{i\kappa_j z}}{z^2} \right\} \qquad z \to -\infty \tag{10.53}$$

where E^{out} is the electric field far outside the surface, The term $e^{ik_p z}$ in this expression is due to the plasmon pole of the dielectric function and is non-zero only above the bulk plasma frequency. The remaining oscillatory terms are the Friedel oscillations associated with the sharp edge of the Fermi sea and the set $\{\kappa_j\}$ is determined from the branch cuts of $\epsilon(q, \omega)$ in the complex q plane.

In the work of Feibelman the unknown coefficients $\{c_j, p\}$ are obtained by an iterative procedure in which the asymptotic form (10.53) is fitted to the solution in the surface region from which a new guess for $E(z)$ inside the metal is found. At low frequencies ($\omega < 0.5\omega_p$), however, numerical problems arise since several $\{\kappa_j\}$ are nearly equal and the method becomes unstable.

We adopt here a more practical way of estimating the asymptotic form which results in a stable scheme in the whole range of frequencies below the bulk plasma frequency. More importantly, our scheme does not require a detailed knowledge of the bulk dielectric function which might not be available in more realistic situations.

Since the exchange-correlation part of the induced potential becomes negligibly small inside the metal, we concentrate on the asymptotic form of the electrostatic part. Our main assumption is that, below the bulk plasma frequency, the induced charge density is reasonably localised in a macroscopic region around $z = 0$. We then define a cut-off Z_b sufficiently far inside the metal beyond which the induced charge density is small as compared to the surface charge density. With this "localisation" assumption, the induced potential at an arbitrary point z can be approximated by:

$$V^{ind}(z, \omega) = -2\pi \int_{Z_b}^{Z_V} dz' |z - z'| \delta n(z', \omega). \tag{10.54}$$

For $z < Z_b$ this yields the asymptotic form of the bulk potential

$$V^{tot}(z, \omega) = 2\pi(\sigma_s - 1)z - 2\pi\sigma_s d_s. \tag{10.55}$$

Here, σ_s is the total screening charge induced in the surface and d_s is its centre of gravity:

$$\sigma_s(\omega) = \int_{Z_b}^{Z_v} dz \delta n(z, \omega), \tag{10.56}$$

$$\sigma_s(\omega) d_s(\omega) = \int_{Z_b}^{Z_v} dz z \delta n(z, \omega). \tag{10.57}$$

Similarly, the asymptotic potential far in the vacuum becomes:

$$V^{tot}(z,\omega) = -2\pi(\sigma_s + 1)z + 2\pi\sigma_s d_s \qquad z > Z_v. \tag{10.58}$$

With the above expressions for the asymptotic potentials, the ratio of the electric field far outside the metal E^{out} to the field inside E^{in} is given by:

$$\frac{E^{out}(\omega)}{E^{in}(\omega)} = -\frac{\sigma_s + 1}{\sigma_s - 1} \tag{10.59}$$

For perfect screening we must have

$$\frac{E^{out}}{E^{in}} = \epsilon(\omega) \tag{10.60}$$

independent of the details of the surface. Thus, ideally, the total induced charge density should satisfy

$$\sigma_s = \frac{\epsilon - 1}{\epsilon + 1} \tag{10.61}$$

which is a useful check of our localisation assumption.

Substitution of the asymptotic expression (10.55) in (10.21) gives for the induced charge density in the surface region

$$\begin{aligned} \delta n(z,\omega) &= \int_{Z_b}^{Z_v} dz'\chi^0(z,z',\omega)[V^{ext}(z') + V^{ind}(z',\omega)] \\ &+ \int_{-\infty}^{Z_b} dz'\chi^0(z,z',\omega)[2\pi(\sigma_s - 1)z' - 2\pi\sigma_s d_s]. \end{aligned} \tag{10.62}$$

Using the identity [1]

$$\int_{-\infty}^{\infty} dz'\chi^0(z,z',\omega) = 0 \tag{10.63}$$

(10.62) becomes

$$\delta n(z,\omega) = \int_{Z_b}^{Z_v} dz'\chi^0(z,z',\omega)[V^{ext}(z') + V^{ind}(z',\omega) + 2\pi\sigma_s d_s] + (\sigma_s - 1)\delta n^{bs}(z,\omega) \tag{10.64}$$

where δn^{bs} is the charge density induced in the surface region by the asymptotic bulk potential:

$$\delta n^{bs}(z,\omega) = 2\pi \int_{-\infty}^{Z_b} dz'\chi^0(z,z',\omega)z' \tag{10.65}$$

and the induced potential in the surface region is given by:

$$V^{ind}(z,\omega) = -2\pi \int_{Z_b}^{Z_v} dz'|z - z'|\delta n(z',\omega) + \frac{\partial v_{xc}}{\partial n}\Big|_{n(z)=n_0(z)} \delta(z,\omega). \tag{10.66}$$

---

[1] This identity simply states that a constant potential does not induce any charge density in the system.

Calculating δn^{bs} requires integrating (10.65) over the bulk half-space. Substituting (10.24) in (10.65) and changing the order of integration we find:

$$\begin{aligned}\delta n^{bs}(z,\omega) &= -\frac{2}{\pi}\int_0^{E_f} dE(E-E_F)\times \\ &\quad \Big\{\int_{-\infty}^{Z_b} dz' ImG(z,z';E)[G(z,z';E+\omega)+G^*(z,z';E-\omega)]\Big\}. \qquad (10.67)\end{aligned}$$

Using expression (10.50) for the "off-diagonal" Green function, the z'-integrations in (10.67) can be performed analytically. The resulting energy integrals are then performed using numerical integration.

In this way we end up with a set of integral equations for the induced charge density and potential which need to be solved explicitly only in the surface region. The bulk effects are taken into account through the term δn^{bs}. The numerical solution of these equations will be discussed in the following section.

10.4 Computational procedure and details

Inserting expansion (10.44) for the Green function in (10.24) we find that the response function in the surface region can be expanded in the form:

$$\chi^0(z,z',\omega) = \sum_{ij} \chi^0_{ij}(\omega) e^{ik_i z} e^{-ik_j z'}. \qquad (10.68)$$

In the same way $\delta n^{bs}(z,\omega)$ can be expanded as

$$\delta n^{bs}(z,\omega) = \sum_i \delta n_i^{bs}(\omega) e^{ik_i z}. \qquad (10.69)$$

The above equations suggest expanding the induced charge density in the same form:

$$\delta n(z,\omega) = \sum_i \delta n_i(\omega) e^{ik_i z}. \qquad (10.70)$$

By inserting (10.68)-(10.70) into (10.64) we obtain:

$$\delta n_i = \sum_j \chi^0_{ij}[V_j^{ext} + V_j^{ind}] + \sum_{jk} \chi^0_{ij} D_{jk} \delta n_k + (\sigma_s - 1)\delta n_i^{bs} \qquad (10.71)$$

where

$$\begin{aligned} V_j^{ext} &= \int_{Z_b}^{Z_v} dz' e^{-ik_j z'} V^{ext}(z',\omega) \\ V_j^{ind} &= \int_{Z_b}^{Z_v} dz' e^{-ik_j z'} V^{ind}(z',\omega) \qquad (10.72)\end{aligned}$$

and

$$D_{jk} = 2\pi \int_{Z_b}^{Z_v} dz' \int_{Z_b}^{Z_v} dz'' e^{-ik_j z'} z'' e^{ik_k z''} \qquad (10.73)$$

Using (10.66) V_j^{ind} can be written as:

$$V_j^{ind} = \sum_k Y_{jk}\delta n_k + \sum_k X_{jk}\delta n_k \tag{10.74}$$

where Y_{jk} and X_{jk} are the matrix elements of the Coulomb potential and the exchange-correlation potential respectively:

$$Y_{jk} = -2\pi \int_{Z_b}^{Z_v} dz' \int_{Z_b}^{Z_v} dz'' e^{-ik_j z'} |z' - z''| e^{ik_k z''}, \tag{10.75}$$

$$X_{jk} = \int_{Z_b}^{Z_v} dz' e^{-ik_j z'} \frac{\partial v_{xc}}{\partial n}\Big|_{n(z')=n_0(z')} e^{ik_k z'}. \tag{10.76}$$

Finally, substituting (10.74) in (10.71) we end up with the following equation (written in matrix form) for the induced charge:

$$\delta\mathbf{n} = \delta\mathbf{n}^{ext} + \chi^0[\mathbf{X} + \mathbf{Y} + \mathbf{D}]\delta\mathbf{n} + (\sigma_s - 1)\delta\mathbf{n}^{bs} \tag{10.77}$$

where

$$\delta n_i^{ext} = \sum_j \chi_{ij}^0 V_j^{ext} \tag{10.78}$$

The above equation is readily inverted to give the induced charge density:

$$\delta\mathbf{n} = \Big[\mathbf{I} - \chi^0(\mathbf{X} + \mathbf{Y} + \mathbf{D})\Big]^{-1}\Big(\delta\mathbf{n}^{ext} + (\sigma_s - 1)\delta\mathbf{n}^{bs}\Big) \tag{10.79}$$

where $\mathbf{I}$ is the identity matrix [2]. The total induced charge density σ_s in the above equation may be eliminated using (10.56). However, in order to check the consistency of our localisation assumption we treated σ_s as an unknown quantity and solve equation (10.79) iteratively. Thus, starting with an initial guess for the total induced charge, $\delta\mathbf{n}$ is obtained from (10.79) and a new guess for σ_s generated. This procedure is repeated until self-consistency is reached. This iterative scheme works very well. In particular, with the initial guess

$$\sigma_s^0(\omega) = \frac{\epsilon(\omega) - 1}{\epsilon(\omega) + 1} \tag{10.80}$$

the procedure converges rapidly to its self-consistent solution (i.e. the difference between the input and output σ_s is less than 1%) showing the internal consistency of the calculations.

The linear response calculations are performed at real frequencies without introducing any additional damping term to suppress bulk Friedel oscillations. Evaluating the response function χ_{ij}^0 requires calculating products of Green functions within an energy integration loop and forms the major part of the computational effort. The energy integrations are performed along the real axis and with Gaussian quadrature. Up to 200 energy points were used to assure convergence and special care was taken to ensure an accurate integration over cusps of χ^0 which were found to occur at $E = \omega$ and $E = E_v$.

---

[2] $\Big[\mathbf{I} - \chi^0(\mathbf{X} + \mathbf{Y} + \mathbf{D})\Big]$ becomes singular at the surface plasmon frequency.

10.5 Results

We performed calculations for metals with densities corresponding to $r_s = 2, 3$, and 4 a.u. and in the whole frequency range below the bulk plasma frequency. Before discussing the results, we examine the sensitivity of our calculations to the value of the bulk cut-off distance Z_b, which defines the length of our actual structure and hence the usefulness of our scheme. The vacuum cut-off is always fixed at $Z_v = 17$ a.u.

Finite size effects

Figures 10.2 and 10.3 show the real and imaginary parts of the induced charge density for $r_s = 3$ calculated at $\omega = 0.3\omega_p$ and $\omega = 0.6\omega_p$. The bulk cut-off is varied between $Z_b = -32$ and $Z_b = -52$ a.u. We see that for $\omega = 0.3\omega_p$ the profile of $Re\delta n(z,\omega)$ converges very rapidly and there is excellent agreement between the three calculations. The agreement is less good at $\omega = 0.6\omega_p$ since Friedel oscillations in the interior of the metal have a relatively large amplitude at this frequency. Nevertheless, with $Z_b = -32$ a.u. the overall shape of the induced charge density in the vicinity of the surface is still very well reproduced. Note in particular that the large peak around $z = 0$ and the tail of the screening charge outside the surface are practically unaffected by the choice of Z_b. The results for the imaginary part show essentially the same behaviour but the "finite size" errors are relatively larger.

We now consider the sensitivity of the d-parameter to the length of the surface region. The real and imaginary parts of $d(\omega)$ calculated for $r_s = 3$ and with $Z_b = -22, -32$ and -42 a.u. are shown in figure 10.4. The results obtained for $Z_b = -32$ and $Z_b = -42$ a.u. are almost identical, indicating that $d(\omega)$ can be accurately calculated using rather modest values of the cut-off distance. The agreement with the shortest structure, however, is less satisfactory. The largest errors (i.e. the difference between the results for $Z_b = -22$ and $Z_b = -42$ a.u.) occur at frequencies above the photoemission threshold $\omega = \Phi = 0.38\omega_p$, with Φ the work function. At these frequencies, Friedel oscillations become significant and penetrate deep inside the bulk. Neglecting these oscillations in the region beyond Z_b results in an error in the total potential which affects the tail of the induced charge outside the surface. These non-local effects however have a finite range determined by the non-locality of the response function and become smaller as Z_b is moved further away from the surface. This is indicated by the excellent agreement between the results for the two longer structures.

Induced densities and fields

In figures 10.5 and 10.6 we show the real and imaginary parts of the induced charge density for $r_s = 3$ at several frequencies below ω_p. The calculations were performed with the cut off distances $Z_v = 17$ and $Z_b = -52$ a.u. The real part of $\delta n(z,\omega)$ is built up of a big peak localised near $z = 0$ accompanied by Friedel oscillation penetrating into the bulk. At $\omega = 0.1\omega_p$ we are almost in the static situation. In this case the big surface peak

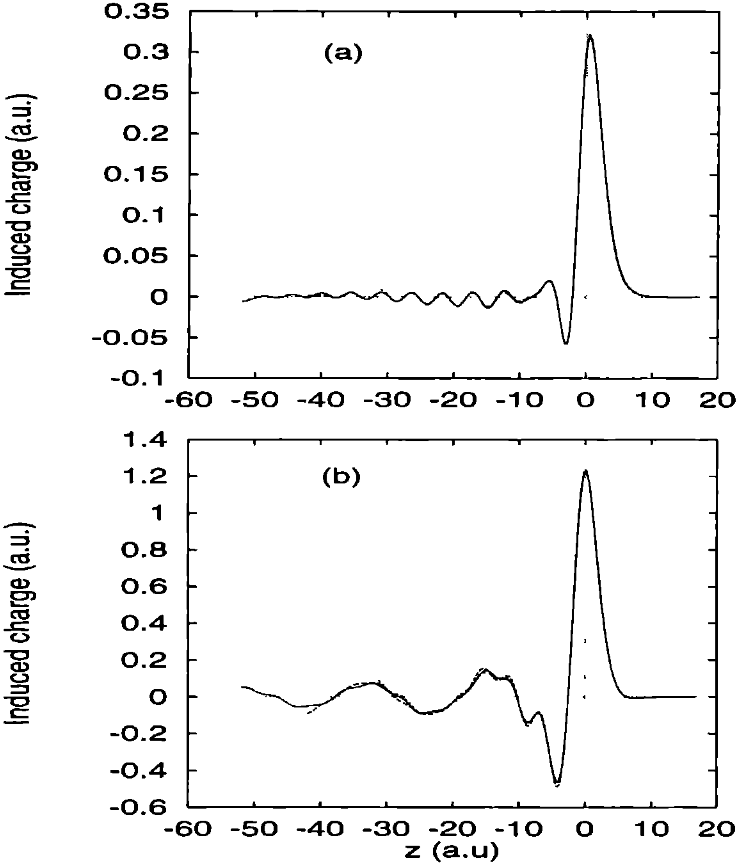

Figure 10.2: Real part of electron density induced by a uniform electric field oriented normal to the surface, calculated at $\omega = 0.3\omega_p$ (a) and $\omega = 0.6\omega_p$ (b) for three different bulk cut off distances $Z_b = -32$ (short dashed lines), $Z_b = -42$ (dashed lines) and $Z_b = -52$ a.u. (solid lines). The bulk density corresponds to $r_s = 3$.

is the analogy of the classical "surface charge" (a delta-function located at the geometrical surface $z = 0$). The static Friedel oscillations are associated with the sharp cut-off at the the Fermi energy and are characterised by a single wavelength $\lambda_s = \pi/k_f$, which is 4.9 a.u. for $r_s = 3$. As ω increases, the surface peak shifts gradually outwards indicating that screening takes place mainly in the tail of the electron charge density. In contrast to the static case, the dynamic Friedel oscillations attain a complicated shape and are not characterised by a single wavelength. Note that unlike the real part, the imaginary part of $\delta n(z,\omega)$ has a dipole character near $z = 0$. In fact, in the absence of bulk absorption processes (i.e. $Im(\epsilon) = 0$) the integrated weight of this quantity should vanishes as can

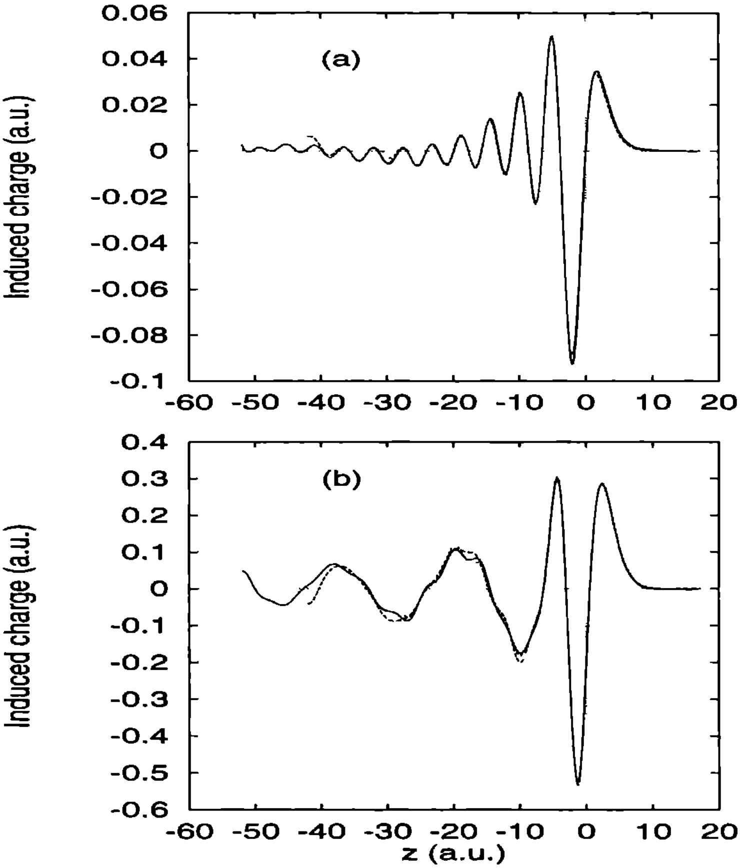

Figure 10.3: The same as figure 10.2 but for the imaginary part.

be seen from equation (10.16).

Above the threshold for photoemission $\omega = \Phi$ ($\omega/\omega_p = 0.38$) the real part of $\delta n(z,\omega)$ changes noticeably, the main peak shifts towards the jellium edge and with a modification of the periode of the Friedel oscillations. The imaginary part is greatly enhanced at these frequencies. These changes are caused by the opening of new channels associated with excitations from occupied states to extended unoccupied states just above the vacuum level. Numerically, the change is caused by a singularity in the excited state Green function $G(z,z',E+\omega)$ at $E+\omega = E_v$ which enters the energy integration range for calculating χ^0 at the critical frequency $\omega = \Phi$.

Above the photoemission threshold, the dominant Friedel oscillation has a wavevector given by [16]

$$q_1(\omega) = \sqrt{2E_v} - \sqrt{2(E_v - \omega)} \tag{10.81}$$

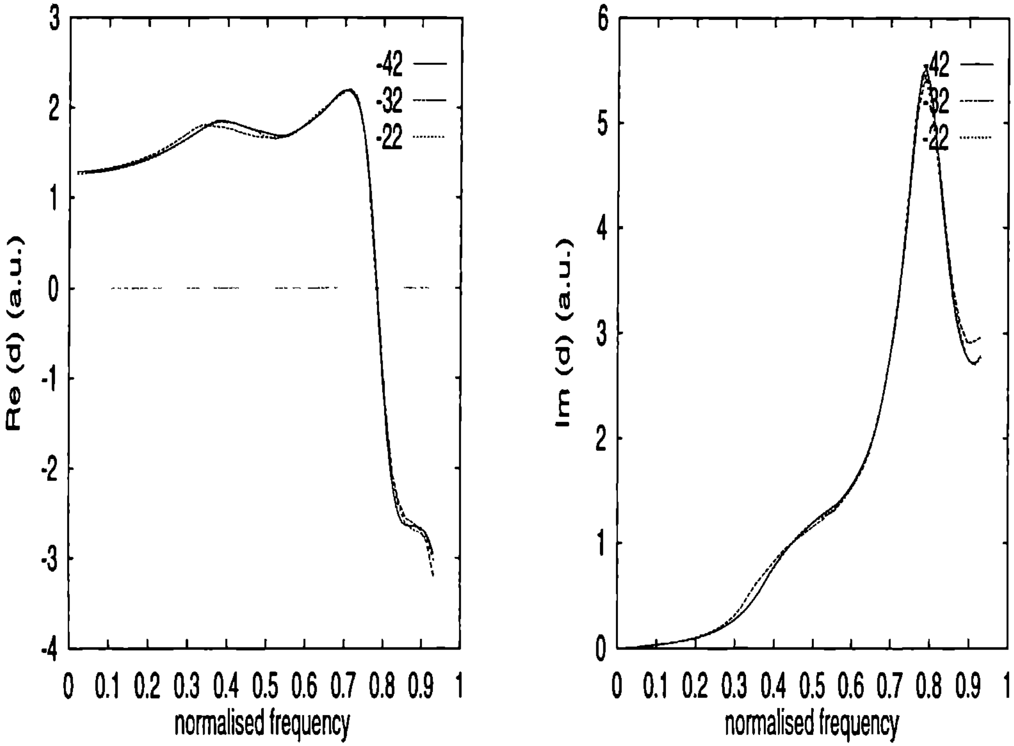

Figure 10.4: Real (left) and imaginary part (right) of centroid d as a function of normalised frequency ω/ω_p calculated with $Z_b = -22, -32$ and -42 a.u. The bulk density corresponds to $r_s = 3$.

which is a solution of [3]

$$\frac{1}{2}k^2 + \omega = \frac{1}{2}(k+q)^2 = E_v \tag{10.82}$$

subject to

$$0 < |k| < k_F \tag{10.83}$$

Physically, the above equation describes a process in which an electron with momentum k is excited to an unoccupied state with momentum $(k+q)$ and energy E_v.

At $\omega = 0.7\omega_p$ we are just below the surface plasma frequency ω_{sp} where the total induced surface charge diverges. This is reflected in the huge amplitude of both real and imaginary parts of the induced charge at $\omega = 0.7\omega_p$ (note the change in the scales in figures 10.5 and 10.6). At frequencies above ω_{sp} the integrated surface charge becomes negative so that V^{ind} and V^{ext} oscillate in phase and the total field is able to penetrate

---

[3] This equation has a second solution $q_2(\omega) = \sqrt{2E_v} + \sqrt{2(E_v - \omega)}$ which must be discarded since the corresponding value for k is negative.

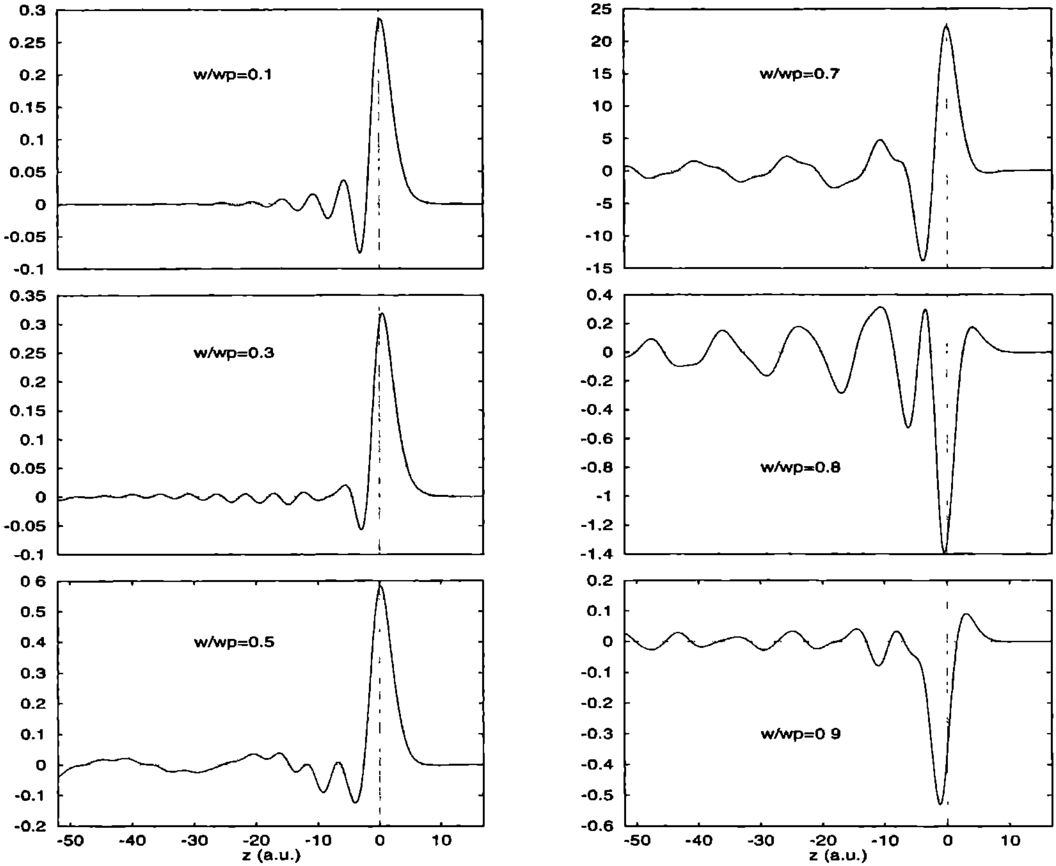

Figure 10.5: Real part of the induced density calculated at several frequencies below ω_p for $r_s = 3$. The plasma frequency is $\omega_p = 0.33$ a.u. The surface region is given by $-52 \leq z \leq 17$ a.u. Note the difference in vertical scales.

the interior much more efficiently. Consequently, the induced charge begins to spread into the metal. The oscillatory part of the induced charge density at $\omega = 0.8\omega_p$ is completely dominated by the wavelength $\lambda_1 = 2\pi/q_1 = 14$ a.u., indicating that excitations to the vacuum level are dominating at this frequency. At still higher frequencies the surface peak starts to collapse and at the bulk plasma frequency (not shown here), the induced charge becomes delocalised.

In figure 10.7 we show the real part of the total electric field for the same range of frequencies together with its asymptotic value $-2\pi(\sigma_s - 1)z$. The step-like profile of the field is due to the main peak in the screening charge around $z = 0$. At $\omega = 0.1\omega_p$ the sharp step resembles the discontinuous field profile obtained from the classical theory.

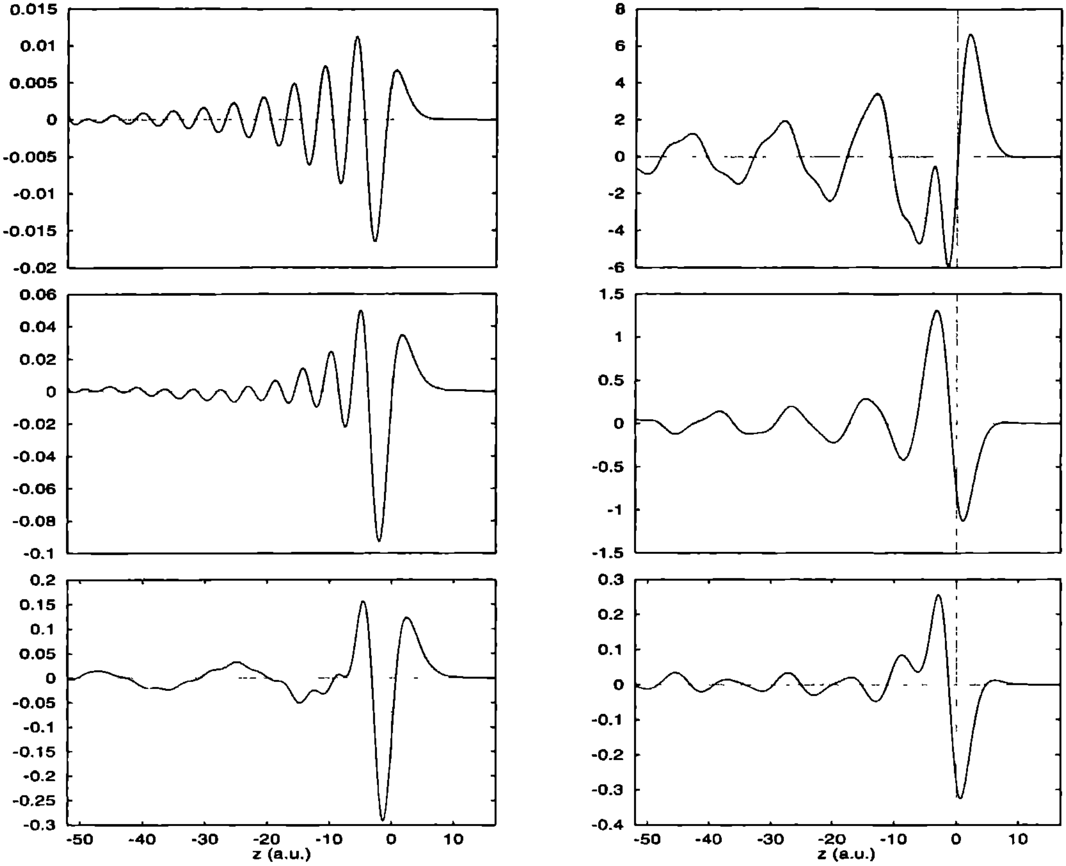

Figure 10.6: The same as figure 10.5 but for the imaginary part of the induced density.

At this frequency $E(z,\omega)$ shows weak Friedel oscillation inside the metal, approaching quickly its asymptotic value over a distance of ~ 20 a.u. The Friedel oscillations in the field are much more pronounced at higher frequencies and they penetrate deep inside the solid. The imaginary part of the field, which has no classical counterpart, consists of a sharp peak located at the surface and the usual Friedel oscillation.

The d-parameter

In figure 10.8 results for both the real and imaginary part of $d(\omega)$ are shown for bulk densities corresponding to $r_s = 2, 3$ and 4 a.u. For small ω the imaginary part of $d(\omega)$ varies linearly with frequency since the phase space for electron-hole excitations grows proportionally with ω. The real part of $d(\omega)$ at $\omega = 0$ coincides with the position of the

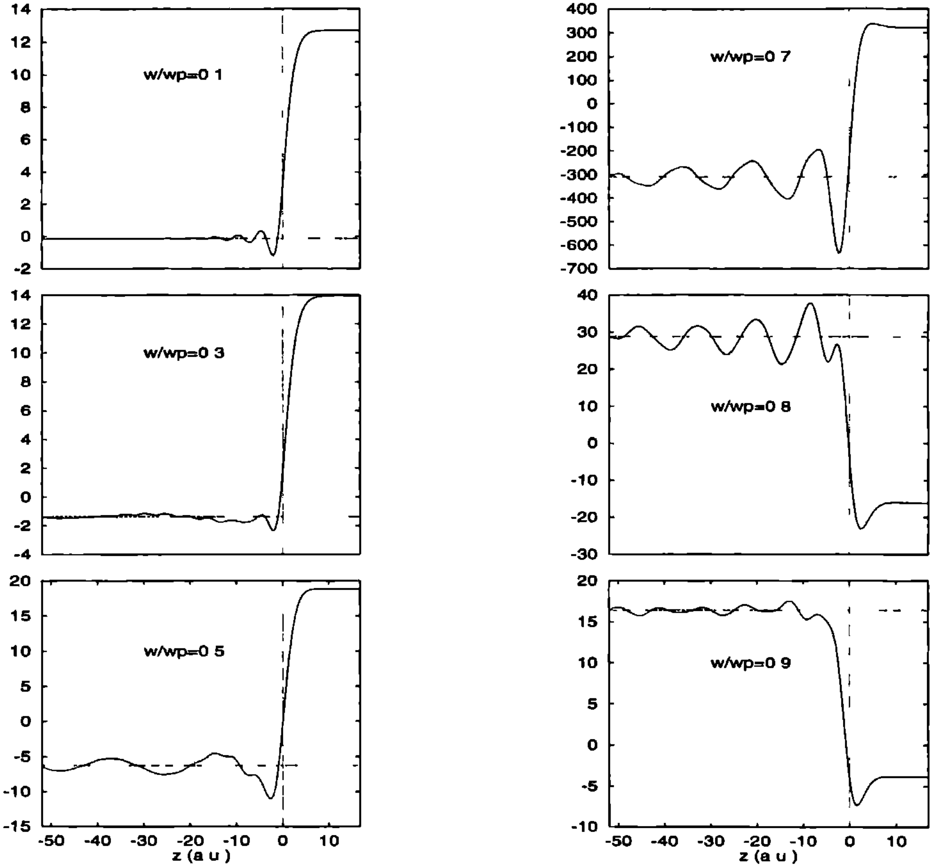

Figure 10.7: Real part of the total electric field (solid lines) calculated with the same parameters as in figure 10.5. The dashed lines are the asymptotic bulk fields given by $-2\pi(\sigma_s(\omega) - 1)$. Note the difference in vertical scales.

static image plane which for all r_s values lies outside the surface. *Red*(ω) shifts gradually outwards as the frequency increases.

At higher frequencies and for all r_s values two main spectral features are observable. The first feature is associated with the threshold for photoemission [5, 20]. For $r_s = 2$ it appears as a peak in the real part of $d(\omega)$ just below this threshold ($\Phi = 0\ 24\omega_p$) and a steep rise in the imaginary part of $d(\omega)$. Since the rise in *Imd* starts below the threshold it cannot be attributed solely to photoemitted electrons, but must also have a significant contribution from absorption into final states that propagate into the bulk of the metal. This structure is less pronounced for larger r_s for which the potential barrier is more diffuse and the work function is a larger fraction of ω_p. For $r_s = 3$, it shows up as a

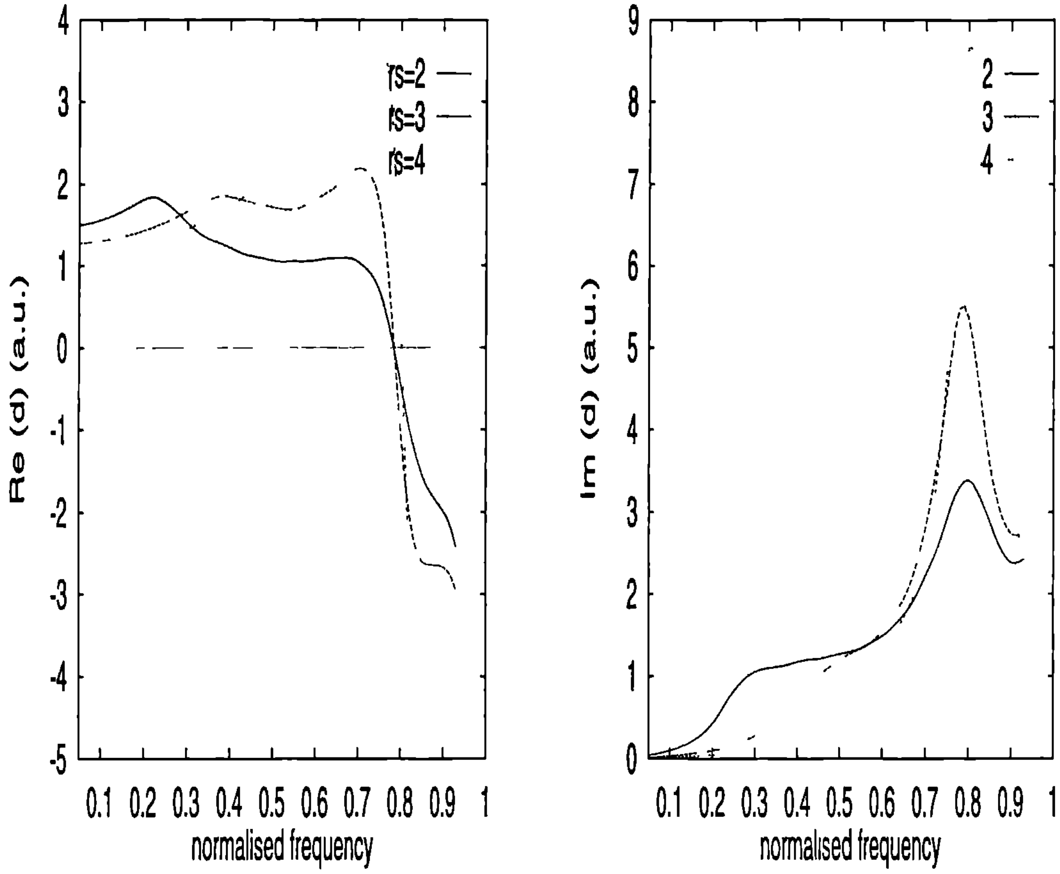

Figure 10.8 Real and imaginary parts of centroid d as a function of normalised frequency ω/ω_p for simple metal surfaces with bulk densities corresponding to $r_s = 2, 3$ and 4. The calculations are performed for a surface region given by $-42 \leq z \leq 17$ a.u.

weak shoulder in the imaginary part of $d(\omega)$ and a small bump in the real part. Note that there is no structure in $d(\omega)$ at the surface plasmon frequency $w_p/\sqrt{2}$ because of the normalisation factor $\sigma(\omega)$ in (10.26) which diverges at $\omega = \omega_{sp}$ resulting in a finite value of $d(\omega)$ at this frequency.

The next structure which we discuss becomes more significant for large r_s where the ground state density profile is more diffuse. It consists of a sharp resonance in $Imd(\omega)$ at $\omega \approx 0.8\omega_p$, and the associated rapid swing in $Red(\omega)$ from large positive values to large negative values in a small frequency range around this frequency. The resonance in $Imd(\omega)$ is relatively broad for $r_s = 2$ but becomes extremely sharp for $r_s = 4$. In $Red(\omega)$ a transfer of weight from the peak around $\omega = \Phi$ to the one around $0.8\omega_p$ can be seen as

r_s increases to higher values.

As we showed in section (10.2) the imaginary part of $d(\omega)$ is proportional to the rate of electron-hole excitations at the surface which determines the photocurrent in photoemission experiments [1]. Also, the energy loss probability of electrons in EELS is proportional to the imaginary part of the surface response function $g(\mathbf{q}_{||}, \omega)$ which at long-wavelength has the expansion [1]

$$g(\mathbf{q}_{||}) = \frac{\epsilon(\omega) - 1}{\epsilon(\omega) + 1}\left[1 + 2q\frac{\epsilon(\omega)}{\epsilon(\omega) + 1}d(\omega)\right] \tag{10.84}$$

Thus a resonance in $Imd(\omega)$ around $\omega = 0.8\omega_p$ should show up as a corresponding feature in both photoemission and EELS spectra. This is indeed the case as is shown by measurements for several simple metal surface such as K, Cs and Al [17, 18, 19].

The above resonance behaviour in $d(\omega)$, usually referred to as the surface multipole mode, has been discussed by several authors [1, 5, 20]. It is associated with a singularity in the response function $d(\omega)$ in the lower half of the complex frequency plane which results in a corresponding resonance along the real axis. We note that the name multipole mode is rather misleading since the induced charge density at the resonance frequency has a monopole character (figure 10.5). However the electron density fluctuations associated with the corresponding pole below the real axis have indeed a zero total weight hence the name multipole mode [18].

As ω increases beyond $0.8\omega_p$, $Re\delta n(z, \omega)$ moves inside the metal and the imaginary part decreases rapidly. At the bulk plasma frequency both the real and imaginary parts of $d(\omega)$ must diverge due to excitation of the bulk plasmon. In this frequency range, however, our results are not accurate enough to estimate the analytical form of this divergence. We note that analytical estimates of simple hydrodynamic model calculation gives a $(\omega - \omega_p)^{-1/2}$ behaviour [21].

10.6 Beyond the jellium approximation?

In this chapter a method has been presented for calculating the full non-local response of metal surfaces to time-dependent potentials within the jellium model and using the time-dependent local density approximation of electron-electron interactions. We applied this method to several metal surfaces and showed that below the bulk plasma frequency accurate results for the induced surface charge density and potential can be obtained using rather short surface regions extending ~ 20 Å into the metal. In particular the centroid of the induced surface charge $d(\omega)$ which characterises the macroscopic surface response can be accurately calculated.

The key feature of our approach is that we treat explicitly only a finite region around the surface where rapid variations in the induced potential occur. In the jellium case this is possible since below the bulk plasma frequency the non-local contributions from the semi-infinite bulk, crucial for a correct description of the surface response, can be calculated analytically knowing the approximate functional form of the asymptotic bulk potential and the exact form of the "off-diagonal" density response function. A natural question to ask is if this procedure can be extended to more realistic surfaces where band-structure effects become important. As far as calculating the "off-diagonal" density response is concerned the answer is "yes", since the matching Green function technique used for calculating this quantity can be readily applied to real surfaces. Finding a suitable approximation for the asymptotic form of the bulk potential, however, is more difficult as we illustrate below.

For this purpose we consider a model system in which electrons move freely in the direction parallel to the surface and experience the following bulk pseudo-potential in the z-direction

$$V(z) = 2V\cos(g_0 z) \tag{10.85}$$

This system has been studied in detail by Burke and Schaich [22] using parameters V and g_0 appropriate for simulating the band structure of Li in the (110) direction. They used a Fourier-space approach which was made tractable by the assumption of an infinite surface barrier. In switching from a jellium to the above system the asymptotic behaviour of the total field becomes [22, 23]

$$E(z) = E^{out}\left\{\epsilon_0^{-1}(0,0,\omega) + \sum_g \epsilon_0^{-1}(g,0,\omega)e^{igz}\right\} \qquad z \to -\infty. \tag{10.86}$$

Here g is a one-dimensional reciprocal lattice vector and $\epsilon_0(g,g',\omega)$ is the microscopic bulk dielectric matrix evaluated in the long-wavelength limit. The second term inside the bracket represents the so-called local field effects. These are undamped periodic oscillations created by the crystal umklapp process which have the same periodicity as the underlying lattice. More importantly, at frequencies where the dielectric matrix becomes singular, the above expression must be supplemented by a solution of the homogeneous equation (i.e. $E(z,\omega) \neq 0$, $E^{out} = 0$) at that frequency. These are self-sustaining oscillations of the bulk system and are obtained from the condition

$$det(\epsilon_q^{-1}(g,g',\omega)) = 0 \tag{10.87}$$

In the jellium case the dielectric matrix is diagonal and (10.87) simply gives the condition for excitation of bulk plasmons. In the case of a crystal, however, other solutions than the bulk plasmons may exist at frequencies well below the bulk plasma frequency. These are the so-called zone-boundary collective states which produce long-range oscillations inside the bulk with a frequency-dependent period larger than the lattice constant. The existence of such modes was suggested several years ago [24] in the context of bulk dielectric response and has been confirmed by more recent model calculations [25] and by EELS experiments [26].

Obviously, our jellium procedure for approximating the asymptotic bulk potential corresponds to neglecting both local field contributions and the possibility for excitation of such crystal-induced collective modes. Our preliminary calculations for the above system indicates that bulk local field effects do not affect the surface response significantly since these oscillations have a zero average over one unit cell. However, we encountered serious difficulties in obtaining convergent results at frequencies above the threshold for interband transitions, which for the above model system lies well below the bulk plasma frequency. We believe that these difficulties are mainly due to excitation of the zone-boundary collective states whose band starts just above this threshold.

References

[1] P.J. Feibelman, Prog. Surf. Sci. **12**, 287 (1982).

[2] P. Apell, Phys. Scr. **24**, 795 (1981).

[3] A. Liebsch, Phys. Scr. **35**, 354 (1987).

[4] P.J. Feibelman Phys. Rev. B **12**, 1319 (1975).

[5] A. Liebsch, Phys. Rev. B **36**, 7378 (1987).

[6] See for example, A.L. Fetter and J.D. Walecka, *Quantum Theory of Many-Body Systems* (McGraw-Hill, New York, 1971).

[7] A. Zangwell and P. Soven, Phys. Rev. A **21**, 1561 (1980); M.J. Stott and E. Zaremba, ibid. **21**, 12 (1980).

[8] B.N.J. Persson and P. Apell, Phys. Rev. B **27**, 6058 (1983).

[9] G.D. Mahan, *Many-Particle Physics* (Plenum Press, New York, 1990).

[10] P.J. Feibelman, Phys. Rev. B **22**, 3654 (1980).

[11] B.N.J. Persson and E. Zaremba, Phys. Rev. B **30**, 5669 (1984).

[12] R.S. Sorbello, Solid State Commun. **56**, 821 (1985).

[13] U. von Barth and L. Hedin, J. Phys. C **5**, 1629 (1972).

[14] J.E. Inglesfield and G.A. Benesh, Phys. Rev. B **37**, 6682 (1988).

[15] J.E. Inglesfield, J. Phys. C **4**, L14 (1971).

[16] K. Kempa, A. Liebsch and W.L. Schaich, Phys. Rev. B **38**, 12645 (1988).

[17] K.D. Tsuei, E.W. Plummer, A. Liebsch, K. Kempa and P. Bakshi, Phys. Rev. lett. **64**, 44 (1990).

[18] K.D. Tsuei, E.W. Plummer, A. Liebsh, E. Pehlke, K. Kempa and P. Bakshi, Surf. Sci. **247**, 302 (1991).

[19] E. Levinson, E.W. Plummer and P.J. Feibelman, Phys. Rev. lett. **43**, 952 (1979).

[20] K. Kempa and W.L. Schaich, Phys. Rev. B **37**, 6711 (1988).

[21] W.L. Schaich and K. Kempa, Phys. Scr. **35**, 204 (1987).

[22] K. Burke and W.L. Schaich, Phys. Rev. B **48**, 14599 (1993).

[23] W.L. Schaich, Phys. Rev. B **50**, 17587 (1994).

[24] E-Ni Foo and J.J. Hopfield, Phys. Rev. **173**, 635 (1968).

[25] K. Sturm and L.E. Oliveira, Phys. Rev. B **40**, 3672 (1988).

[26] J. Fink, Adv. Electron. Electron Phys. **75**, 121 (1989).

Samenvatting

Dit proefschrift gaat over elektronenstruktuur berekeningen voor metaaloppervlakken. Het doel van deze berekeningen is het bepalen van elektronische eigenschappen van metaaloppervlakken (uittree-arbeid, elektronendichtheid en elektronische toestanden, lokale magnetisatie enz.) door het oplossen van de Schrödinger vergelijking voor elektronen in deze systemen. Door de onderlinge wisselwerking van elektronen te *benaderen* door een gemiddelde potentiaal kan de veeldeeltjes Schrödinger vergelijking gereduceerd worden tot een vergelijking voor een *enkel* elektron. Deze Schrödinger vergelijking kan vervolgens numeriek worden opgelost. In dit werk wordt een aanpak gebruikt die gebaseerd is op de zogenaamde dichtheidsfunctionaal theorie in de lokale dichtheid benadering (hoofdstuk 1). Deze aanpak leidt tot een gemiddelde potentiaal die afhangt van de dichtheid van elektronen. De elektronendichtheid is *a priori* niet bekend en de resulterende vergelijking wordt iteratief (zelfconsistent) opgelost.

In deel I van dit proefschrift worden nieuwe methoden beschreven voor het numeriek oplossen van de Schrödinger vergelijking aan oppervlakken. In deel II worden deze methoden gebruikt om de eigenschappen van een belangrijke klasse van oppervlaktetoestanden van metaaloppervlakken te onderzoeken. Deel III beschrijft modelberekeningen voor de diëlektrische respons van metaaloppervlakken op tijdsafhankelijke elektrische velden.

Het oplossen van de Schrödinger vergelijking voor elektronen in een perfekt en oneindig kristal wordt aanzienlijk vereenvoudigd door de aanwezigheid van translatiesymmetrie van het rooster in drie richtingen. Aan het oppervlak is translatiesymmetrie afwezig in de richting loodrecht op het oppervlak zodat geen eenvoudige reductie met betrekking tot deze coördinaat kan worden verkregen (de Schrödinger vergelijking strekt zich uit over een *oneindig* gebied in de richting loodrecht op het oppervlak). In de "embedding" methode (hoofdstuk 2) wordt dit probleem aangepakt door gebruik te maken van het feit dat afwijkingen in het potentiaal – ten opzichte van de bulk of vacuüm – beperkt zijn tot een *eindig* gebied rond het oppervlak. De Schrödinger vergelijking wordt dan uitsluitend in dit gebied zelfconsistent opgelost en waarbij het effect van het resterende substraat *impliciet* wordt meegenomen. Dit gebeurt door het toevoegen van een energieafhankelijke en niet-lokale potentiaal – de "embedding" potentiaal – aan de Hamiltoniaan in dit gebied. De "embedding" potentiaal is direkt gerelateerd aan de Greense functie van het substraat. Door de aanwezigheid van deze potentiaal sluiten de elektrongolffuncties in het oppervlaktegebied correct (d.w.z. in amplitude *en* afgeleide) aan op de golffuncties van het substraat. De "embedding" methode geeft dus een correcte beschrijving van de elektronische toestanden aan het oppervlak en het continuüm van bulktoestanden. Dit is een belangrijk voordeel van de methode. Hierdoor is het mogelijk om de resultaten van de berekeningen direct te gebruiken voor het interpreteren van spectroscopische metingen aan oppervlakken.

Het bepalen van de "embedding" potentiaal van het substraat speelt een cruciale rol in deze methode. Voorheen werd deze berekend door in het substraat gebruik te maken van de "muffin-tin" benadering (in de "muffin-tin" benadering wordt de ruimte opgedeeld in niet-overlappende bollen rond de atoomkernen. Binnen de bollen wordt de potentiaal benaderd door een sferische middeling uit te voeren. In de tussenliggende ruimte wordt de potentiaal benaderd door een constante waarde). Het gebruik van deze benadering heeft het nadeel dat het oppervlak (waar geen benadering gemaakt wordt voor de potentiaal) en het onderliggende substraat niet geheel compatibel zijn. Dit kan leiden tot convergentieproblemen in de zelfconsistentie procedure. In hoofdstuk 3 wordt dit probleem aangepakt door een nieuwe iteratieve methode te ontwikkelen voor het bepalen van de "embedding" potentiaal van het substraat waarbij *geen* benadering wordt gemaakt voor de potentiaal in het substraat. In veel toepassingen is het noodzakelijk om de Schrödinger vergelijking op te lossen voor een oppervlaktegebied dat een groot aantal atoomlagen bevat omdat de storing diep in het metaal doordringt. Een voorbeeld hiervan zijn de gestapte oppervlakken. In hoofdstuk 3 wordt vervolgens een methode gepresenteerd om de numerieke oplossing van de Schrödinger vergelijkingen in deze gevallen te versnellen. Deze methode wordt verder uitgewerkt in hoofdstuk 4 en toegepast op het gestapte jelliumoppervlak (jellium is een vereenvoudigd model voor een metaal waarbij de ionen zijn vervangen door een homogene achtergrond van positieve lading). In hoofdstuk 5 laten we zien hoe de "embedding" methode kan worden toegepast om de eigentoestanden te bepalen van begrensde quantumsystemen, zoals een onzuiverheid in een "quantum dot" of een "quantum wire".

In deel II worden de methoden van deel I gebruikt voor het bestuderen van beeldpotentiaaltoestanden op metaaloppervlakken. Buiten het metaaloppervlak ondervinden elektronen een attractieve potentiaal. Asymptotisch heeft deze potentiaal de vorm van de klassieke beeldpotentiaal hetgeen aanleiding geeft tot een *oneindige* reeks van toestanden gelocaliseerd aan het oppervlak: dit zijn de beeldpotentiaal-toestanden (hoofdstuk 6). Deze toestanden komen bij een groot aantal metaaloppervlakken voor. Het bestuderen van hun eigenschappen verschaft informatie over elektron-elektron wisselwerking, variaties in de uittree-arbeid en lokale magnetisatie nabij het oppervlak. Deze eigenschappen (energie, dispersierelatie, magnetische opsplitsing) kunnen worden waargenomen met behulp van inverse foto-emissie, twee-foton foto-emissie en "scanning tunneling microscopy" (STM).

De grootheid die in inverse foto-emissie wordt waargenomen is de lokale toestandsdichtheid van de elektronen (de dichtheid van elektronen met een gegeven energie). In hoofdstuk 7 wordt het effect van de beeldpotentiaal op deze grootheid onderzocht. In de literatuur is gesuggereerd dat de lokale toestandsdichtheid een singulier gedrag vertoont bij de vacuüm energie. Onze berekening voor twee verschillende oppervlakken Ni(001) en Al(001) laten zien dat dit niet het geval is. In tegendeel, door de aanwezigheid van de beeldpotentiaal vertoont de lokale toestandsdichtheid een glad verloop bij deze energie. Deze conclusie is van belang bij de interpretatie van inverse photo-emissie spectra: het betekent dat de vacuüm energie – dus de uittree-arbeid – *in principe* niet kan worden gedetecteerd met deze techniek. We tonen vervolgens aan dat het continue gedrag van de toestandsdichtheid een gevolg is van opeenhoping van een *oneindig* aantal beeldpotentiaal-toestanden net onder de vacuüm energie.

Beeldpotentiaal-toestanden op ferromagnetische oppervlakken kunnen opgesplitst worden in spin-op en spin-neer toestanden. Dit is het gevolg van hun wisselwerking met enerzijds het ferromagnetische substraat en anderzijds de spin-gepolariseerde oppervlakte-barrière. In hoofdstuk 8 berekenen we de spin-opsplitsing van beeldpotentiaal-toestanden op het Fe(110) oppervlak en onderzoeken we de oorsprong van deze opsplitsing. We vinden een opsplitsing van 55 meV voor de $n = 1$ toestand. Zeer recentelijk is deze voorspelling bevestigd door inverse photo-emissie experimenten (57 ± 5 meV). We laten zien dat de opsplitsing voornamelijk veroorzaakt wordt door de interactie van beeldpotentiaal-toestanden met het substraat. De bijdrage van de spin-gepolariseerde barrière aan de opsplitsing is veel kleiner ($\approx 10\%$) en is *tegengesteld* aan de bijdrage van het substraat. Dit laatste resultaat kan worden verklaard uit het feit dat de lokale magnetisatie net buiten het Fe(110) oppervlak negatief wordt (meer spin-neer dan spin-op elektronen) – een effect die zou kunnen worden waargenomen in spin-gepolariseerde STM experimenten. Hoofdstuk 9 bevat de resultaten van onze berekeningen voor de (spin-afhankelijke) dispersierelatie van beeldpotentiaal-toestanden op Fe(110). Voor beide spinrichtingen blijken deze nagenoeg te voldoen aan de dispersierelatie van vrije elektronen – grote afwijkingen van dit gedrag komen alleen voor in de buurt van de spin-gepolariseerde bulk continua waar de dispersierelatie sterk spin-afhankelijk wordt.

Het laatste deel van dit proefschrift gaat over het bepalen van de tijdsafhankelijke diëlektrische respons van metaaloppervlakken. Dit is van belang voor het interpreteren van optische en spectroscopische experimenten aan het oppervlak en komt neer op het oplossen van een stelsel integraalvergelijkingen die de respons beschrijven. De fysisch meest interessante situatie treedt op wanneer het elektrisch veld loodrecht staat op het oppervlak. Verder is de golflengte van de storing (bijvoorbeeld het veld van een optische laser) meestal veel langer dan de Fermi golflengte. Het probleem dat zich in dit geval voordoet is dat de integraalvergelijkingen zich uitstrekken over een *oneindig* gebied (in de richting normaal op het oppervlak). In hoofdstuk 10 wordt een methode beschreven voor het oplossen van deze vergelijkingen voor het jelliumoppervlak.

List of publications

1. B.J. Geurts, M. Nekovee, H.M.J. Boots and M F.H. Schuurmans: *Exact and moment equation modeling of electron transport in submicron structures*, Appl. Phys. Lett. **59**, 1743 (1991).
2. M. Nekovee, B.J. Geurts, H.M.J. Boots and M.F.H. Schuurmans: *Failure of extended-moment-equations approaches to describe ballistic transport in submicrometer structures*, Phys. Rev. B **45**, 6643 (1992).
3. S. Crampin, J.B.A.N. van Hoof, M. Nekovee and J.E. Inglesfield: *Full-potential embedding for surfaces and interfaces*, J. Phys. C **4**, 1475 (1992).
4. M. Nekovee and J.E. Inglesfield: *Threshold behaviour of surface density of states at the vacuum level*: Europhys. Lett. **19**, 535 (1992).
5. S. Crampin, M. Nekovee, J.A.B.N. van Hoof and J.E. Inglesfield: *Subvolume embedding for interfacial electronic structure*, Surf. Sci. **287**, 732 (1993).
6. M. Nekovee, S. Crampin and J.E. Inglesfield: *Magnetic splitting of image states at Fe(110)*, Phys. Rev. Lett. **70**, 3099 (1993).
7. M. Nekovee and J.E. Inglesfield: *Image-induced surface states and resonances at Fe(110)*, Surface Review and Letters **1**, 415 (1994).
8. S. Crampin M. Nekovee and J.E. Inglesfield: *The embedding method for confined quantum systems*, Phys. Rev. B **51**, 7318 (1995).
9. M. Nekovee and J.E. Inglesfield: *Theory of Image States at Magnetic Surfaces*, Prog. Surf. Sci., to be published.

Curriculum Vitae

Maziar Nekovee
Geboren op 14 juli 1965 te Teheran, Iran

juni 1983	Eindexamen middelbare school te Teheran.
juni 1984	Vertrek uit Iran.
september 1984	Aankomst in Nederland.
1985-1990	Studie Elektrotechniek aan de Technische Universiteit Delft. Afstudeerproject bij het Philips Natuurkundig Laboratorium. Onderwerp: Modelleren van ballistische elektronen transport in submicron halfgeleider componenten.
juni 1990	Doctoraal examen (*cum laude*).
1990-1994	Assistent in Opleiding aan de Katholieke Universiteit Nijmegen bij de groep Elektronenstruktuur van Materialen. Promotie-onderzoek verricht onder begeleiding van Prof. J.E. Inglesfield. Onderwerp: Beeldpotentiaal-toestanden en diëlektrische respons van metaaloppervlakken. Promotie datum 12 september 1995.
maart 1995-	Post-doc bij de afdeling Condensed Matter Theory, Imperial College of Science Technology and Medicine, London.